DESIGN, CONSTRUCTION AND CONTROL OF AN ELECTRO-HYDRAULIC LOAD SIMULATOR FOR TESTING HYDRAULIC DRIVES

A THESIS SUBMITTED TO
THE GRADUATE SCHOOL OF NATURAL AND APPLIED SCIENCES
OF
MIDDLE EAST TECHNICAL UNIVERSITY

BY

HAYRETTİN ULAŞ AKOVA

IN PARTIAL FULFILLMENT OF THE REQUIREMENTS
FOR
THE DEGREE OF MASTER OF SCIENCE
IN
MECHANICAL ENGINEERING

SEPTEMBER 2014

Approval of the thesis:

DESIGN, CONSTRUCTION AND CONTROL OF AN ELECTRO-HYDRAULIC LOAD SIMULATOR FOR TESTING HYDRAULIC DRIVES

submitted by **HAYRETTİN ULAŞ AKOVA** in partial fulfillment of the requirements for the degree of **Master of Science in Mechanical Engineering Department, Middle East Technical University** by,

Prof. Dr. Canan Özgen _____
Dean, Graduate School of **Natural and Applied Sciences**

Prof. Dr. Suha Oral _____
Head of Department, **Mechanical Engineering**

Prof. Dr. Bülent E. Platin _____
Supervisor, **Mechanical Engineering Dept., METU**

Prof. Dr. Tuna Balkan _____
Co-Supervisor, **Mechanical Engineering Dept., METU**

Examining Committee Members:

Prof. Dr. Y. Samim Ünlüsoy _____
Mechanical Engineering Dept., METU

Prof. Dr. Bülent E. Platin _____
Mechanical Engineering Dept., METU

Prof. Dr. Tuna Balkan _____
Mechanical Engineering Dept., METU

Asst. Prof. Dr. Yiğit Yazıcıoğlu _____
Mechanical Engineering Dept., METU

Prof. Dr. Yücel Ercan _____
Mechanical Engineering Dept., TOBB ETU

Date: 04.09.2014

I hereby declare that all information in this document has been obtained and presented in accordance with academic rules and ethical conduct. I also declare that, as required by these rules and conduct, I have fully cited and referenced all material and results that are not original to this work.

Name, Last name : Hayrettin Ulaş AKOVA

Signature :

ABSTRACT

DESIGN, CONSTRUCTION AND CONTROL OF AN ELECTRO-HYDRAULIC LOAD SIMULATOR FOR TESTING HYDRAULIC DRIVES

Akova, Hayrettin Ulaş
M.S., Department of Mechanical Engineering
Supervisor : Prof. Dr. Bülent E. Platin
Co-Supervisor: Prof. Dr. Tuna Balkan

September 2014, 171 pages

In this thesis, an electro-hydraulic load simulator is designed, constructed, and controlled in order to carry out the stability and performance tests of newly developed hydraulic drive and control systems. It is an experimental loading system capable of applying the desired test loads onto the actuator of the hydraulic drive system under test in a laboratory environment. The primary aim of this study is to support the research activities related to the development of hydraulic drive and control systems so as to reduce their development period and to save the funds.

A fluid power control system with a valve controlled linear actuator is designed as the load simulator. The selection of the hydraulic components of the system is presented in detail. A real-time control system is employed for controlling the electro-hydraulic load simulator. A test bench is designed and constructed in order to accommodate the actuators of the electro-hydraulic load simulator and the hydraulic drive system under test.

A mathematical model of the system is developed and a simulation model is constructed by using MATLAB®/Simulink®. The model is validated by the results of open-loop tests. A combined feedforward and feedback force controller and a disturbance feedforward controller are designed by linearizing the validated model of the system around a critical operating point. The actuator position of the hydraulic drive system under test is measured with an incremental encoder and its velocity is estimated by a kinematic Kalman filter to be used in the disturbance feedforward controller. The controllers and the kinematic Kalman filter are implemented into a real-time control computer.

The dynamic performance of the electro-hydraulic simulator developed is evaluated by performing a series of real time experiments and comparing their results with the model responses. In addition, the loading limits of the simulator are clearly demonstrated by both experimental tests and simulation results.

Keywords: Electro-Hydraulic Load Simulator, Fluid Power Control System, Modeling and Validation, Force Control, Combined Feedforward and Feedback Control, Kinematic Kalman Filtering

ÖZ

HİDROLİK SÜRÜCÜ SİSTEMLERİNİN TESTLERİ İÇİN ELEKRO-HİDROLİK YÜK SİMÜLATÖRÜ TASARIMI, ÜRETİMİ VE KONTROLÜ

Akova, Hayrettin Ulaş
Yüksek Lisans, Makina Mühendisliği Bölümü
Tez Yöneticisi : Prof. Dr. Bülent E. Platin
Ortak Tez Yöneticisi: Prof. Dr. Tuna Balkan

Eylül 2014, 171 sayfa

Bu tez çalışmasında, yeni geliştirilmekte olan hidrolik sürücü ve kontrol sistemlerinin kararlılık ve başarım testlerinin gerçekleştirilmesi için bir elektro-hidrolik yük simülatörü tasarlanmış, üretilmiş ve kontrolü gerçekleştirilmiştir. Bu yük simülatörünün, geliştirilmekte olan hidrolik sürücü sistemlerinin test edilmesi amacıyla belirlenen kuvvetleri laboratuvar ortamında uygulayabilen deneysel bir yükleme sistemi olarak kullanılması hedeflenmiştir.

Yük simülatörü olarak valf kontrollü doğrusal bir eyleyiciye sahip bir akışkan gücü kontrol sistemi tasarlanmıştır. Sistemi oluşturan hidrolik ekipmanların seçimi ayrıntılı olarak verilmiştir. Elektro-hidrolik yük simülatörünün kontrolünü gerçekleştirmek için gerçek zamanlı bir kontrol sistemi kurulmuştur. Yük simülatörünün ve test edilmekte olan hidrolik sürücü sisteminin eyleyicilerinin uygun bir şekilde birbirlerine bağlanabilmesi için bir test düzeneği tasarlanıp üretilmiştir.

Sistemin matematiksel modeli kurularak MATLAB®/Simulink® ortamında bir benzetim modeli oluşturulmuştur. Bu model açık çevrim test sonuçları ile doğrulanmıştır. Model kritik bir çalışma noktası etrafında doğrusallaştırılarak bir birleşik ileri ve geri besleme kuvvet kontrolcüsü ve test edilecek sistemin hareketinden kaynaklı bozucu etkiyi giderici bir ileri besleme hız kontrolcüsü tasarlanmıştır. Test edilmekte olan sistemin eyleyici konumu doğrusal bir cetvel ile ölçülmekte, hızı ise kinematik Kalman filtresi kullanılarak kestirilmektedir. Kontrolcüler ve kinematik Kalman filtresi bir gerçek-zamanlı kontrol bilgisayarında gerçekleştirilmiştir.

Elektro-hidrolik yük simülatörünün dinamik başarımı yapılan testler ile değerlendirilmiş ve model yanıtları ile karşılaştırılmıştır. Ayrıca simülatörün yükleme kapasitesi deneysel sonuçlar ve yapılan simülasyonlar ile açık bir şekilde gösterilmiştir.

Anahtar Kelimeler: Elektro-Hidrolik Yük Simülatörü, Akışkan Gücü Kontrol Sistemi, Modelleme ve Doğrulama, Kuvvet Kontrolü, Birleşik İleri ve Geri Beslemeli Kontrol, Kinematik Kalman Filtre

To My Mother and Father

And

To My Love Özge

ACKNOWLEDGEMENTS

First of all, I would like to thank my supervisors Prof. Dr. Bülent E. Platin and Prof. Dr. Tuna Balkan for their guidance, advice, criticism and encouragement throughout this thesis study.

I sincerely like to thank to my colleague and officemate Hakan Çalışkan for his invaluable supports, comments and suggestions about my study. I would also like to express my appreciation to my colleagues Ulaş Yaman and Rasim Aşkın Dilan for their friendship and supports during my assistantship.

I am also grateful to Suat Demirer for his financial and technical supports for this study. I would like to thank to Göker Gökalp for his comments and technical supports in the construction of the test bench.

In addition, the financial support of the Scientific and Technological Research Council of Turkey (TÜBİTAK) is gratefully acknowledged.

Finally, I would like to thank to my family for their endless support and encouragement during my life.

TABLE OF CONTENTS

LIST OF TABLES

TABLES

LIST OF FIGURES

FIGURES

LIST OF SYMBOLS AND ABBREVIATIONS

SYMBOLS

$\mathbf{A}$	State matrix of the kinematic model of the disturbance actuator
A_A	Actuator piston side cross-sectional area
A_B	Actuator rod side cross-sectional area
A_p	Piston side pressure area
C	Chamber capacitance of the hydraulic actuator
C_d	Discharge coefficient
F	Force exerted on the system under test
F_f	Friction force
F_L	Load force applied by the hydraulic actuator
F_{ref}	Reference force input
$F_d(s)$	Disturbance feedforward controller
$F_u(s)$	Reference, or set-point, feedforward controller
$G_a(s)$	Transfer function of the valve actuator
$G_c(s)$	Feedback controller
$G_{FU}^{ext}(s)$	Transfer function between the controlled output and the manipulated input for extension case
$G_{FU}^{ret}(s)$	Transfer function between the controlled output and the manipulated input for retraction case
$G_{FX_d}^{ext}(s)$	Transfer function between the controlled output and the disturbance input for extension case

$G_{FX_d}^{ret}(s)$	Transfer function between the controlled output and the disturbance input for retraction case
$\mathbf{H}$	Output matrix for the kinematic model of the disturbance actuator
K_a	Steady state gain of the valve actuator
K_c	Flow-pressure coefficient of the valve
K_{c_A}	Flow-pressure coefficient corresponding to A port of the valve
K_{c_B}	Flow-pressure coefficient corresponding to B port of the valve
K_p	Proportional controller gain
K_{q_A}	Flow gain corresponding to A port of the valve
K_{q_B}	Flow gain corresponding to B port of the valve
K_q	Flow gain of the valve
K_v	Steady state flow gain of the valve
$\mathbf{K_k}$	Kalman gain
P_0	Operating point around which linearization is performed
$\mathbf{P_k}$	Posteriori error covariance estimate matrix
$\mathbf{P_k^-}$	Priori error covariance estimate matrix
Q	Flow rate
Q_A	Flow rate through A port of the valve
Q_B	Flow rate through B port of the valve
Q_{A0}	Steady state flow rate through A port of the valve
Q_{B0}	Steady state flow rate through B port of the valve
$\mathbf{Q}$	Process noise covariance matrix
$\mathbf{R}$	Measurement noise covariance matrix
R	Measurement noise covariance for the incremental encoder
T_a	Time constant of the valve actuator

T_s	Sampling time
V_A	Piston side volume of the hydraulic actuator
V_B	Rod side volume of the hydraulic actuator
V_{A_0}	Initial piston side volume of the hydraulic actuator
V_{B_0}	Initial rod side volume of the hydraulic actuator
X_0	Amplitude of the oscillations of the load actuator
$Z(s)$	Output impedance
b_p	Viscous friction coefficient
g	Hydraulic conductance of flow control valve per metering edge
k_s	Spring stiffness
m_p	Mass of the actuator piston
p_A	Piston side pressure of the hydraulic actuator
p_B	Rod side pressure of the hydraulic actuator
p_{A0}	Steady state piston side pressure of the hydraulic actuator
p_{B0}	Steady state rod side pressure of the hydraulic actuator
p_s	Supply pressure
p_t	Return (tank) pressure
p_L	Load pressure of the hydraulic actuator
$\tilde{q}$	Power spectral density of the continuous time process noise of the kinematic model of the disturbance actuator
u	Control input to the valve
$\mathbf{x}$	State vector of the disturbance actuator
x_p	Position of the hydraulic actuator
x_p^{max}	Maximum piston stroke
x_d	Position of the disturbance actuator

x_v	Valve spool position
v_d	Velocity of the disturbance actuator
v_p	Velocity of the hydraulic actuator
w	Peripheral width of the orifice
$\widetilde{w}(t)$	Zero mean white noise
$\mathbf{w_k}$	Process noise vector
$\mathbf{\Phi}$	State transition matrix for the kinematic model of the disturbance actuator
α	Pressure area ratio of the hydraulic cylinder
β	Bulk modulus of the hydraulic fluid
ω	Frequency of applied force
Δp	Pressure differential
ρ	Density of the hydraulic fluid

ABBREVIATIONS

MBD	Model Based Design
EMA	Electro-Mechanical Actuator
GUI	Graphical user interface
HIL	Hardware-in-the-Loop
MEA	More Electric Aircraft
DAQ	Data Acquisition
PI	Proportional-Integral
PD	Proportional-Derivative

PID	Proportional-Integral-Derivative
KKF	Kinematic Kalman Filter

CHAPTER 1

INTRODUCTION

1.1 Background and Motivations

Since the very early ages of the human history, many mechanisms and machines have been invented in order to ease the human life. Primitive and simply jointed mechanisms were the first machines and they were actuated by the human power [1]. However, the use of external power sources to actuate the components of machines was one the greatest desires of the human being. In around B.C. 250, the Alexandrian mechanician Ktesibios invented a float regulator valve to provide a water clock with a constant flow rate [2]. The increasing water level in a measuring vessel of the water clock was utilized as the indicator of the time. This invention of Ktesibios is commonly regarded as the earliest known servomechanism [3]. Since his invention, especially during the industrial revolution and the modern era, the hydraulic, pneumatic, and electric actuator technologies have evolved considerably and they become inevitable components of the modern machines. In addition, the development and practice of the control theory as well as the fields of electrics and electronics made fast and accurate motion control systems possible. Today, servo control systems are used in many industrial, military, and aerospace applications as the complex integration of mechanical structures, or mechanisms, with actuators, transducers, and control hardware and algorithms.

The design of control systems requires a multi-domain knowledge and the investigation of the whole system consisting of a number of subsystems from different physical domains [4]. Brezina et al. [5] underlined the importance of the

model based design (MBD) in designing mechatronic systems in many industrial, aerospace, and automotive applications. The modeling and the model analysis of the complete system under development constitute the basis of the design approach (Figure 1-1a). Generally, a parametric system model is regarded as a useful model since it allows the improvement of the model in each design cycle (Figure 1-1b). However, it was also stated that the accuracy obtained depends on the accordance between the real system and the developed models. Hence, the verification of the desired characteristics (*properties ensurance*) is highly essential as it can also be inferred from Figure 1-1a.

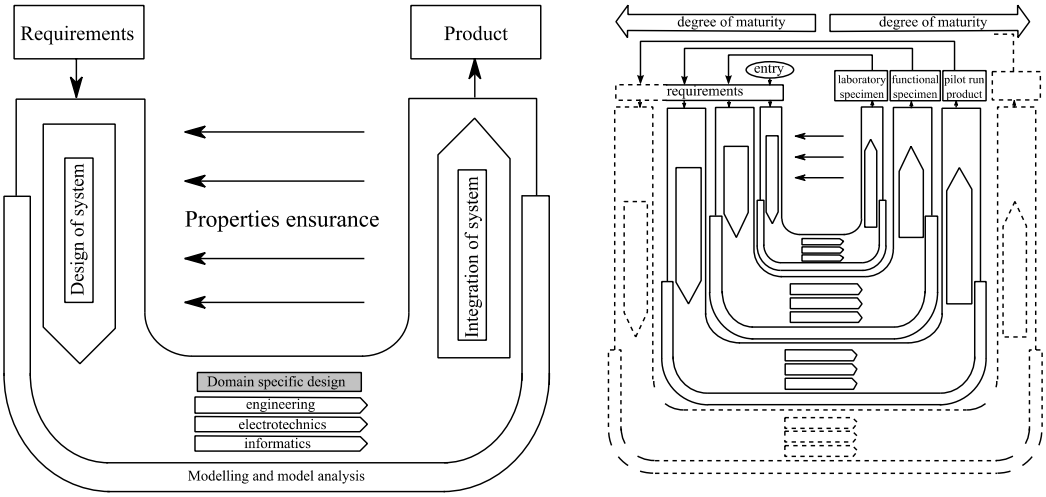

Figure 1-1 a) A mechatronic design cycle, b) recurrent design cycles [5]

While modeling dynamic systems, generally a number of simplifying assumptions are made. Sometimes, some fast dynamics of systems are intentionally neglected, or some important dynamics of systems may be missed unintentionally. In addition, some model parameters are only estimated as their nominal values. Often, some model parameters are assumed to be constant, even though they are actually time varying. Therefore, although modeling and simulation are highly important design tools, it should also be noted that testing models with real data compensates for the mentioned drawbacks and is also an important part of the whole product development process for verification and validation purposes.

The testing of drive systems on the actual plant, which can be a machine, or a vehicle, is usually not possible on the early phases of the design. Even if it is possible, it might cause safety problems before evaluating their performance in controlled laboratory conditions. Furthermore, the testing with the actual plant can be very expensive and time consuming. Thus, the initial testing of actuators and their controllers are generally performed in laboratory conditions by using either motion [6] or load simulators [7] depending on the application. Load simulators are used to re-create the test loads onto the actuator of the control system whereas motion simulators provide the disturbance motion.

In system dynamics terminology, a mechanical translational/rotational element which can provide any desired force/torque independent of the velocity of its point of application is called as an active T-type translational/rotational element [8]. In ideal cases, the same function is expected from a closed-loop force-controlled load simulator, which is an experimental loading unit. That is, a load simulator should be able to re-create and apply the operational loads onto the engineering system under test in laboratory conditions. The system under test can either be an actuator (Figure 1-2a) or a structure (Figure 1-2b). In addition, different drive technologies can be used as the load simulator; such as an electro-mechanical actuator (EMA) (Figure 1-2a) and an electro-hydraulic actuator (Figure 1-2b).

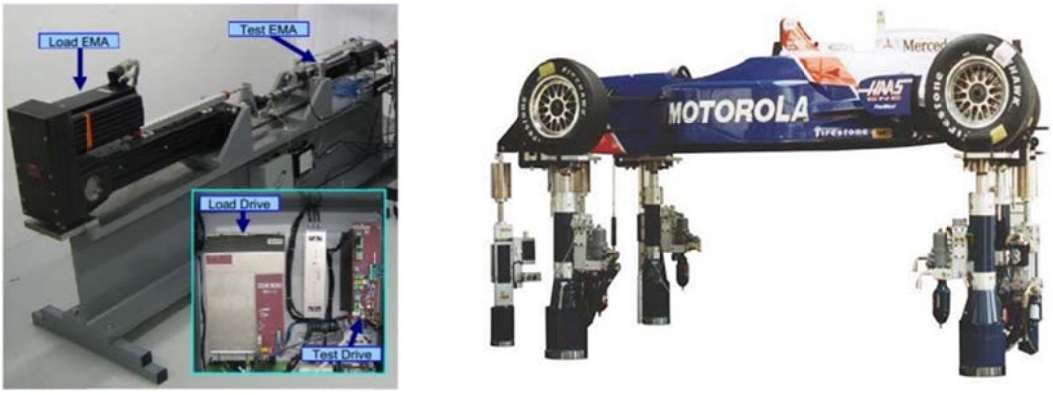

Figure 1-2 a) An EMA test bench at NASA AMES Research Center [9]
b) Dynamic structural testing of a Formula 1 car [10]

A schematic view of an electro-hydraulic load simulator test bench, which is used to simulate the loads affecting the rudder of an aircraft [11], is given in Figure 1-3 so as to explain the main components of a load simulator test bench.

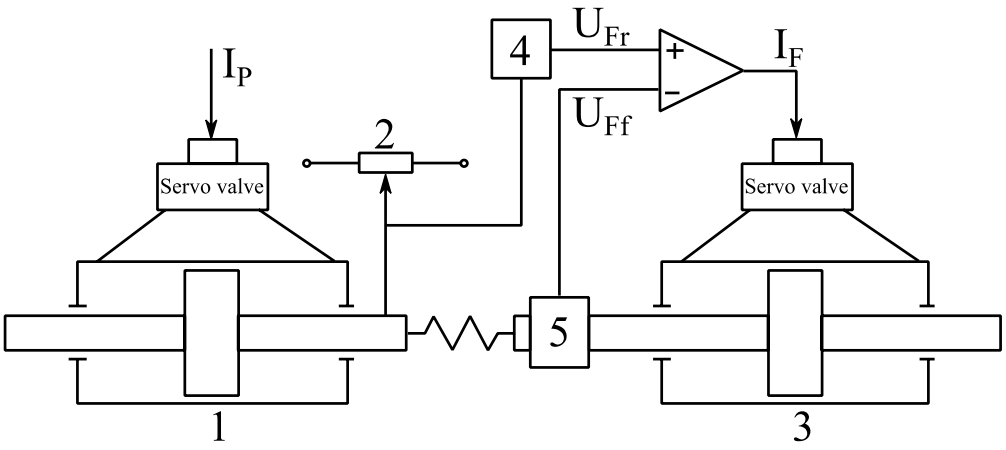

Figure 1-3 An electro-hydraulic load simulator [11]

A load simulator test bench consists of two main parts; namely, the test actuator/system under test and the load simulator. In Figure 1-3, the actuator under test, whose performance is evaluated in laboratory conditions, is labeled as (1) whereas the load simulator, which is responsible for creating the desired loads on the actuator under test, is labeled by (3). Moreover, a force feedback is obtained through a force transducer (5). In addition, two systems are connected to each other through a compliant spring arrangement, which is generally called as a *load system*. The reference loading for the load simulator can either be a set of random or predefined data [12] or the result of a dynamic simulation in real time, determined by using the motion data of the test actuator via the position transducer (2). The latter case is known as HIL (Hardware-in-the-loop) simulation [13]. In Figure 1-3, the element (4) represents the real-time hardware in which the reference load generator and the controller of the load simulator is implemented. The reference load generator and the controller are not necessarily be implemented in the same real-time hardware.

The advantages that can be expected from a load simulator test bench to test hydraulic drive systems are summarized as follows [14, 15].

- The effects of some hard-to-model characteristics of the system, such as noise, hysteresis, backlash, changes in fluid properties (e.g., bulk modulus, viscosity), on the system performance can be evaluated.
- The performance of control systems can be observed without requiring the complete system to be tested.
- The system can be tested under extreme conditions in laboratory, such as, high temperature, high loading, shock, etc.
- The system can be tested in the presence of different fault and failure conditions.
- It is time and cost efficient since it does not require the complete system to be tested.

With these advantages, load simulators are used in many application areas as experimental testing benches, e.g., seismic testing of civil engineering structures, health monitoring and fault testing of EMAs, ground testing of actuators of control surfaces of aircrafts, and development of energy efficient electro-hydrostatic (EHAs) drive systems.

Currently, a number of research studies on the development of new energy efficient hydraulic drive systems and their control algorithms are carried out in the Middle East Technical University - Automatic Control Laboratory [16, 17, 18, 19]. In one of these studies, which focuses on a variable speed pump controlled hydraulic drive system [19], a need for a load simulator is arisen so that its stability and performance tests can be carried out in a fast and economic way. Since the actuator of the system is mounted on the test bench, rather than the actual machine, any modification made on the system can be easily evaluated. The load simulator can also be used for testing different drive systems within its limits. Hence, through this load simulator, it is

expected to provide a controlled laboratory environment for the testing of new hydraulic circuit solutions and their control algorithms.

In addition to the experimental test systems, force control systems are encountered in many other applications, such as injection molding machines [20], active suspension systems [21, 22], robotic applications [23, 24], haptic simulations [25], etc. Hence, the development of some new force control strategies for these applications is a promising research area. A load simulator test bench can easily serve as a platform on which the research activities related to force control techniques can be carried out.

1.2 Literature Survey

In this section, two important points related to the electro-hydraulic force control applications are explained. These are the added compliance (low stiffness spring) between the actuators of the load simulator and the system under test and the use of velocity feedforward compensation to eliminate the strong disturbance caused by the motion of the position controlled actuator to be tested. Some examples of the load simulators used for testing of different servo systems are also presented by highlighting the points regarding the details of their drive systems, the applied control methods, and the mechanical structures of the test benches.

1.2.1 Issues Related to Electro-Hydraulic Force Control

Hydraulic control systems are used in many motion control applications such as position control or velocity control of the hydraulic actuators. They are considered to be good velocity sources even in the presence of large disturbances thanks to their high mechanical stiffness [26]. However, many researchers underlined that a mechanically compliant or low impedance actuator is required for a good force control [27, 28, 29].

Robinson [30] studied mathematically the effects of using a compliant spring in series between a closed-loop force controlled actuator and the load. Such an actuator

is called as a *series elastic actuator*. In Robinson's study, a simple, power domain independent model was initially considered to derive important conclusions and then the same analysis were performed for both hydraulic and electric actuators, separately. Due to its simplicity, this model and the derived results are presented here. The model consists of an ideal velocity source with a DC gain of K_m, a spring with stiffness k_s, and a simple proportional controller with gain K. The block diagram representation of this simple model is given in Figure 1-4. The controlled output of the system is f whereas the reference and disturbance inputs are denoted by f_{ref} and x_d, respectively.

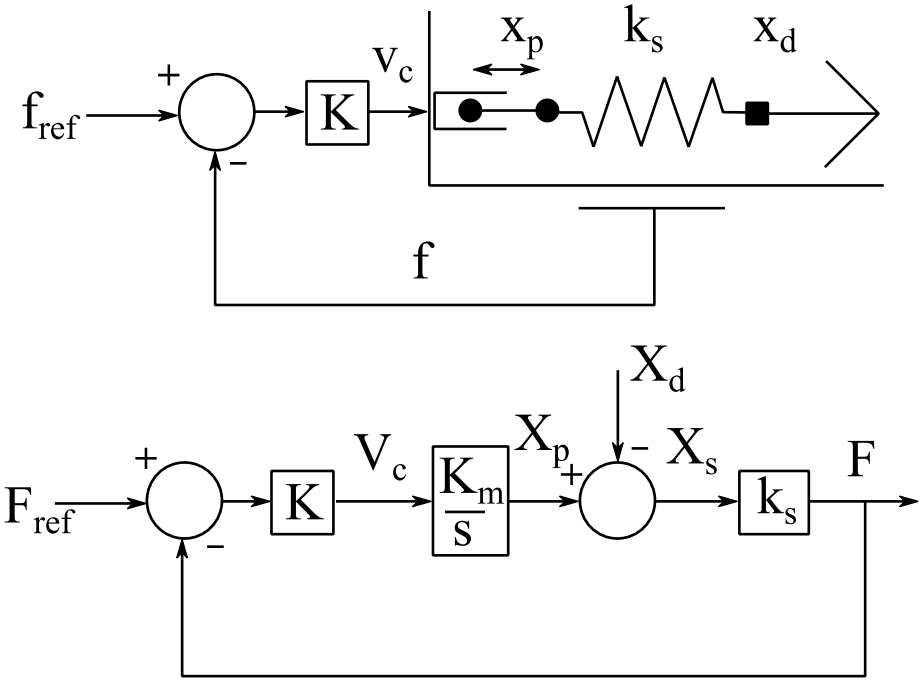

Figure 1-4 Simple model of a force controlled actuator and its block diagram [30]

From the block diagram in Figure 1-4, the input-output relationship of the simple force controlled actuator is determined as

$$F(s) = \frac{k_s K K_m}{s + k_s K K_m} F_{ref}(s) - \frac{k_s s}{s + k_s K K_m} X_d(s) \tag{1.1}$$

which can be utilized to investigate the closed-loop bandwidth and the output impedance of the system.

The following closed-loop transfer function is obtained between F and F_{ref} by neglecting the motion of the disturbance (letting $X_d = 0$)

$$G_{cl}(s) = \frac{F(s)}{F_{ref}(s)} = \frac{k_s K K_m}{s + k_s K K_m} \tag{1.2}$$

It is seen from this first order transfer function that the actuator bandwidth is directly related to the spring stiffness and controller gain. These two system parameters contribute to the corner frequency of this first order transfer function ω_c as follows:

$$\omega_c = k_s K K_m \tag{1.3}$$

From Equation (1.3), it is concluded that any decrease in the spring stiffness can be compensated by increasing the controller gain proportionally without deteriorating the bandwidth of the closed-loop system, assuming that the actuator operates within saturation limits of the control valve. One obvious advantage of decreasing the stiffness of the spring and increasing the controller gain is observed in the output impedance Z of the actuator, which is obtained by letting $F_{ref} = 0$ in Equation (1.1) as

$$Z(s) = \frac{\mathrm{F}(s)}{X_d(s)} = \frac{-k_s s}{s + k_s K K_m} \tag{1.4}$$

At low frequencies, the effect of the disturbance is minimum, which is highly desired. However, as the frequency increases, the output impedance approaches to the value of the stiffness of the spring. Therefore, decreasing the spring stiffness decreases the output impedance. In addition, the allowed increase in the controller

gain helps to keep the low impedance range unchanged since the corner frequency of Equation (1.4) is the same as the one given in Equation (1.3).

Another advantage of *taking the gain out of the sensor and putting into the control system* was highlighted by the author as the capability of the actuator to reject the motion errors [30]. This practical point was shown by introducing a noise function X_n for the motion errors of the actuator and by neglecting the dynamics of the whole system together with the disturbance load motion as seen in Figure 1-5.

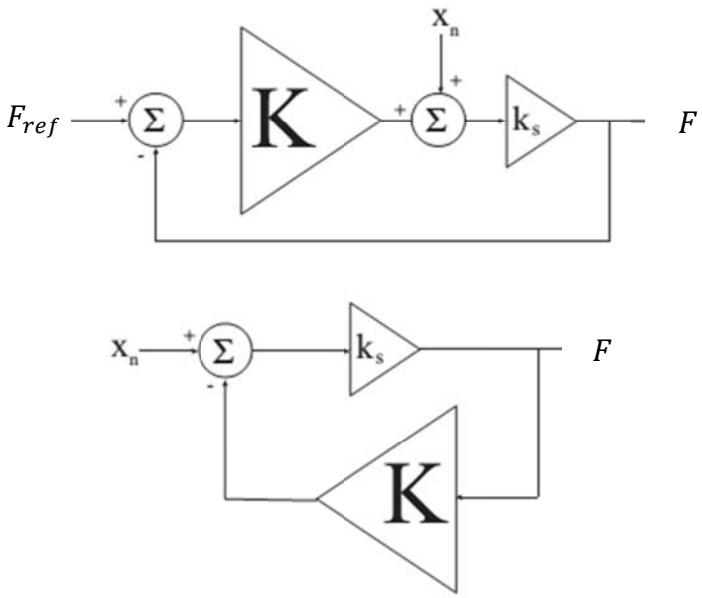

Figure 1-5 Zero order model to illustrate the effect of motion errors [30]

The transfer function between the force output F and the position noise X_n is obtained as follows:

$$\frac{F}{X_n} = \frac{k_s}{1 + k_s K} \tag{1.5}$$

It is clearly seen from Equation (1.5) that increasing the control gain by using a compliant spring attenuates the motion errors. Hence, the author concluded that high control gain provides a smooth force output.

This point was also considered by Pratt et al. [29]. They suggested the use of a compliant element between the load and the actuator in force-controlled robots in unstructured environments despite the common feeling that *stiffer is better* [29]. It was stated for a stiff connection that any small relative movement between the actuator and the load causes high force errors in the control loop and high controller gains leads to stability problems. Therefore, one is restricted to use a conservative controller gain. It was concluded that the effect of friction and inertia, in this way, cannot be compensated completely in the closed-loop system. Hence, a practical control law cannot be determined.

Another obvious advantage of using a compliant arrangement between the actuator and the load is the reduction in the shock loadings, which prevents the damage of the components of the test bench.

Besides the advantages stated above, using a serial compliance between the force controlled actuator and the load actuator results in a considerable bandwidth limitation at around limit forces of the actuator. A low stiffness spring requires large deformations to create large forces meaning that the actuator has to operate faster. However, an actuator can operate only within certain velocity and force limits. In Figure 1-6, a typical saturation curve for an actuator is given and it is represented by

$$v_p \leq V_{sat}\left(1 - \frac{f}{F_{sat}}\right) \tag{1.6}$$

where V_{sat} and F_{sat} are the no load velocity and the stall force of the actuator, respectively.

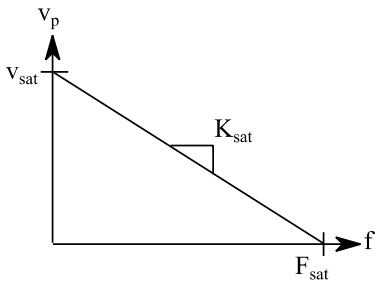

Figure 1-6 Saturation curve of the actuator [30]

If the actuator operates within its limits, the closed-loop bandwidth of the actuator is not affected by the compliance of the spring element. Nevertheless, for larger forces the closed-loop bandwidth of the system is damaged by the saturation limit of the actuator. Robinson [30] showed this force bandwidth constraint by performing an analysis of the load, which is a spring of stiffness k_s, as follows.

$$f(t) = F_{max}(\omega)e^{i\omega t} = k_s x_p(t) \tag{1.7}$$

where ω is the frequency of the loading, F_{max} is the maximum force that can be applied at a given ω, and x_p is the position of the load actuator.

Taking the derivative of Equation (1.7), the velocity of the load actuator v_p is determined.

$$v_p = \frac{1}{k_s} F_{max} i\omega e^{i\omega t} \tag{1.8}$$

By inserting Equations (1.7) and (1.8) into Equation (1.6) and getting the magnitude of the resulting expression, the following inequality is obtained:

$$\frac{F_{max}(\omega)}{F_{sat}} \leq \frac{k_s \frac{V_{sat}}{F_{sat}}}{\sqrt{\omega^2 + \left(k_s \frac{V_{sat}}{F_{sat}}\right)^2}} \tag{1.9}$$

From Equation (1.9), it is seen that with decreasing the value of k_s the achievable bandwidth at relatively large loads considerably diminishes. It should be noted that the actuator can still generate these large forces but only at lower frequencies. However, for most applications, a large bandwidth is only required for rather small forces while the bandwidth requirement decreases at higher forces. Therefore, the selection of the spring stiffness is an engineering trade off, in which bandwidth requirements must be satisfied while at the same time the added compliance should be as compliant as possible to reduce the output impedance.

The use of serial compliance in closed-loop force controlled actuators is not limited to the load simulator test. It is also encountered in closed-loop force controlled structural testing applications. For example, Sivaselvan et al. [31] suggested including a spring as a compliant element between the actuator and the structure in a structural force control application. They also presented a hydraulic actuator as a high impedance velocity source and stressed the requirement for a flexible component between the actuator and the test structure. However, they provided neither an analytical treatment nor a value for the spring stiffness in this study. The spring arrangement connecting the test structure and the actuator can be seen in Figure 1-7.

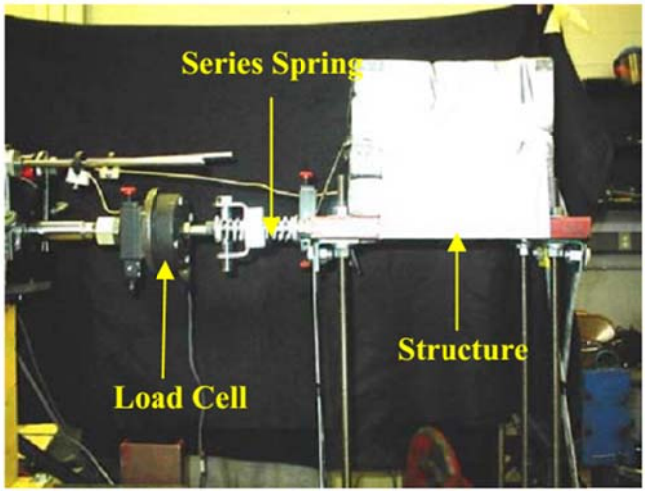

Figure 1-7 Spring arrangement between the structure and load simulator [31]

Ahn and Dinh [28] proposed and analyzed a number of ways to provide a compliant element between the hydraulic actuators of a load simulator test bench as seen in Figure 1-8. The force controlled actuator was named as the *force generator*. On the other hand, the other hydraulic actuator is called the *disturbance generator* since the force control performance of an electro-hydrostatic actuator (EHA) was primarily studied in that study. Moreover, the compliant systems were termed as the *loading system* representing the working environment of the actuators. The direct connection of the load transducer and the hydraulic actuators was called as the *rigid mode* (Figure 1-8a).

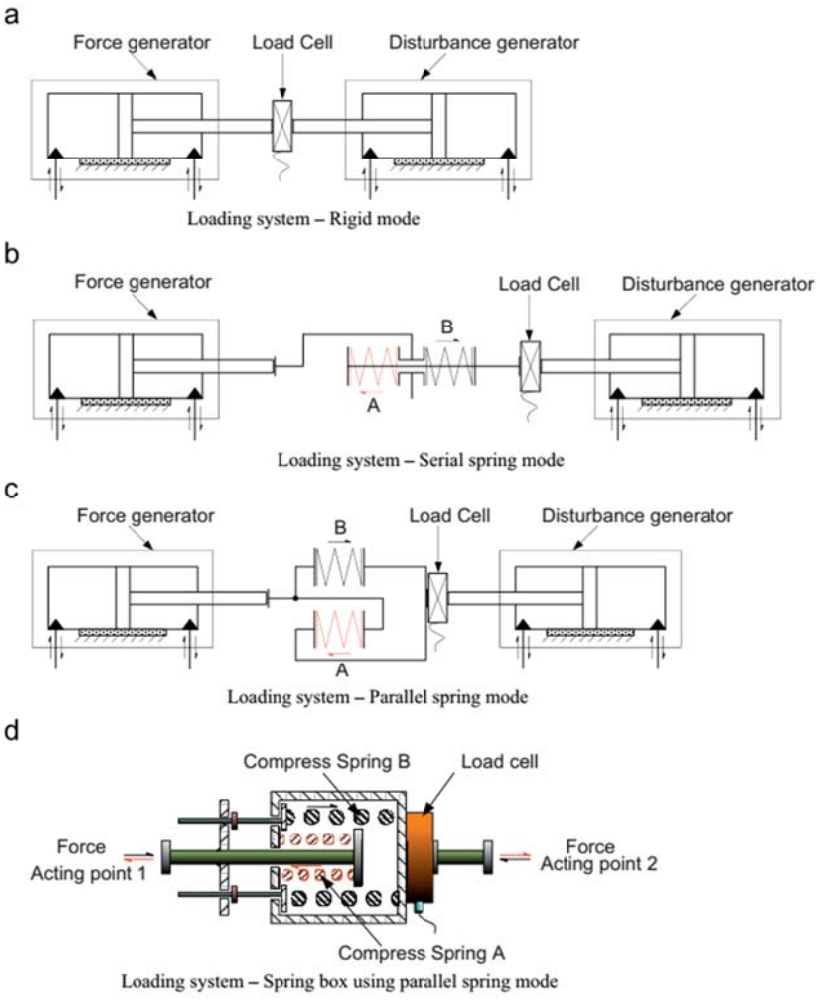

Figure 1-8 Different configurations for the loading system [28]

Because of the aforementioned difficulties encountered in the rigid mode, Ahn and Dinh considered different arrangements of two compression springs with various spring constants as the possible design solutions. The arrangement of the springs in Figure 1-8b was named as the *serial spring mode*. With this configuration, it was also aimed to have different environments in extension and retraction of the load actuator so that the performance of the controllers can be better analyzed. To illustrate this, the spring A is compressed while the load actuator is retracting whereas the spring B is at its free length. However, the authors preferred the configuration in Figure 1-8c named as *parallel spring mode* since it is more compact than the previous one while having the same functioning. The final design that they were used in their study is shown in Figure 1-8d.

Another commonly discussed issue related to the electro-hydraulic load simulation is the velocity feedforward compensation, which was extensively used by many researchers so as to improve the disturbance rejection performance of force controlled electro-hydraulic actuators [7, 32, 33, 34, 35]. Jacazio and Balossini [36] proposed the load velocity feedforward compensation scheme for the control of loading actuators of an aerospace test rig. In that study, although the performance of the test system was shown with test results, the improvement achieved by the feedforward compensation scheme was not clearly indicated.

A successful application of the velocity feedforward compensation scheme was performed by Plummer [33]. A combined force control strategy, consisting of a proportional force feedback controller G_p and a velocity feedforward compensator for the load motion $1/Q(s)$, is proposed in that study as shown in Figure 1-9. The method was applied in a Formula One test bench. It is required to simulate the aerodynamic down loads while, at the same time, the car is being tested on a four poster rig. The feedforward compensator was used to *match* the motions of the load and the actuator without resulting in large force errors. In that study, the velocity of the load was determined from the motion data obtained by an accelerometer attached to the test structure as seen in Figure 1-9. This signal was then filtered with an

inverse dynamic model of the hydraulic actuator. The author also considered the effect of the high frequency noise available in the velocity signal. Hence, the disturbance feedforward controller transfer function was designed to attenuate the high frequency noise. Finally, a proportional force feedback controller was designed by assuming a disturbance-free plant transfer function. The improvement in disturbance rejection achieved with the addition of the feedforward compensator can be seen in Figure 1-10. In that study, a compliant element between the actuator and the load is also included by emphasizing its requirement to have a certain level of *mechanical isolation*. Therefore, the load dynamics on the actuator was reduced to a single spring independent of the dynamics of the actual load. As a result, the method can be used to test different loads with different dynamics without requiring the model of the load and the re-adjustment of the controller parameters.

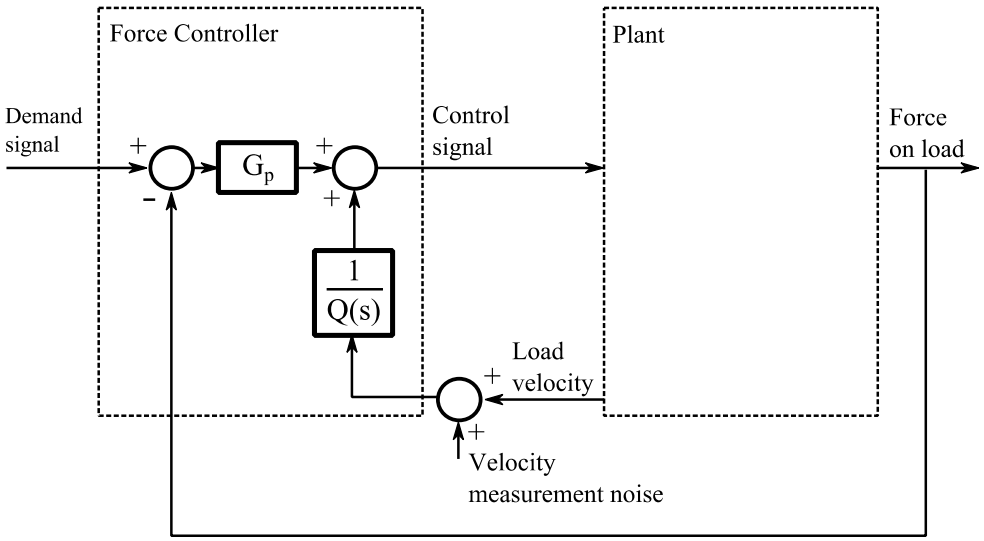

Figure 1-9 Control block diagram of the electro-hydraulic load simulator [33]

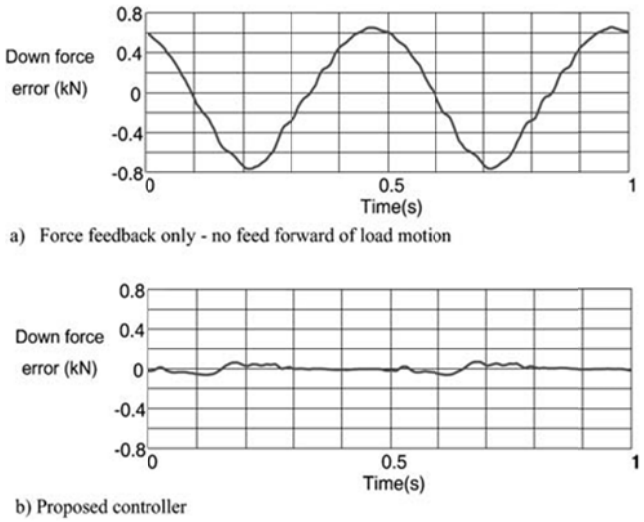

Figure 1-10 Disturbance rejection a) without, b) with velocity feedforward [33]

1.2.2 Examples of Some Load Simulators

In this section, different types of load simulators used for actuator testing are investigated and the points regarding the details of the drive systems, the applied control methods, and the mechanical structure of the test benches are reviewed. Although electro-hydraulic load simulators with linear actuators, as in this study, were commonly encountered, the examples also include load simulators with electro-mechanical linear and rotational actuators, and the ones with electro-hydraulic rotary actuators.

To begin with, the More Electric Aircraft (MEA) concept in aerospace industry increased the importance of electro-mechanical actuators as the primary and secondary flight control actuators [37]. Hence, there are many research activities for the development of electro-mechanical actuators (EMAs) in aerospace industry. To illustrate, Smith et al. [9] designed an EMA test bench in the NASA Ames Research Center. In addition to the performance tests of EMAs, it was aimed to test health monitoring algorithms on that test bench. An overall view of the test bench is given

in Figure 1-11a. Two electro-mechanical actuators, one as a load simulator and the other as a test actuator, were mounted on a structural I-beam with the help of two L-shaped brackets. The load actuator was capable of applying 50 kN of force. It was stated that both the mounting beam and the brackets were designed to have high bending stiffness so that the structural deflections under the maximum loading could not affect the test results. However, the resulting design was considerably massive and its transportation was highly problematic. In addition, the surface of the beam was machined with high precision in order to provide a good alignment of the actuators, which required a highly developed machining facility. As seen in Figure 1-11b, an attention was also given to the proper alignment of the load and test EMAs. A rod-end coupling was utilized to tolerate the lateral and spherical misalignments. In addition, thread adapters were used between the test cell and the test EMA and between the coupling and load EMA. The test bench also included a power supply system (for the transducers and servo-drives), two controllers and a data-acquisition (DAQ) system. In Figure 1-12, the schematic view of the test bench is given showing the interactions of the axes controllers and DAQ system with the EMAs. The load simulator was primarily equipped with a linear position transducer and a

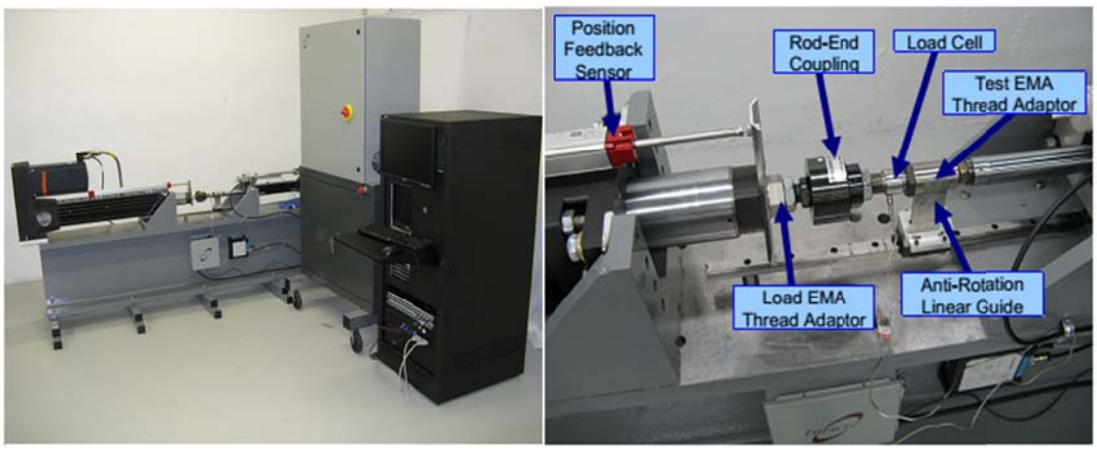

Figure 1-11 a) EMA test bench in NASA Ames,
b) Coupling of the load and test EMAs [9]

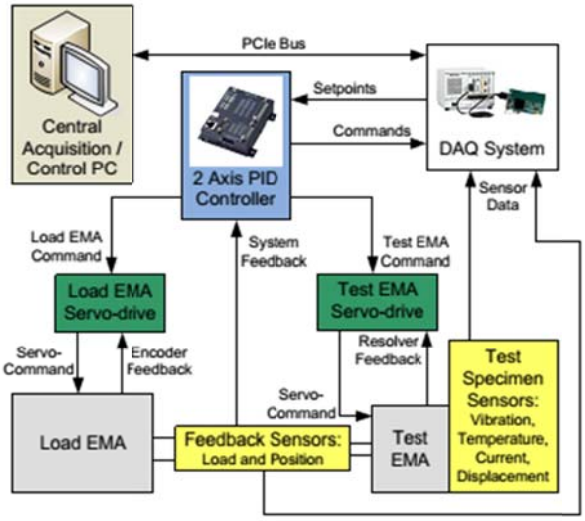

Figure 1-12 Schematic of the EMA test bench [9]

bi-directional force transducer. On the other hand, the actuator under test had more transducers to accurately represent its health state, such as, thermocouples, accelerometers, and a laser position transducer. The test bench was designed to allow the user to specify custom force and motion profiles for the load and test actuators, respectively. In order to track the specified references, two PID (Proportional-Integral-Derivative) controllers were used in the test bench with proper feedback signals (Figure 1-12) and the outputs of the controllers were utilized to drive the EMAs. However, the details of the controller design were not explained in that study.

Karpenko and Sepehri [32] studied an electro-hydraulic load simulator of a hardware-in-the-loop test bench, which is used to emulate the operational loads on a flight actuator. The loads to be applied onto the test actuator were determined from the simulated flight maneuvers. The test and load actuators were connected to each other through a guided connector, an S-shaped force transducer ($22\ kN$), and a spring arrangement (Figure 1-13). In addition, an optical rotary encoder provided the position feedback for the position controlled flight actuator. In that study, a desktop computer with required I/O and encoder modules was utilized as the DAQ system and the control computer. Both of the actuators were controlled by servo-valves. A

single hydraulic power source with a variable displacement pump provided the required power for both of the actuators as seen in Figure 1-13b. The maximum force output was approximated as $F_{max} = 7.3\,kN$ assuming that the maximum power available to load when the pressure drop through the servo valve was about $2/3P_s$. The proposed control system for the load simulator in that study consisted of three separate controllers, namely, a feedback controller, a pre-filter, and a displacement compensator. Designs of the feedback controller and the pre-filter were performed by using quantitative feedback theory. The deterioration in the force tracking performance of the load simulator due to the motion of the position

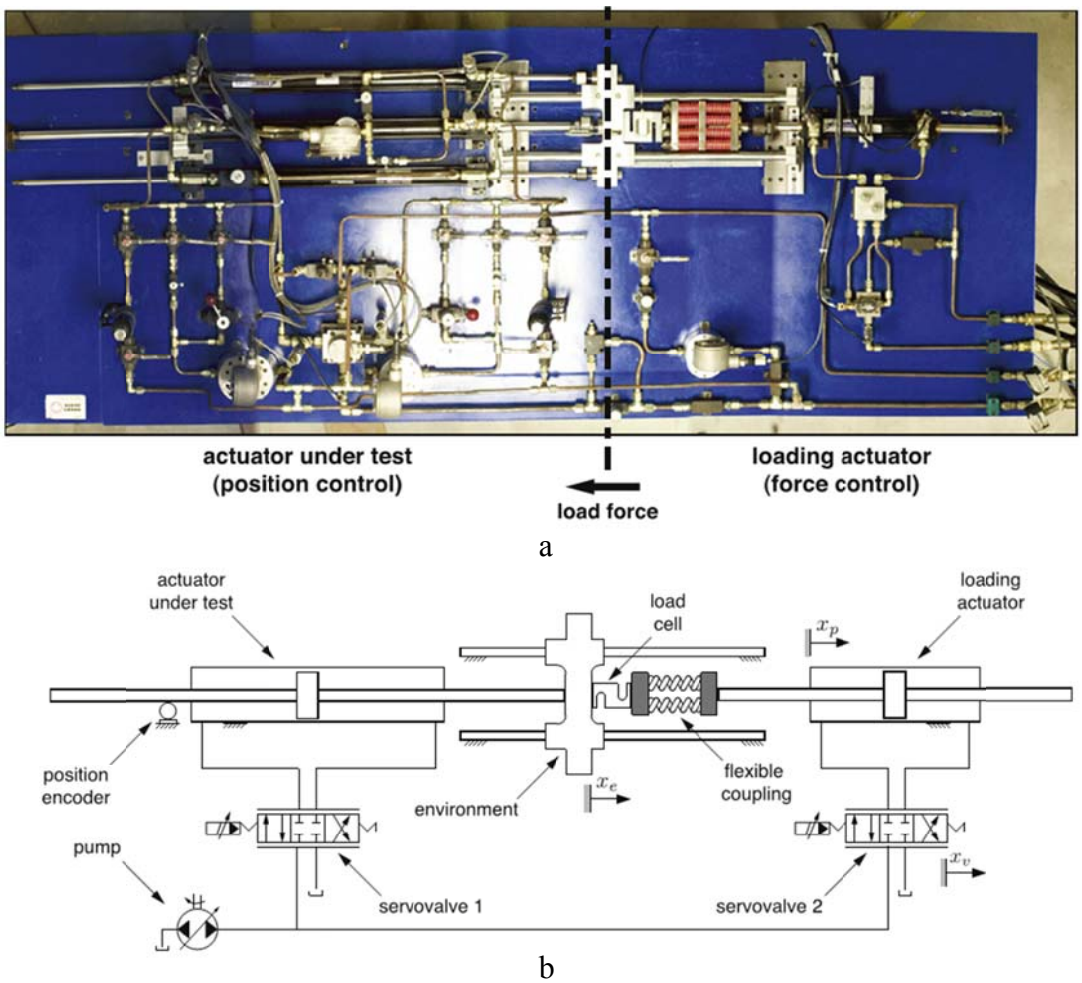

Figure 1-13 a) A photograph and b) a schematic view of the test bench [32]

controlled flight actuator was eliminated via a displacement compensator. Experiments were carried out with and without the disturbance compensator. The disturbance rejection performance of the compensation was evaluated by applying a step command of $5\,mm$ to the actuator under test. For this disturbance input, the maximum observed force error was about $0.6\,kN$ and about $0.3\,kN$ without and with displacement compensator, respectively. The authors also stated a $30\,\%$ improvement in the settling time according to $2\,\%$ criteria. Hence, the results showed that the force tracking performance of the load simulator was considerably improved with the addition of the velocity compensation.

Zongxia et al. [38] studied the hydraulic torque control problem on a load simulator test bench, whose schematic view is given in Figure 1-14. Two hydraulic motors were used as the load and test actuators, and they were controlled by two servo-valves. The test actuator was controlled to track a reference position input and an angular transducer was available for the feedback as seen in the figure. On the other hand, the closed-loop torque controlled load actuator was expected to track a reference torque command with a feedback from a torque transducer. The details about the mechanical structure/connections of the test bench are not available in the study. However, authors discussed the heavy disturbance of the test actuator on the performance of the load actuator in detail. Although they pointed the velocity feedforward compensation scheme as a suitable method to this problem, they proposed a more direct approach, named as *velocity synchronizing control,* which made use of the control signal to the servo-valve of the test actuator rather than its velocity. In that way, it was aimed to eliminate phase lag caused by the feedforward compensator, which was an inverse dynamic model of the hydraulic system. A detailed non-linear mathematical model of the load simulator was obtained and the improvement achieved with the proposed method was shown with the experimental results. To illustrate, for a $10\,Hz$ sinusoidal disturbance input, the torque error decreased from $75\,Nm$ to $5\,Nm$ with the addition of the compensator. The

effectiveness of the method was clearer at high frequencies. The method is appealing especially when the both systems share the same mathematical model.

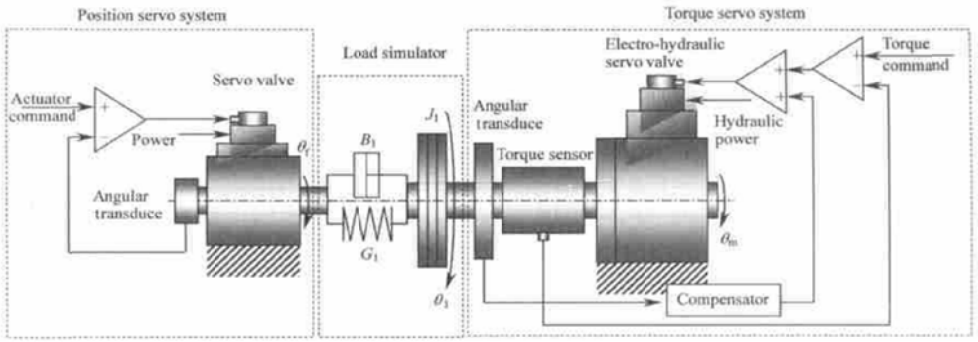

Figure 1-14 A schematic view of the torque load simulator [38]

Kashi et al. [39] introduced their hydraulic test rig which was used for the investigation of the performance of active suspension systems. As seen in Figure 1-15, the load actuators were mounted to a closed structure and the actuators of the active suspension system are connected between them.

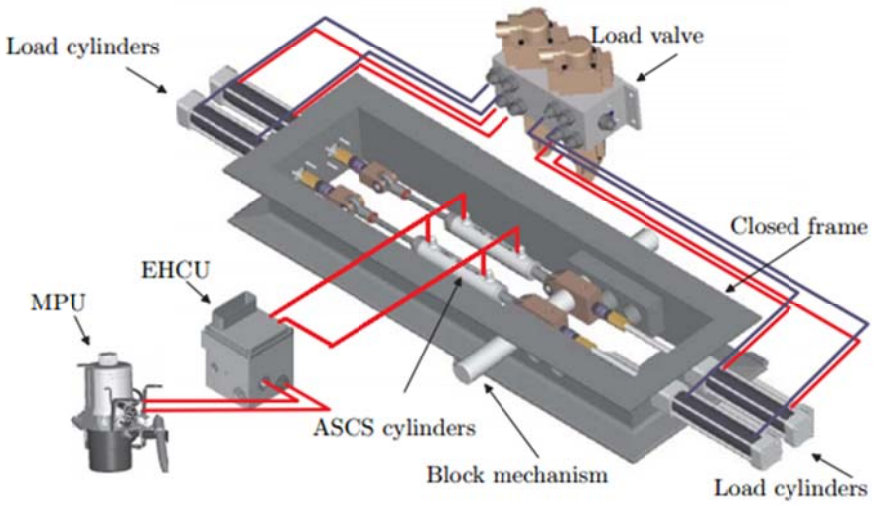

Figure 1-15 Active suspension test bench [39]

The closed structure design of the test bench did not allow the forces to be transferred to the environment. Hence, the test bench could easily be transported and mounted on any platform. The loads to be applied to the suspensions were determined from the real time simulation of the vehicle dynamics via dSPACE and controlled by a valve controlled system.

Although the conventional valve controlled hydraulic systems are well-known with their high power to weigh ratio and very high speed of response, their very low energy efficiency is considered as a crucial drawback for today's engineering systems. Therefore, there is a great research activity in literature to eliminate the valve losses in variable displacement or speed pump controlled hydraulic systems. In order to provide a platform to study and improve the force and position control performance of such an energy efficient hydraulic system, Ahn and Dinh [20] designed an electro-hydraulic testing machine. Two hydraulic systems controlled by variable speed pumps were connected two each other (Figure 1-16). The

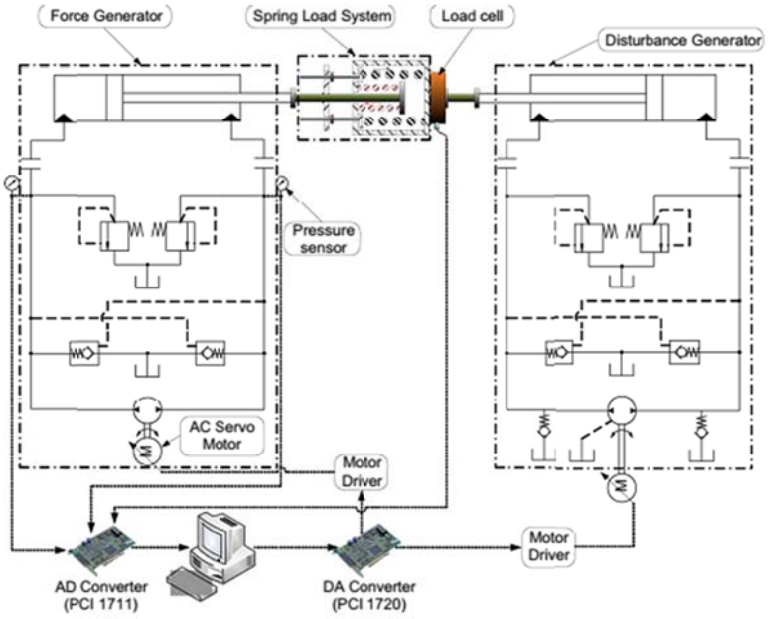

Figure 1-16 Schematic view of the EHA test machine [20]

load simulator was named as the *force generator*, whereas the position controlled system was named as the *disturbance generator* since the objective was to study the force control problem for an energy efficient hydraulic system. Different spring arrangements, named as spring load system, were discussed in that study to provide a certain degree of compliance between the actuator under test and the load simulator. The inner and outer springs had the spring constants of $720\ N/mm$ and $519\ N/mm$, subject to a maximum force of $8.6\ kN$ and $4.7\ kN$, respectively. A force transducer with a capacity of $50\ kN$ was used to provide the required feedback for the force control. In addition, a PC (Personal Computer) was utilized as the control computer equipped with the required data acquisition and control cards. A two degree-of-freedom robust adaptive control strategy was proposed with a feedback controller and a pre-filter and its results were compared with those obtained when a classical PID controller was used. The proposed method was particularly effective in terms of steady state performance, but its transient performance was only comparable with that of the PID controller. The test bench was highly flexible since it allowed the development of different control strategies for the developed hydraulic circuit solutions.

1.3 Objective of the Thesis

The main objective of this thesis is to develop an electro-hydraulic load simulator to carry out the performance and stability tests of newly developed hydraulic drives and control systems in controlled laboratory conditions. With the help of this load simulator, it is aimed to eliminate the strong need for an actual plant to be readily built or available so as to evaluate the performance and stability of these systems.

The design and control of the hydraulic load simulator are to be performed to satisfy the given requirements. The resulting system should be tested to indicate its actual limits clearly. A simulation model will also be developed as an off-line tool available to the user to foresee the results before performing the experiments on the test bench.

1.4 Thesis Outline

In this chapter, load simulators are introduced as experimental loading units used in actuator or structural testing systems. The main components of these test benches are explained and the advantages of using a load simulator test bench in the development of new systems are discussed. In literature review, two commonly discussed issues in the field of electro-hydraulic force control, namely the use added compliance between the actuators of the load simulator and the actuator under test, and the use of velocity feedforward controller are considered. In addition, some selected examples of load simulators from the literature are investigated in terms of their drive systems, control topologies, and the mechanical structures of the test stands. Finally, the objective of this thesis study is presented.

In Chapter 2, the development of an electro-hydraulic load simulator is presented. The sizes of the hydraulic components and the stiffness of the spring load system are determined according to the design specifications. The feedback transducers and the real-time target machine, which is used as DAQ system and the control computer of the load simulator, are introduced. The construction of the test bench to accommodate the actuators of the hydraulic load simulator and the drive system under test are presented. The final view of the constructed test bench together with the load simulator and the hydraulic drive system under test are shown and the main components of the test bench are labeled on its photographs.

In Chapter 3, a non-linear mathematical model of the electro-hydraulic load simulator is developed and a simulation model is constructed by using MATLAB®/Simulink®. Most model parameters are obtained from the technical drawings and catalogs of the components. The friction characteristic of the hydraulic actuator is determined by some performing open-loop experiments. The validity of the model with these parameters is also shown by performing some open-loop experiments and comparing them with simulation results.

In Chapter 4, the non-linear mathematical model obtained in the previous chapter is linearized around a critical operating point. The linearized model is utilized in order to design a combined feedforward and feedback controller. A proportional feedback controller for the force control loop is selected and a reference feedforward is designed to improve the force tracking performance of the system. A disturbance feedforward controller is also designed in order to reduce the strong disturbance caused by the motion of the hydraulic drive system under test. Since only the actuator position of the hydraulic drive system under test is measured by a linear encoder, its velocity is estimated for using in the disturbance feedforward controller. A Kalman filter with a kinematic model is designed and tuned to accurately estimate the velocity of the actuator.

In Chapter 5, the performance of the electro-hydraulic load simulator is investigated by conducting some real-time experiments and by comparing their results with model responses. Disturbance rejection and force tracking performances of the electro-hydraulic load simulator are evaluated by performing a set of frequency response tests. The saturation limits of the hydraulic system of the load simulator are investigated by applying reference sinusoidal force inputs of various magnitudes and frequencies. Force and spool position responses of the non-linear simulation model are also presented in order to show that the simulation model can be utilized as an offline test platform before performing real-time experiments.

In Chapter 6, the whole design process of the electro-hydraulic load simulator and the results are summarized, conclusions reached are presented, and some possible research points for future studies are discussed.

CHAPTER 2

DEVELOPMENT OF THE ELECTRO-HYDRAULIC LOAD SIMULATOR

An electro-hydraulic load simulator and a test bench is developed in this thesis so as to carry out the performance and stability tests of hydraulic drive systems in controlled laboratory conditions. In this chapter, the development of the electro-hydraulic load simulator is explained in detail. This mainly includes the development of a valve-controlled electro-hydraulic loading system with its real-time control hardware, and the construction of a test bench to accommodate the actuators of the load simulator and the hydraulic drive system under test.

In Section 2.1, the design specifications are given. A brief description of the overall system is given in Section 2.2. The development of the electro-hydraulic loading system and the hydraulic components utilized in this study are explained in Section 2.3. The selection of the spring constant for the load system is also explained in this section. In Section 2.4, the control hardware including a real-time control computer and feedback transducers is presented.

In Section 2.5, the test bench constructed in order to accommodate the actuators of the electro-hydraulic load simulator and the hydraulic drive system under test is introduced. In Section 2.6, a set of photographs showing the final view of the electro-hydraulic load simulator test bench are supplied, and its main components are labeled on them.

2.1 Requirements for the Electro-Hydraulic Load Simulator

An electro-hydraulic load simulator with its test bench is to be designed and constructed in order to satisfy the following requirements.

- The test bench should provide a mean for the direct connection of the actuators of the load simulator and the system under test with a minimum axial misalignment.
- The test bench should accommodate a single rod hydraulic actuator as an initial test specimen, whose main dimensions can be seen in Appendix C.
- The allowable operating region in the $F - v_d$ plane for the system under test is defined in Figure 2-1. The load locus of the system under test is restricted within a region limited by a maximum power of $0.75\,kW$, a velocity of $100\,mm/s$, and a maximum force of $15\,kN$. The frequencies of the sinusoidal forces that the load simulator should apply at the maximum velocity and the loading of the actuator under test are specified as $\omega = 1.75\,Hz$ and $\omega = 1\,Hz$, respectively.

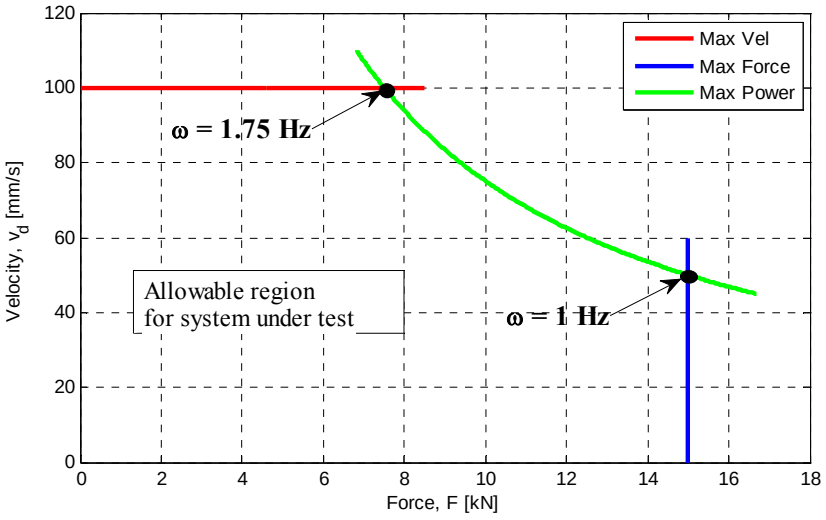

Figure 2-1 Allowable region for the system under test

- The bandwidth of the load simulator should reach 10 Hz for relatively small loading conditions of the actuator under test (1 kN at 10 Hz).
- The user should be able to specify some custom load force profiles.

2.2 Description of the Test Bench

A schematic view of the test bench is given in Figure 2-2. As seen in the figure, the actuators of the load simulator and the hydraulic drive system under test are fixed to a bench to provide a mechanical support for applying the desired test loads. Two actuators are connected to each other through a compliant spring arrangement (spring load system) and a force transducer. The force transducer provides a feedback signal for the closed-loop control of the load simulator. On the other hand, the spring load

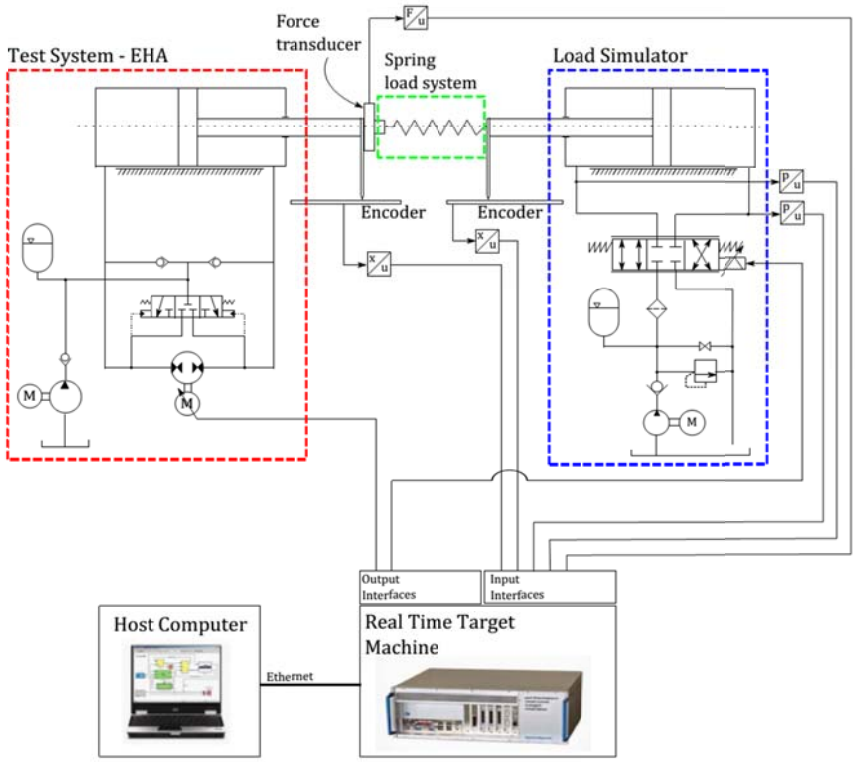

Figure 2-2 A schematic view of the load simulator and the test bench

system is introduced to attenuate the effect of the strong disturbance of the test actuator on the performance of the load simulator. In addition to the force transducer, two position and two pressure transducers are also utilized in the test bench. One of the position transducers is used to measure the position of the actuator under test. The output of this transducer is used in a disturbance feedforward controller. Other transducers are available only for monitoring purposes. The hydraulic circuit layouts of the valve-controlled load simulator and the variable speed pump controlled hydraulic drive system under test are given in dashed blue and red rectangles, respectively. A valve controlled hydraulic system is considered for the load simulator due to its high performance relative to pump controlled drives. Connections of the transducers and the driver of the flow control valve with the real time control computer through its various input and output interfaces are also indicated in Figure 2-2.

2.3 Development of the Hydraulic Load System

In this sub-section, the development of the hydraulic load system is explained in detail. In Figure 2-3, the layout of the valve controlled electro-hydraulic load simulator is given. It consists of a proportional control valve, a differential hydraulic actuator, and a spring arrangement. The valve operates with a constant supply pressure p_s and its return is connected to the tank p_t. The supply pressure is initially selected to ensure that the hydraulic actuator can deal with the operational loads. The flow control valve and the stiffness value of the load system are selected to satisfy the given requirements. In addition, the design of the hydraulic power pack which is constructed to provide the required flow rate at the selected supply pressure p_s is explained with its hydraulic circuit elements.

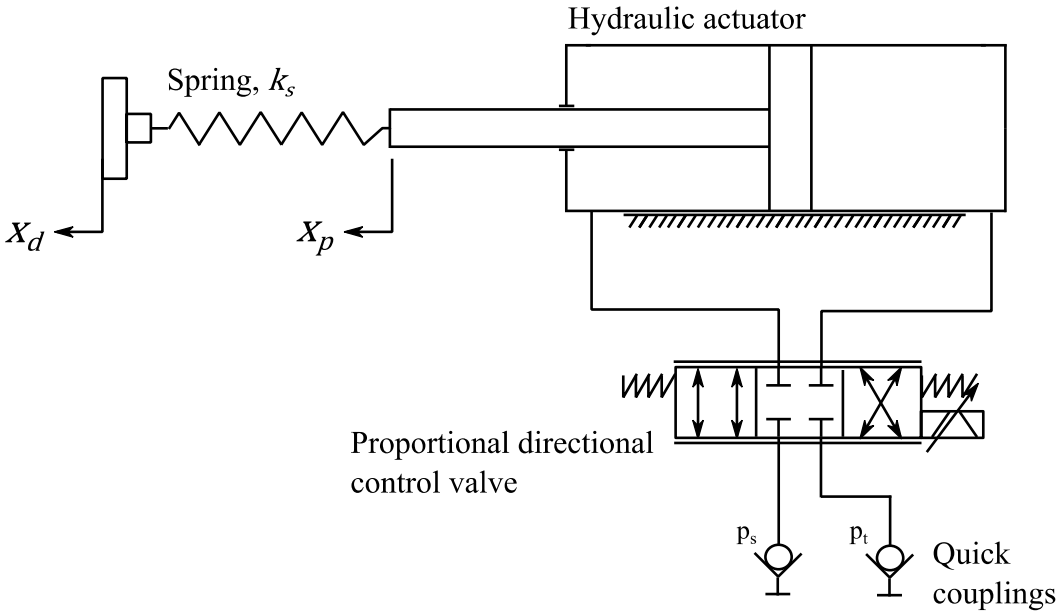

Figure 2-3 Layout of the valve-controlled electro-hydraulic load simulator

2.3.1 Selection of the Supply Pressure and Hydraulic Actuator

The selection of the supply pressure of a hydraulic control system operating at constant pressure is one of the first design steps [40]. A high supply pressure is desirable since less flow is then required in order to deliver a specified power to the load. On the other hand, two factors limit the use of very high supply pressures, namely, increased leakage and noise and decreased component life. Therefore, for most industrial systems, generally a supply pressure between 35 and 140 bar is selected [40]. However, the final value of the supply pressure should be determined at the same time with the size of the hydraulic actuator to handle the expected loads.

In this study, a Hanchen 120 series differential hydraulic actuator is used as the actuator of the load simulator since it has been made available to the research team by the department. The specifications of the hydraulic actuator are given in Table 2-1.

Table 2-1 Hydraulic actuator specifications

Piston diameter	$60\ mm$
Rod diameter	$30\ mm$
Stroke	$200\ mm$
Maximum operating pressure	$150\ bar$
Overall mass	$10.5\ kg$
Piston rod mass	$2.7\ kg$

In many applications, differential actuators are commonly preferred because of their compact design, low cost, and easy use. However, they exhibit an inherent nonlinearity due to their different pressure areas for rod and piston sides and this leads to different the steady state velocities of the hydraulic piston in extension and retraction phases for the same valve openings.

The following equation can be utilized to determine the required supply pressure for the actuator to handle the dynamic operational loads [40]:

$$p_L = \frac{m_p\left(d^2x_p/dt^2\right) + b_p(dx_p/dt) + k_s(x_p - x_d)}{A_p} \tag{2.1}$$

Here, it can be assumed that the maximum acceleration, velocity, and spring force occur at the same time with a very conservative approach. The maximum force requirement is set as $F^{\max} = k_s\Delta x^{max} = 15\ kN$. Some reasonable values are assumed for the maximum velocity and acceleration of the actuator as $\dot{x}_p = 250\ mm/s$ and $\ddot{x}_p = 15000\ mm/s^2$. In addition, it is reasonable to assume that load pressure p_L never exceeds $2p_s/3$. This last assumption is desirable since as p_L approaches to p_s, the actuator tends to stall and hence the flow gain decreases

leading the system to lose control [40]. The mass of the hydraulic piston with the addition of connector parts is $m_p = 8\ kg$. A reasonable value for the viscous friction coefficient is assumed as $b_p = 6.5\ Ns/mm$. Considering the rod side pressure area of the hydraulic actuator $A_B = 2121\ mm^2$, the minimum supply pressure required is determined as $p_s \geq 118\ bar$. Therefore, a supply pressure of $p_s = 120\ bar$ $(12\ MPa)$ is selected in this study.

2.3.2 Selection of the Spring Constant and Flow Control Valve

The selection of the spring constant is a highly crucial design step for the development of a series elastic actuator to be used in closed-loop force control applications. The addition of series compliance between the actuators of the load simulator and the system under test has the distinct advantage of reducing the output impedance $Z(s) = F(s)/X_d(s)$. Therefore, the effect of this strong disturbance caused by the motion the system under test is considerably reduced. However, the flow requirement drastically increases with decreasing spring stiffness as larger deformations are required so as to generate the same forces. Since this also increases the size of the flow control valve, a load analysis with various spring stiffness values is performed by considering the flow-pressure saturation limits of different proportional flow control valves.

The flow-pressure characteristics (saturation curve) of a flow control valve used with a differential actuator are expressed by the following equations [41]:

- For extension of the actuator,

$$v_p = g\frac{1}{A_A\sqrt{1+(A_A/A_B)^3}}\sqrt{p_s - F/A_A} \tag{2.2}$$

- For retraction of the actuator,

$$v_p = g \frac{1}{A_A \sqrt{1 + (A_A/A_B)^3}} \sqrt{(A_A/A_B)p_s + F/A_A} \tag{2.3}$$

where g is the hydraulic conductance of the valve at its full opening per metering edge.

In this study, three different proportional control valves available in the catalog of Parker Hannifin are considered. The valves are rated at a pressure drop of 35 bar (3.5 MPa) per metering edge as 16 lpm ($0.27 \cdot 10^{-3}\ m^3/s$), 25 lpm ($0.42 \cdot 10^{-3}\ m^3/s$) and 40 lpm ($0.67 \cdot 10^{-3}\ m^3/s$). By using Equations (2.2) and (2.3), the characteristic curves of these valves at the supply pressure $p_s = 120\ bar$ are plotted in Figure 2-4 for extension and retraction cases, separately.

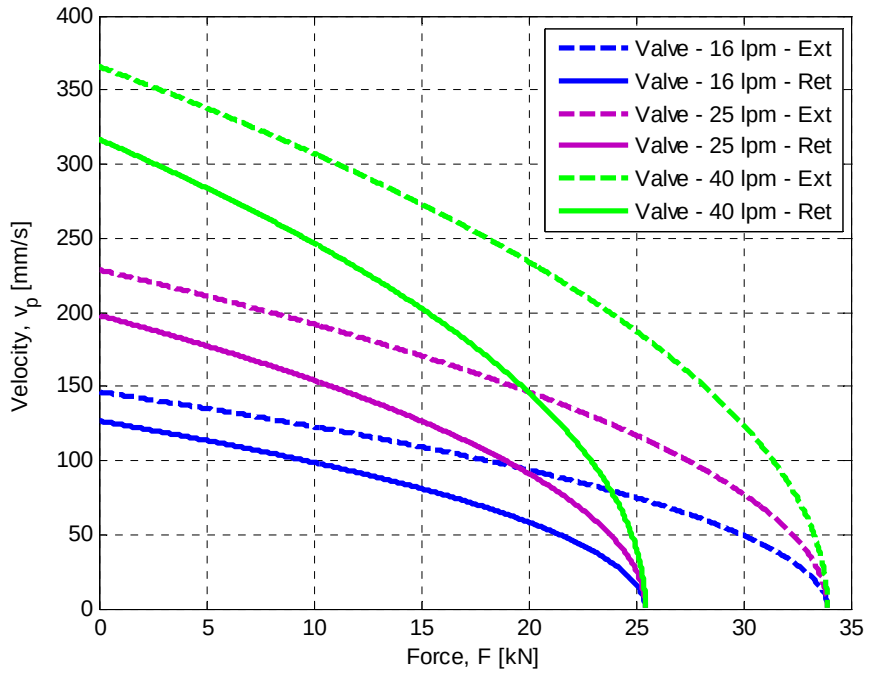

Figure 2-4 Characteristic curves of valves with different flow ratings

As seen in Figure 2-4, the retraction case limits the achievable performance of the hydraulic system. Therefore, while selecting the control valve and the value of the

spring constant of the load system the retraction plots are considered in the analysis. The extension case determines the requirements for the power supply.

In order to apply the desired loads onto the actuator under test, the motion of the hydraulic load simulator should be expressed as follows:

$$x_p(t) = X_0 \sin \omega t + x_d(t) \tag{2.4}$$

$$v_p(t) = X_0 \omega \cos \omega t + v_d(t) \tag{2.5}$$

where X_0 and ω are the amplitude and frequency of the oscillations of the load actuator, respectively. The position and velocity of the disturbance actuator are denoted by x_d and v_d, respectively.

In the analysis, the effects of inertia and friction are neglected since force associated with them are relatively small as compared to the spring force $F(t)$, which can be inferred from Equation (2.1). Then, the force applied by the load actuator is determined as follows:

$$F(t) = k_s\big(x_p(t) - x_d(t)\big) = k_s X_0 \sin \omega t \tag{2.6}$$

Equations (2.5) and (2.6) are initially squared and then summed to yield to

$$\frac{\big(v_p - v_d\big)^2}{(X_0 \omega)^2} + \frac{F^2}{(k_s X_0)^2} = 1 \tag{2.7}$$

By using Equation (2.7), the load loci for different stiffness values of the load system are plotted in Figure 2-5 by considering the limit loadings specified in Section 2.1. In the figure, the pressure – flow characteristics of the valves given in Figure 2-4 are also plotted.

As can be seen in Figure 2-5 and Figure 2-6, as the stiffness of the spring between the actuators of the load simulator and disturbance actuator is decreased, the required

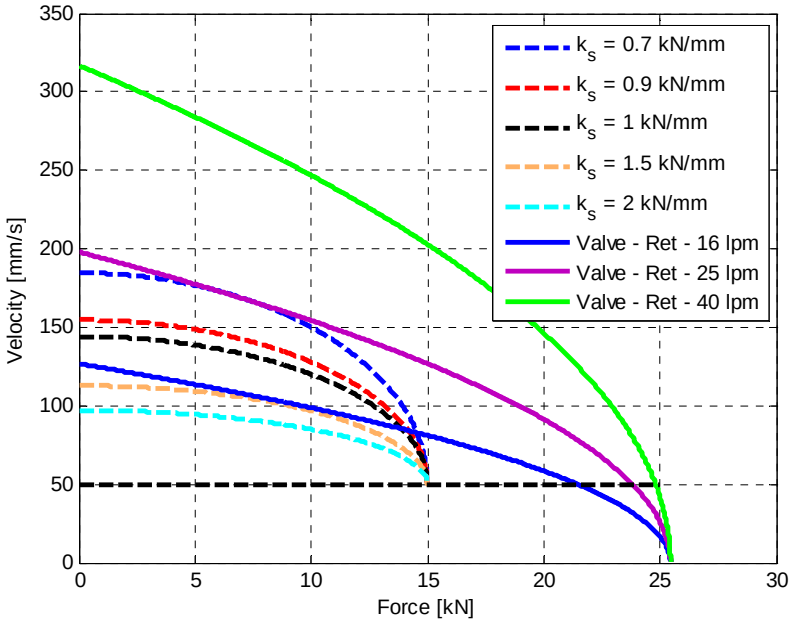

Figure 2-5 Load loci for different spring constants - $F = 15$ kN at $\omega = 1$ Hz and $v_d = 50\ mm/s$

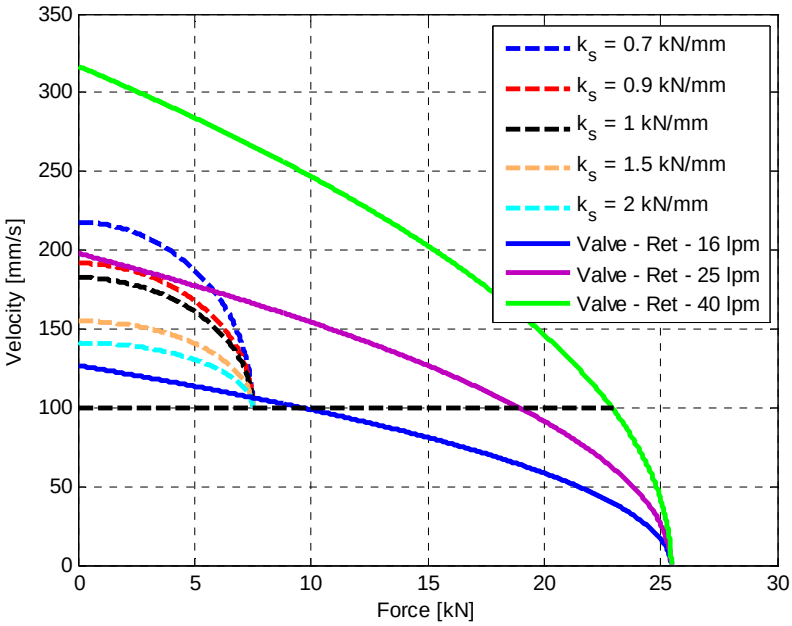

Figure 2-6 Load loci for different spring constants - $F = 7.5\ kN$ at $\omega = 1.75\ Hz$ and $v_d = 100\ mm/s$

flow rates to apply the desired forces at specified frequencies considerably increase. Thus, it requires the use of valves with higher flow capacities. However, it is desired to select the smallest sized flow control valve possible in order to keep the size of the hydraulic power pack as compact as possible to reduce the overall development cost. Therefore, first the valve with the lowest flow capacity should be considered.

From Figure 2-5, it is seen that with the valve rated as $16\ lpm$, the requirement investigated in that plot can be achieved if spring stiffness value greater than $1.5\ kN/mm$ is selected. On the other hand, the requirement given in Figure 2-6 cannot be satisfied with this valve and spring selections. At that point, it is required to either increase the stiffness of the load spring system or select a flow control valve with higher capacity. In Appendix D, the extra stiff springs available in the catalog of a die spring producer is given. The highest stiffness value in the catalog is $952\ N/mm$. However, the stiffest one readily available in the market was the one with a stiffness value of $565\ N/mm$. Even a parallel combination of two of these springs cannot lead to a stiffness value greater than $2\ kN/mm$, thus further complicated spring arrangements are required to achieve this stiffness value. In addition, it is not reasonable to limit the maximum velocity of the load system to $125\ mm/s$ which is slightly greater than the system under test and to further increase the output impedance of the load actuator.

The next valve in the catalog, which has a flow rating of $25\ lpm$, is considered. It is observed in Figure 2-5 and Figure 2-6 that with the use of this valve and a spring load system having an equivalent stiffness of $1\ kN/mm$ satisfies both requirements given these figures. Therefore, two of this hardest spring that is readily available in market are gathered and the springs are decided to be used in parallel connection to lead to an equivalent stiffness of $2 \cdot 565\ N/mm = 1130\ N/mm$. A mechanical arrangement is constructed to operate the springs in parallel connection.

The ordering code of the selected proportional directional control valve ($25\ lpm\ at\ 35\ bar\ per\ metering\ edge$) of Parker Hannifin is D1FPE50HB9NB5

[42]. A cross-sectional view of the valve is given in Figure 2-7. It converts an electrical command input into a proportional spool stroke. In order to achieve a high dynamic response, its driver performs a closed-loop position control by taking the actual spool position as the feedback. It is a critically (or zero lapped) lapped valve. That is, the width of lands on the spool is the same as the width of the ports on the slave of the valve. The wiring diagram of the valve driver is given in Appendix A.2.

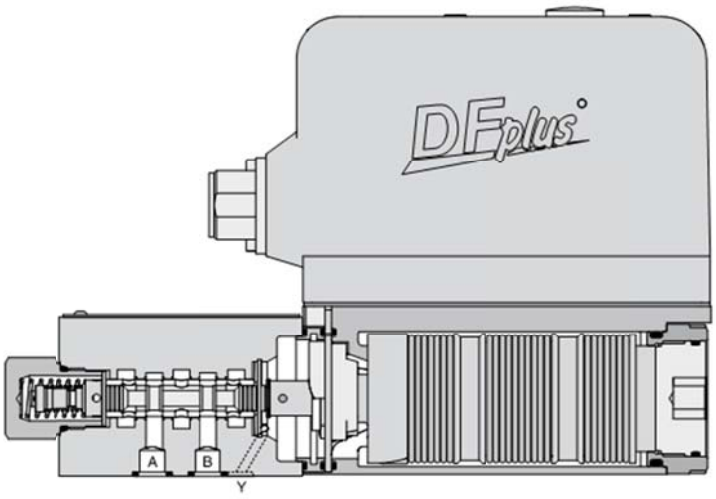

Figure 2-7 Cross-sectional view of the Parker DFplus proportional directional control valve [42]

In Figure 2-8, the allowable operating region for the system under test and the loading limits of the electro-hydraulic load simulator are plotted together. In this figure, it is shown that the loading system is capable of applying the desired loads at specified frequencies while the system under test is within the allowable region.

The load loci for different loading conditions when $\dot{x}_d = 0\, mm/s$ is illustrated in Figure 2-9. The saturation curve of the selected flow control valve is also shown in

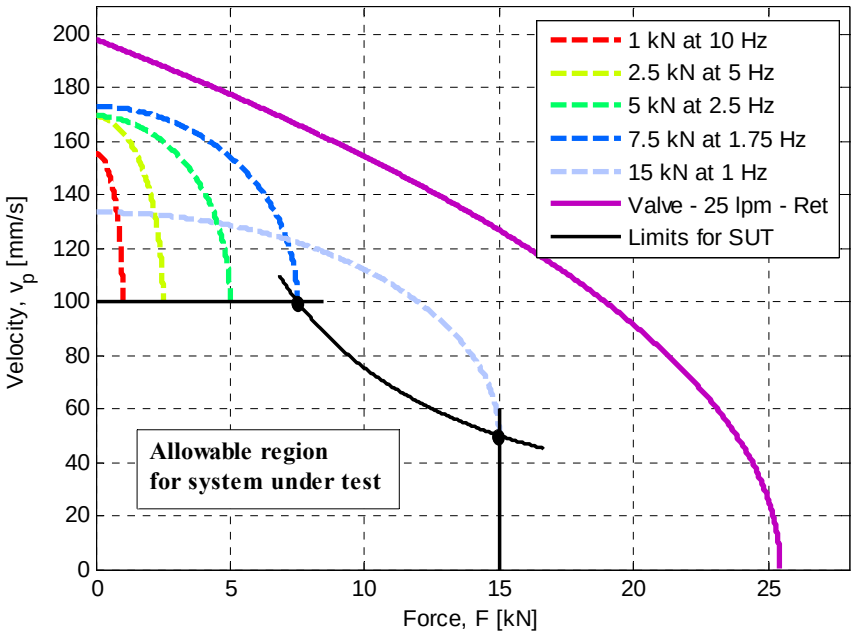

Figure 2-8 Allowable operating region for the system under test and load loci for the load simulator ($k_s = 1130\ N/mm$)

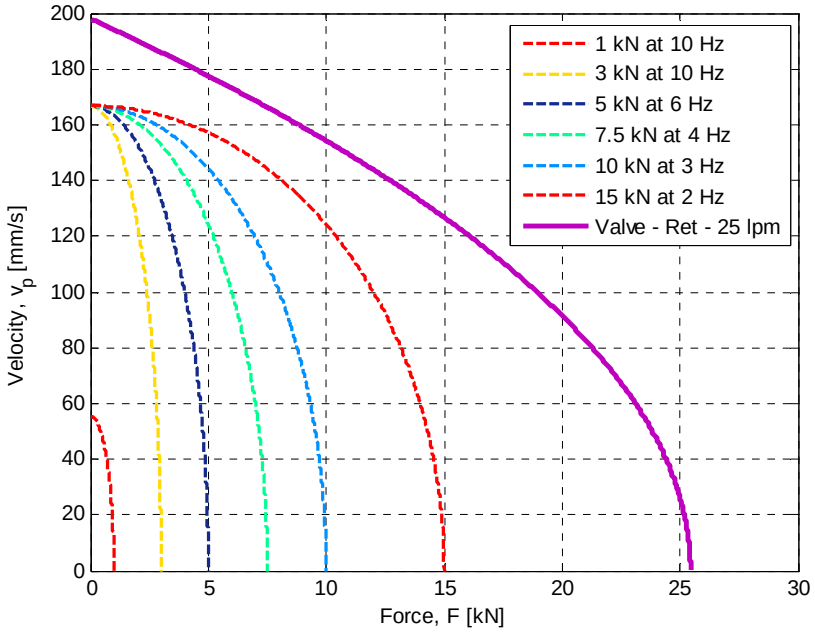

Figure 2-9 Load loci for the load simulator when $v_d = 0\ mm/s$

the figure. By using these figures, the loading limits of the hydraulic system are summarized in Table 2-2 and Table 2-3.

Table 2-2 Loading limits of the hydraulic system for $v_d = 100\ mm/s$

Magnitude [kN]	1	2.5	5	7.5
Frequency [Hz]	10	10	6	4

Table 2-3 Loading limits of the hydraulic system for $v_d = 0\ mm/s$

Magnitude [kN]	1	3	5	7.5	10	15
Frequency [Hz]	10	10	6	4	3	2

To conclude, if it is further required to get a more extended dynamic loading capability, the stiffness of the load system can be increased, but of course at the expense of an increased output impedance, $Z(s)$.

2.3.3 Hydraulic Power Pack

A hydraulic power pack is constructed to provide the valve controlled hydraulic system with the required flow rate at the selected constant supply pressure. The hydraulic layout of the power unit is given in Figure 2-10, and the elements of the power pack are listed below.

- Hydraulic pump and motor
- Pressure relief valve

- Check valve
- Shut-off valve
- High pressure filter
- Accumulator
- Reservoir
- Quick couplings for pressure and return lines (disconnected)

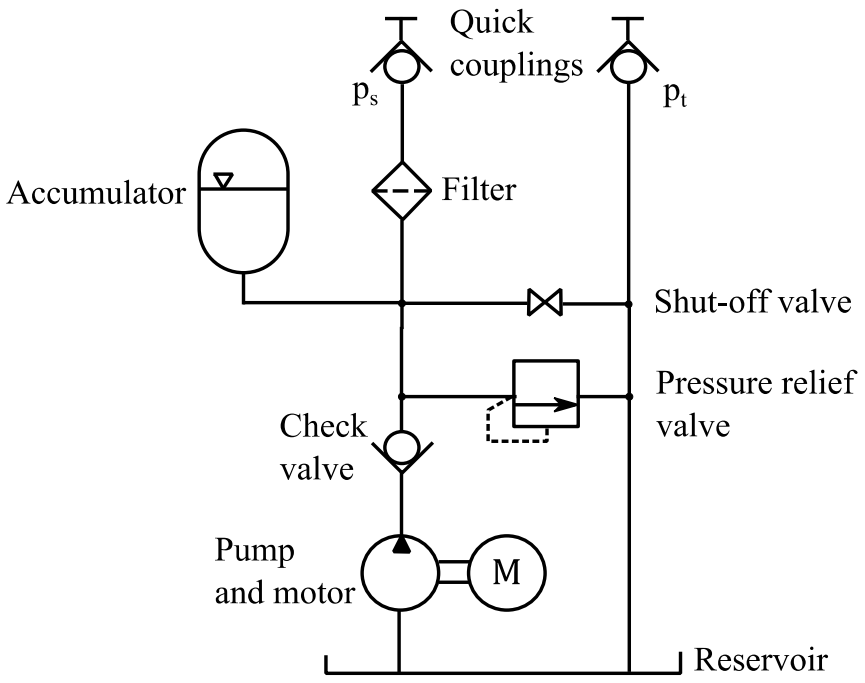

Figure 2-10 Hydraulic power pack layout – constant pressure operation

Pump and Motor

The required hydraulic power for the electro-hydraulic load simulator is provided by a constant displacement pump which is driven by a prime mover (an electric motor) as seen in Figure 2-10. A GAMAK cage induction motor with a power rating of

11 kW is utilized in this study, and its further specifications are given in Table 2-4. The size of the pump is determined by using the following equation:

$$Q_p = \eta D_p N \tag{2.8}$$

where η is the volumetric efficiency, D_p is the displacement of the pump per revolution, and N is the rotational speed of the pump, hence of the electric motor since they are coupled. From the catalog of Bucher Hydraulics, a constant displacement pump (QX31-032) with an effective displacement of 31.2 cm^3/rev is selected. Since its volumetric efficiency at 120 bar is about 0.93, the actual pump flow is determined as $Q_p = 43\ lpm$ by using (2.8). Hence, when the characteristic curve of the valve given in Figure 2-4 is considered, the selected pump-motor arrangement satisfies the required flow rate (42 lpm). In addition, the torque that should be provided by the electric motor to provide a supply pressure of 120 bar with this pump is determined as 60 Nm.

Table 2-4 Specifications of the electric motor

Type	$AGM2E$ 160 $M4$
Supply voltage	$3-phase, 400\ V, 50\ Hz$
Rated power	11 kW
Speed	1470 rpm
Current	21.0 A
Torque	71.5 Nm

Pressure Relief Valve

A Bucher Hydraulics DVPA-1-10-SM pressure relief valve is used to set the constant supply pressure at 120 bar [43]. It is a two-stage cartridge type pressure relief valve with a positive seat pilot stage, and a spool type main stage. The performance characteristic of the valve is given in Figure 2-11. As can be seen from its symbol, the flow direction is from its port A to port B, whereas in the reverse direction the flow is prevented. The crack pressure of the valve is adjusted through an adjusting screw on the valve. One complete turn of the adjusting screw increases the crack pressure of the valve about 38 bar.

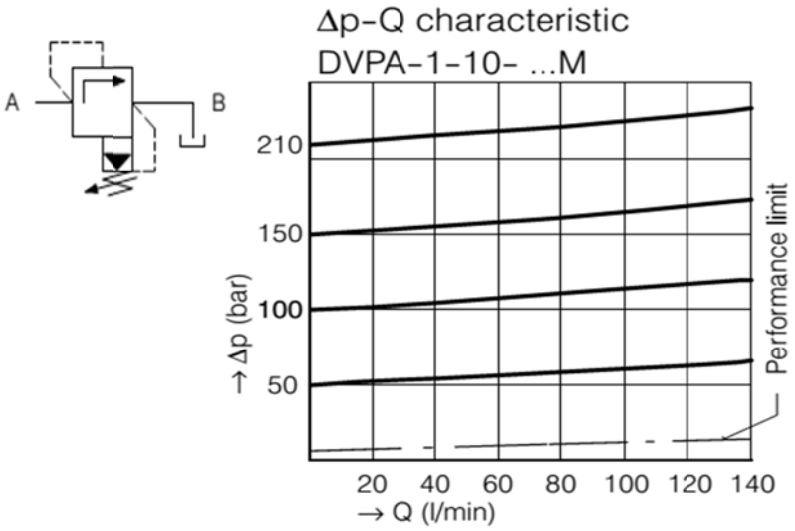

Figure 2-11 Performance characteristic of the pressure relief valve [43]

Accumulator

Accumulators are commonly preferred in constant pressure supply power packs to filter out the pressure oscillations generated at the pump and to provide the required flow at peak flow demands [40]. A SAIP bladder type accumulator with a volume of 1.5 liter and a maximum operating pressure of 350 bar (35 MPa) is used as it is

provided by the project sponsor. The pre-charge pressure of the accumulator p_0 is suggested in reference [44] to be calculated as follows:

$$p_0 = C_{acc} \cdot p_m \tag{2.9}$$

Here, p_m is the average operating pressure and C_{acc} is a constant between 0.6 and 0.75. Thus, the pre-charge pressure of the accumulator is set to $0.6 \cdot 120bar \approx 70\ bar$.

Transmission Line Elements

A number of flexible hoses, couplings, and fittings are used as the transmission line elements. For this purpose, FIREFLEX DIN EN 853 SAE100R2 AT 1/2" hydraulic hoses with a maximum operating pressure of $275\ bar$ are employed. Since the elasticity of the hoses affects the dynamics of the system, the control valve is assembled as close as possible to the hydraulic actuator in order to decrease the hose length. In addition, quick couplings are used to connect the power pack to the valve in order to decrease the setup-time and to prevent the hydraulic oil losses during disassembling and assembling the test bench.

Hydraulic Fluid

PO Hydro Oil HD 46 series hydraulic oil is used as the working medium in the valve controlled hydraulic system. Some typical physical specifications of the oil are given in Table 2-5. With its high viscosity index, it can be used in wide temperature ranges. It is also possible with this oil to obtain a cleanness level of NAS 7 (according to NAS 1638) by using a proper filtration, which is required for the operation of the proportional control valve.

Table 2-5 Physical specifications of the hydraulic oil

Manufacturer and type	Petrol Ofisi, Hydro Oil HD Series
ISO Viscosity Grade (VG)	46
Density, @ 15^oC	0.879 kg/m^3
Kinematic viscosity, @ 40^oC	46 mm^2/s
Viscosity Index	99

Hydraulic Reservoir

It is suggested as a rule of thumb that the volume of the hydraulic reservoir be 3 times the rated pump flow rate expressed as volume per minute [45]. That is, the time required to empty the reservoir should take 3-5 minutes in case of a failure of the major line [46]. Hence, the minimum required size of the hydraulic fluid reservoir is determined as about 120 $liters$.

Pressure Filter

The proper filtration of the hydraulic oil is extremely important to prevent component failures and the resulting failure costs [46]. An Eaton HP 61 10VG series pressure filter is utilized in order to maintain the required fluid cleanliness. This filter with stainless steel wire mesh has a filter-fineness of 10 μm. It is advised to place the filter at the last possible place before the critical component, which is the proportional flow control valve in this system [40]. Thus, the filter is placed just before the valve inlet as seen in Figure 2-10.

Before installing the proportional directional control valve, a flushing operation is performed by manually directing the fluid flow to both sides of the hydraulic actuator via a hand operated directional control valve during a day shift. The cleanliness of the system is monitored by the Parker Laser CM20 Contamination Monitor in order

to make sure that a level of NAS 6 is obtained before installing the proportional directional control valve to the system.

2.4 DAQ and Control System Hardware

In this section, the data acquisition and control system hardware utilized for the hydraulic load simulator is presented. It consists of a number of feedback and monitoring transducers, a real-time target machine as the real-time data acquisition system, and the control computer. The interactions of the transducers and the driver of the control valve with the real-time target machine and the hydraulic system can be seen in Figure 2-2.

2.4.1 Feedback and Monitoring Transducers

The electro-hydraulic load simulator is equipped with a number of feedback and monitoring transducers, namely, a force transducer, two pressure transducers, and a position transducer. In addition, an incremental encoder is used to measure the piston position of the hydraulic drive system under test. The details of these components are given in this section.

Force Transducer

The force applied by the load simulator onto the test actuator is determined via a force transducer which is given in Figure 2-12. It is a Burster Model 8524 tension and compression force transducer which is suitable for laboratory applications [47]. It is made of corrosion resistant steel and it is easily integrated with the test bench with the aid of a number of threaded and unthreaded fastening holes. The maximum static load that can be measured is 20 kN, and the natural frequency of the transducer is stated to be about 4 kHz. [47].

Figure 2-12 Burster tension and compression force transducer

The transducer operates on the principle that the force to be measured deforms a set of spring gauges, thus their electrical resistances change. In this model, a Wheatstone bridge arrangement of the gauges is utilized, which provides a voltage value directly proportional to the measured force. Thus, the voltage output of the transducer at maximum loading, U_a, is given by

$$U_a = c \cdot U_b \tag{2.10}$$

where U_b is the excitation voltage and c is the sensitivity of the transducer.

A test and calibration certificate is provided by the manufacturer and the sensitivity of the transducer is given as $1.5004\ mV/V$. Since an excitation voltage of $U_b = 5\ V$ is recommended, the output of the transducer is in the range of $7.5\ mV$. This highly small amplitude signal is amplified with a signal amplifier whose bandwidth is $1\ kHz$. The calibration and gain setting of the amplifier is explained in Appendix B.2. The transducer outputs a positive signal while it is at compression.

Pressure Transducers

Both chamber pressures of the hydraulic actuator of the load simulator are measured by separate pressure transducers. Two Trafag 8472 pressure transducers (Figure 2-13) are used in this study [48]. They are supplied by a voltage of $24\ V\ DC$. The measuring range of the both transducers is $0-250\ bar$. They provide a voltage signal output in the range of $0-10\ V\ DC$. All pressure transducers are calibrated by using a dead weight pressure tester and the results are used to implement a look-up table for better results. The calibration of transducers via the deadweight pressure tester is explained in Appendix B.1.

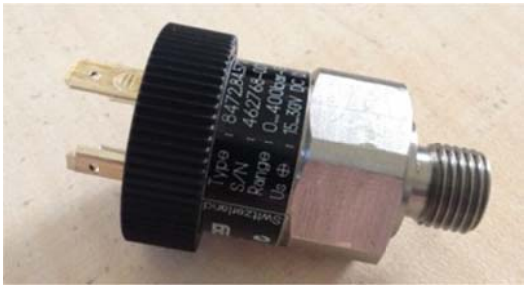

Figure 2-13 Trafag 8472 pressure transducer

Position Transducers

In this study, the position of the piston-rod relative to the cylinder is measured by a Novotechnik linear contactless magnetostrictive position transducer [49]. It consists of a rod-shaped measuring probe and a ring-shaped position marker as seen in Figure 2-14. The transducer is fastened coaxially to the hydraulic cylinder and its long rod-shaped measuring probe extends into the gun-drilled piston-rod. On the other hand, the ring-shaped position marker is fixed to the piston of the hydraulic actuator. The stroke of the transducer is $300\ mm$. In addition, it is an absolute position transducer and provides a voltage output in the range of $0-10\ V\ DC$. It requires a supply voltage of $24\ V\ DC$ and the working pressure is to be limited to a chamber pressure of $350\ bar$.

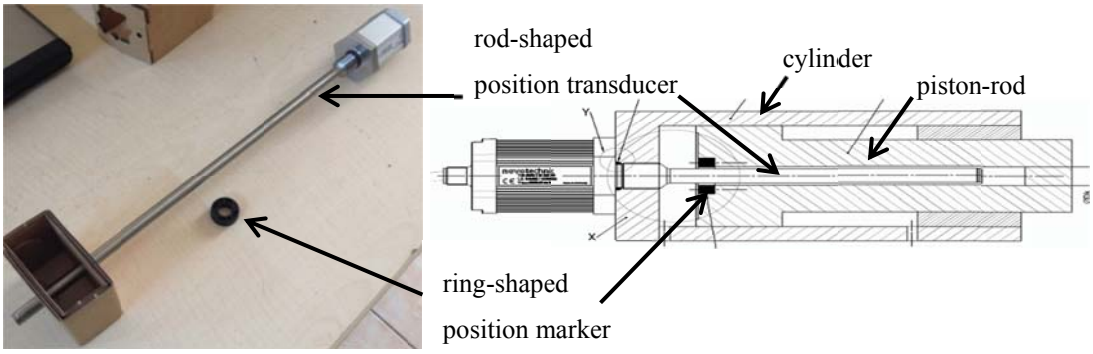

Figure 2-14 Novotechnik position transducer [49]

In addition, the test bench is equipped with an incremental encoder to measure the position of the actuator under test. Its connection to the actuator can be as seen in Figure 2-20. It is an Atek MLS-4 series incremental encoder with $270\,mm$ stroke and $5\mu m$ resolution at 4X decoding. The encoder provides a TTL output with A and B channels as well as an index channel. It requires a supply voltage of $5\ V\ DC$. Since the motion of the test actuator is considered as the disturbance input to the electro-hydraulic load simulator, the output of this incremental encoder is utilized in the feedforward controller of the load simulator designed for the purpose of disturbance rejection.

2.4.2 Real-Time DAQ and Control Computer

A Speedgoat modular real-time target machine (SN 1414) with various analog and digital IO modules is utilized as the DAQ system and control computer, which is shown in Figure 2-15. The computer has an Intel Core 2 Duo 2.26 GHz processor and a memory of 2048 MB DDR3 RAM. Moreover, the target machine is equipped with the following I/O modules:

- Analog input module (I/O105)
- Analog output module (I/O111)

- TTL/SSI encoder module (I/O401)
- Digital input and output module (I/O203)

Figure 2-15 Speedgoat modular real-time target machine

The analog input module I/O105 includes 32 differential analog input channels of 16-bit resolution. This module is used to acquire the voltage outputs of the pressure, position, and force transducers. The analog output module I/O111 includes 16 analog output channels of 16-bit resolution. This module is utilized to drive the proportional control valve. The encoder module I/O401 includes 6 counters of 32-bit resolution. This module is used to acquire the output of the incremental encoder. Connections of all these transducers to the corresponding I/O modules can be seen in Appendix A.1.

The real-time target machine is compatible with MathWorks® xPC Target™ software. Hence, the real-time control of the system is performed by implementing the designed controller in MATLAB®/Simulink®. A standard personal computer with a MATLAB® R2011a (win32) software installed is utilized as the host PC. The Speedgoat's tools and drivers for xPC target are installed on the top of the existing MATLAB® software. In addition, it is required that the MathWorks® products,

namely, Simulink®, Real-Time Workshop®, and xPC Target™, already be installed on the host PC. A fixed step Runge-Kutta 4th order (ode4) solver is selected with a sampling frequency of $1000\,Hz$ for integration of system differential equations during simulations. The designed controller in MATLAB®/Simulink® environment is compiled in the host PC and downloaded to the real-time target machine.

2.5 Mechanical Construction of the Test Bench

A test bench is designed and constructed to accommodate the actuators of the load simulator and the hydraulic system under test. The solid model of the test bench can be seen in Figure 2-16, which is obtained by modeling the components of the test bench in SolidWorks 2010. As seen in the figure, a closed frame structure is preferred in order to prevent the created forces from being transferred to its environment. Therefore, the resulting structure can be mounted on any platform. Furthermore, it is compact and easily transportable. Some important dimensions of the test bench can be seen in Appendix C.

The components of the test bench are labeled in Figure 2-17. Hydraulic actuators are supported by two separate mounting brackets. Each actuator is clamped to its mounting bracket with six threaded bolts. On the other hand, the mounting brackets are connected to each other to form a closed structure through six end threaded connecting rods by using nuts. In order to provide these connections, the mounting brackets are machined to obtain the required holes. The technical drawings of the brackets can be seen in Appendix C. Furthermore, the proper alignment of the actuators is critical since the lateral forces induced onto the force transducer increase with increasing amount of misalignment, which may damage the transducer. Hence, the brackets are machined together to ensure the concentricity of the rods of two actuators.

The length of the connecting rods, that is the distance between the actuators of the load simulator and the system under test, is determined such that the whole stroke of

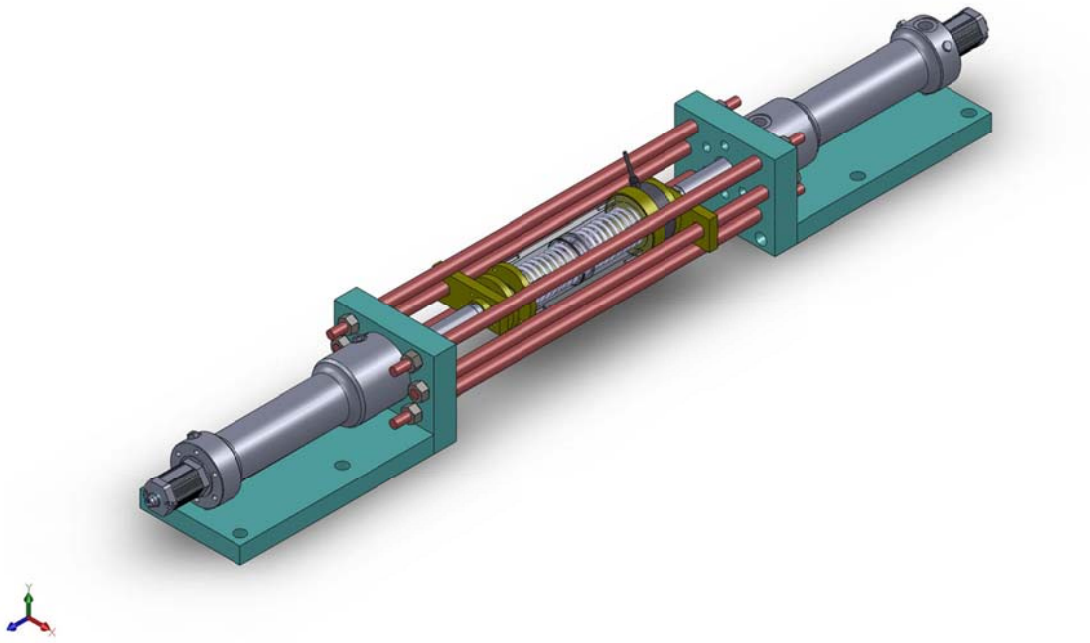

Figure 2-16 Isometric view of the load simulator test bench

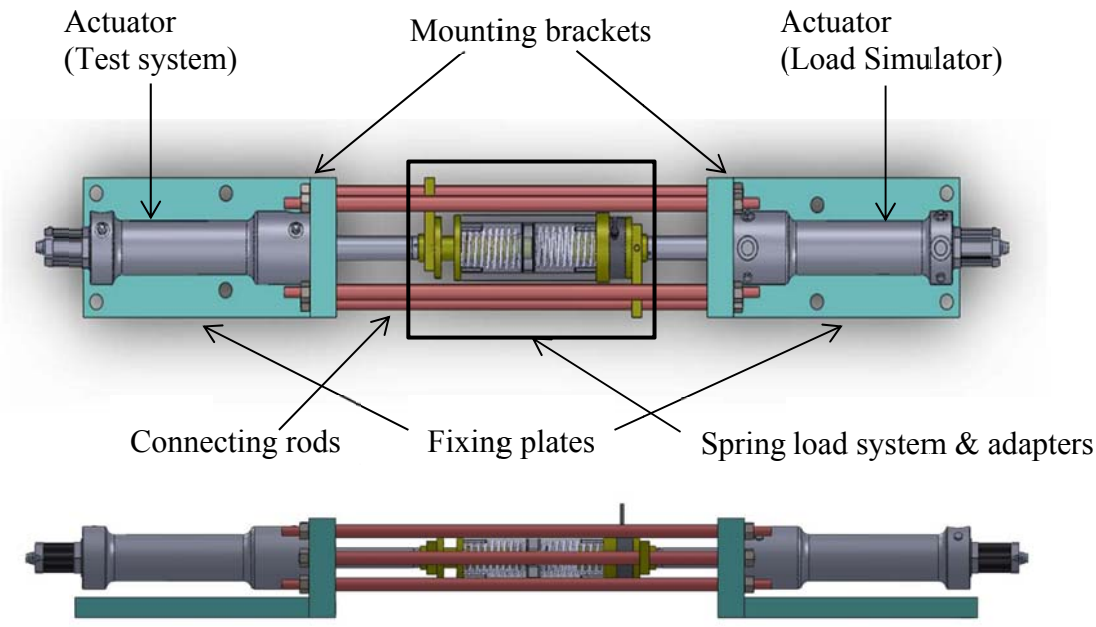

Figure 2-17 Top and side views of the test bench and its components

the actuators can be utilized during testing. Therefore, when the piston of one of the actuators is at its maximum stroke, the other is at its minimum stroke. Note that the unloaded length of the load system is also taken into account.

So as to fix the test bench to a platform, two thick plates are fastened to the mounting brackets as seen in Figure 2-17. The plates are then bolted to a base platform through the mounting holes of the plates. Thanks to the closed mechanical structure of the test bench, no load is induced by the loading system onto the fixing plates same as the base platform.

The actuators of the load simulator and the system under test are connected to each other through the load system whose isometric view is given in Figure 2-18. A honed cylinder is utilized as the spring housing and two housing heads are used to pre-compress the die springs in the housing. In addition, a piston-rod arrangement is used to deflect the springs within the spring housing. The piston of the loading rod is grooved to place a low friction seal.

Note that it is required to have the die springs connected in parallel to each other. Hence, as seen in Figure 2-19, the piston of the piston-rod arrangement deflects the

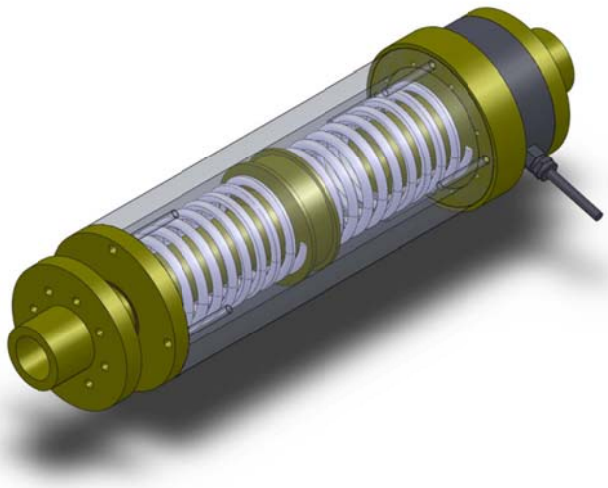

Figure 2-18 Isometric view of the spring load system

springs the same amount and thus they are in parallel connection. In addition, the length of the housing cylinder is determined such that during testing none of the springs can reach to their free lengths if the applied forces are within the operating limits. The free length of the springs is given in Appendix D as 127 mm and the main dimensions of the load system are given in Appendix C where the length of the housing is 210 mm. Since the piston deflecting the springs inside the load system has a length of 20 mm, each spring is pre-compressed to a value of 18 kN, which is greater than the operating limit of the system. Thus, the pre-deflection of the springs prevents the nonlinearity in the operation.

The force transducer is connected to one of the housing head with six threaded bolts. The other side of the force transducer is connected to the actuator of the system under test with the aid of a thread adapter. Similarly, another thread adapter is utilized to connect the piston-rod arrangement of the load system to the actuator of the load simulator.

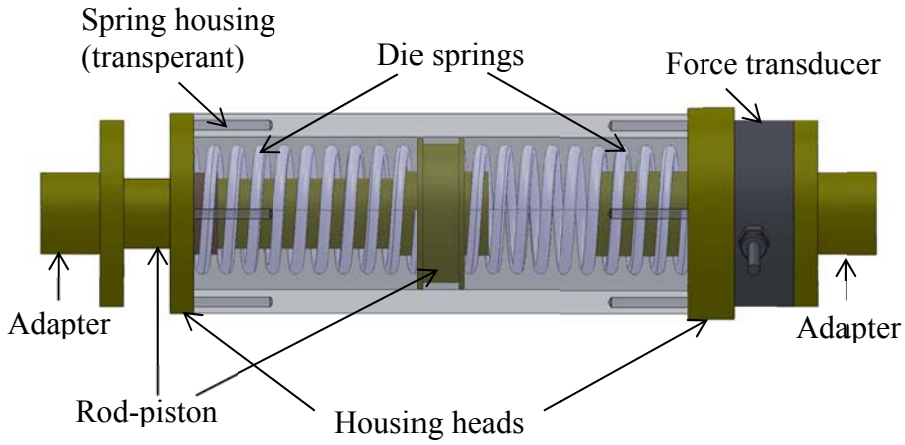

Figure 2-19 Side view of the spring load system and its components

2.6 The Overall View of the Test Bench

A photograph of the electro-hydraulic load simulator test bench is given in Figure 2-20. The hydraulic actuator and the proportional control valve of the hydraulic load simulator are seen on the right as well as its connection to its hydraulic power pack. On the other hand, the actuator of the system under test is located on the left of the test bench with its hydraulic equipment. The actuators are connected to each other through the spring load system. The main components of the load simulator are also labeled in Figure 2-21. A photograph of the hydraulic power pack is provided in Figure 2-22, on which its components are labeled.

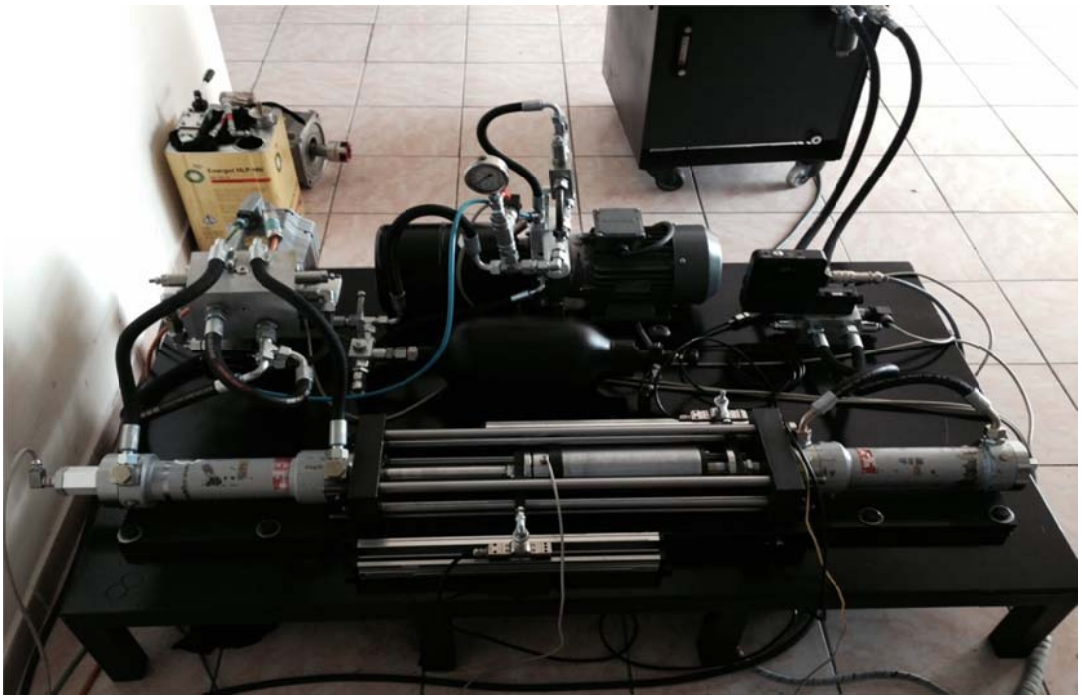

Figure 2-20 A photograph of the electro-hydraulic load simulator test bench

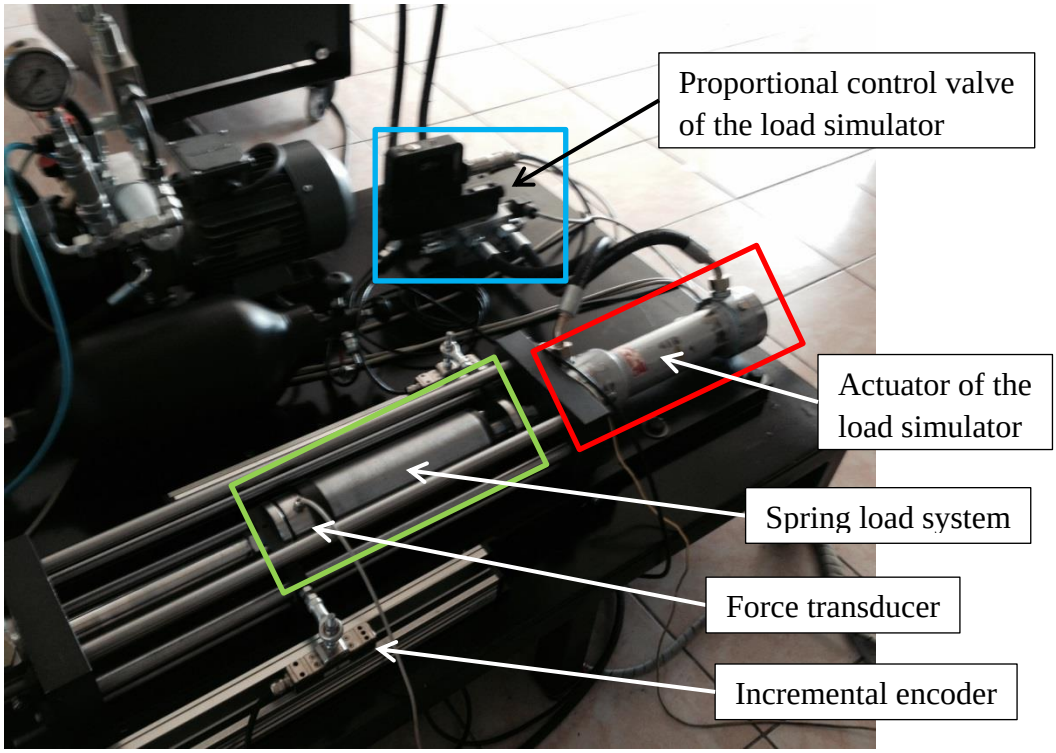

Figure 2-21 Components of the hydraulic load simulator

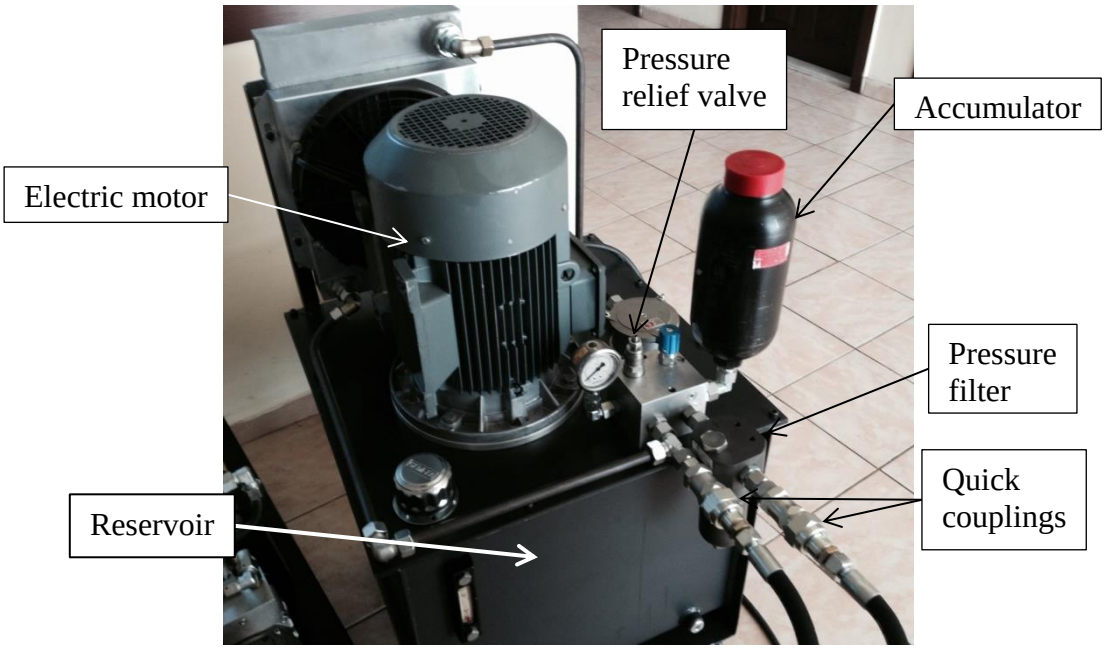

Figure 2-22 A photograph of the power pack and its components

CHAPTER 3

MATHEMATICAL MODELING OF THE SYSTEM

In this chapter, a mathematical model of the electro-hydraulic load simulator is developed with the purpose of control system design and analysis and a numerical simulation model is obtained by using MATLAB®/Simulink®. In Section 3.1, the physical model of the hydraulic system is given and the mathematical model of the each component is developed by using the physical laws under the stated assumptions. The simulation model of each component is also constructed and presented. In Section 3.2, the nominal model parameters are obtained and the simulation model is validated by comparing the simulation results with the open-loop test results.

3.1 Mathematical Model

The physical model of the valve controlled electro-hydraulic load simulator is given in Figure 3-1 for mathematical modeling. The hydraulic system consists of a differential hydraulic actuator and a proportional control valve with an input signal of u. The areas of the actuator for piston and rod side are represented by A_A and A_B, respectively. The mass of the piston and other parts attached to it are lumped to the mass m_p, whose position is denoted by x_p. The spring arrangement connecting the load actuator to the test actuator is represented by a spring with stiffness k_s where the force transducer is assumed to be rigid. In addition, a positive direction for the disturbance motion is assumed and is denoted by x_d in the figure.

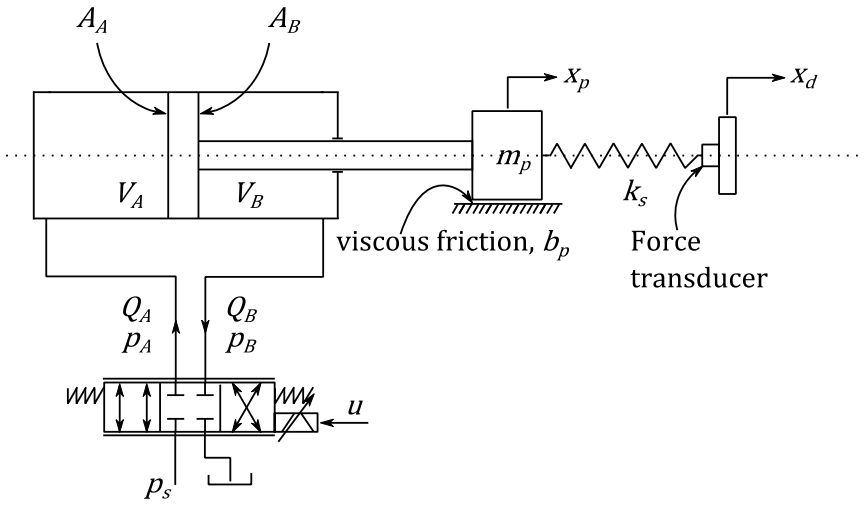

Figure 3-1 Physical model of the electro-hydraulic load simulator

In the following sub-sections, the simplifying assumptions are explained and the mathematical models of the valve, actuator, and the load are developed by using physical laws. Furthermore, the MATLAB®/Simulink® models for each sub-system are constructed and presented.

3.1.1 Valve Model

A four-way, zero-lapped proportional control valve is used in order to control the flow through the actuator of the load simulator. The valve is modeled as shown in Figure 3-2. The input voltage to the valve driver u results in a proportional spool

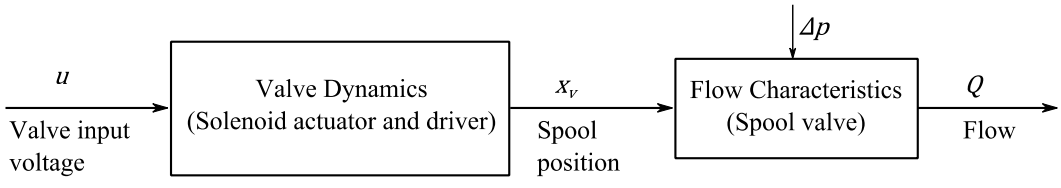

Figure 3-2 Valve model

position x_v, which is controlled by the position controller of the spool in the valve driver. An LVDT on the valve feeds back the spool position to the controller. For this study, a first order transfer function between the input voltage $U(s)$ and the spool position $X_v(s)$ can be used to describe the valve dynamics as follows:

$$G_a(s) = \frac{X_v(s)}{U(s)} = \frac{K_a}{T_a s + 1} \tag{3.1}$$

where K_a is the steady state gain and T_a is the time constant of the valve actuator.

The time constant of the valve actuator T_a can be approximated from the frequency response plots of the valve given in Figure 3-3, where the amplitude ratio corresponds to the input voltage and the voltage output of the LVDT on the valve. The bandwidth of the valve, that is the frequency range in which the magnitude curve is greater than -3 dB, is about 80 Hz.

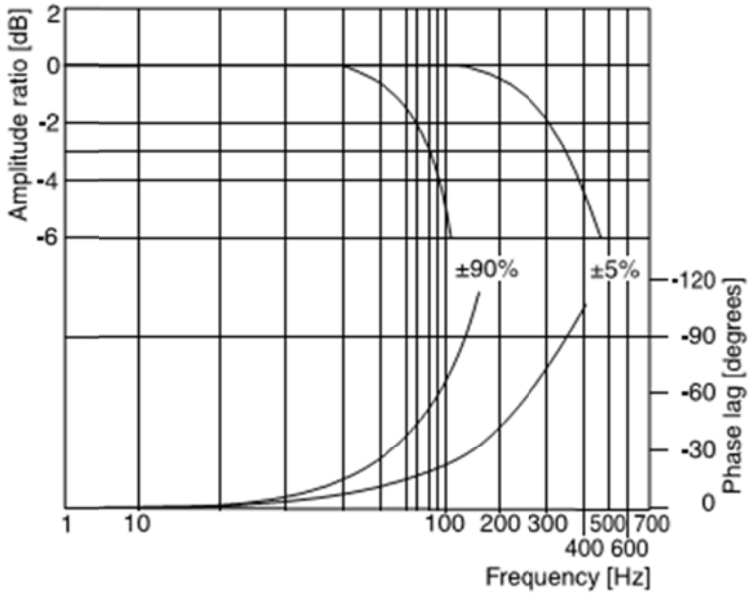

Figure 3-3 Frequency response (Bode) plots of the control valve [42]

The resulting opening of the valve leads to flows through the orifices of the valve. To determine the flow through each orifice, the following flow equation is utilized.

$$Q = C_d w x_v \sqrt{\frac{2}{\rho}\Delta p} \tag{3.2}$$

Here, C_d and w are the discharge coefficient and peripheral width of the orifice, respectively, Δp is the pressure differential across the orifice and ρ is the density of the hydraulic fluid.

A schematic view of a typical symmetrical four-land-four-way spool valve is given in Figure 3-4. Ports labeled as A and B are connected to the piston and rod side chambers of the hydraulic actuator, respectively. Also, assumed directions of the flows through these ports Q_A and Q_B are indicated in the figure. Remaining ports are for the supply and return lines as shown. Supply and return pressures are represented by p_s and p_t, respectively. In this study, oscillations in the supply pressure are neglected and the supply pressure is assumed to be constant since an accumulator is utilized on the pressure line to reduce those oscillations. On the other hand, the return pressure is assumed to be zero, i.e., $p_t = 0$, since it is considerably smaller than the other system pressures [40].

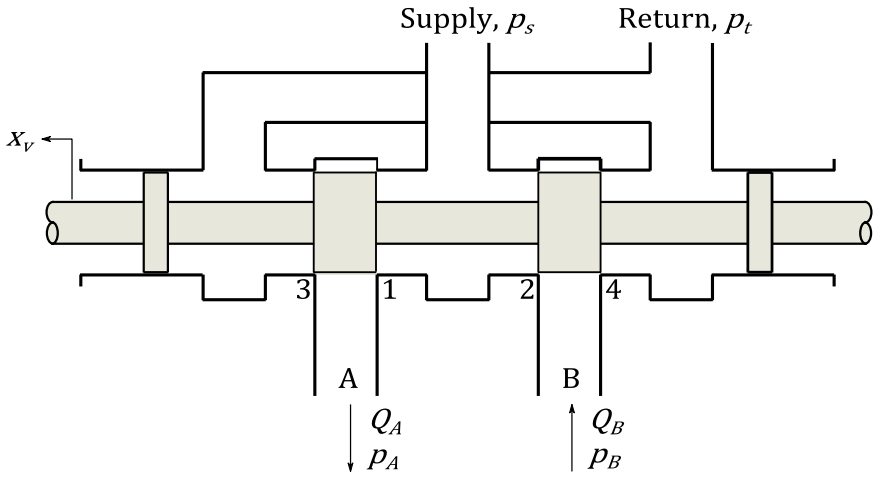

Figure 3-4 Schematic of a four-land-four-way spool valve

Four orifices on the valve are numbered in Figure 3-4. In addition, the assumed positive direction of the spool position is shown in the figure. For an exactly zero-lapped valve with perfect radial clearances, at null position of the spool, no flow to the load is allowed whereas only two of the orifices of the valve permit the fluid flow depending on the sign of spool stroke.

The configuration of the valve for the positive displacement of the spool is given in Figure 3-5. Here, only the orifices 1 and 4 allow the fluid flow to provide the extension of the hydraulic actuator.

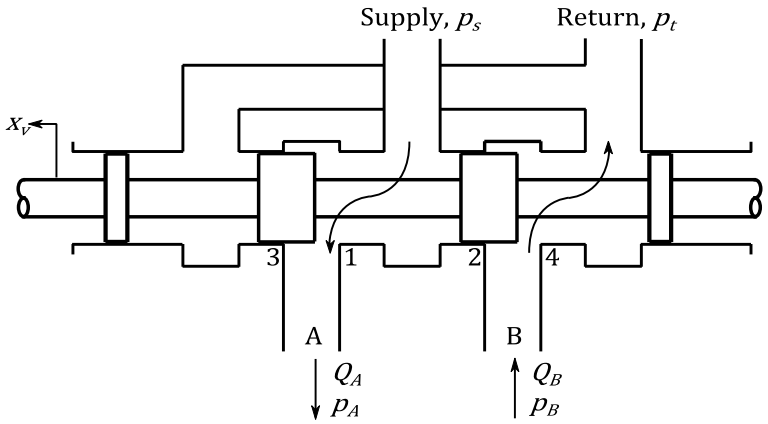

Figure 3-5 Configuration of the valve for positive spool position

Following flow equations can be written for $x_v \geq 0$:

$$Q_A = C_d w x_v \sqrt{\frac{2}{\rho}(p_s - p_A)} \tag{3.3}$$

$$Q_B = C_d w x_v \sqrt{\frac{2}{\rho} p_B} \tag{3.4}$$

The configuration of the valve for the negative displacement of the spool is given in Figure 3-6. In this configuration, only the orifices 2 and 3 allow the fluid flow to provide the retraction of the hydraulic actuator.

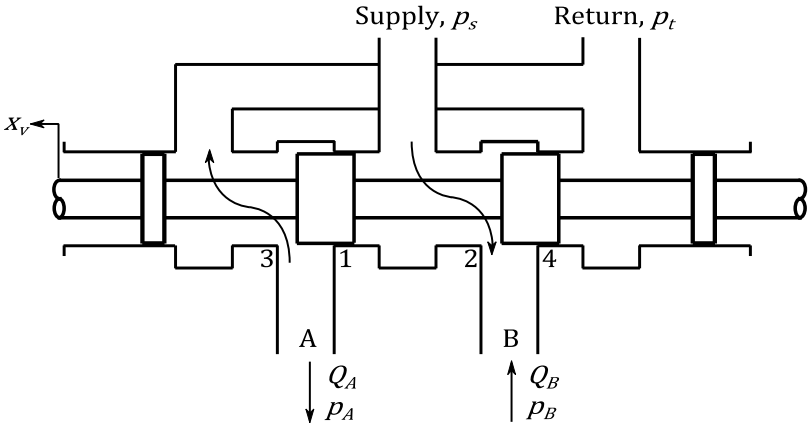

Figure 3-6 Configuration of the valve for negative spool position

Following flow equations for can be written for $x_v < 0$:

$$Q_A = C_d w x_v \sqrt{\frac{2}{\rho} p_A} \tag{3.5}$$

$$Q_B = C_d w x_v \sqrt{\frac{2}{\rho} (p_s - p_B)} \tag{3.6}$$

In general, the model parameters of the valve are difficult to determine, or measure, and not available in valve catalogs. Instead, they are combined in a parameter K_v named as *steady state flow gain*, which is given by

$$K_v = K_a C_d w \sqrt{\frac{2}{\rho}} \tag{3.7}$$

The steady state flow gain of the valve is extracted from the valve catalog by using the nominal (rated) flow of the valve at maximum input signal. The nominal flow of the valve is provided by the manufacturer as $25\ lpm$ under a pressure drop of $35\ bar$ at each orifice. Moreover, the flow curve of the valve with respect to the input signal is given in Figure 3-7. It is seen that, at constant pressure drop, the flow gain is independent of the input signal and it is fairly constant.

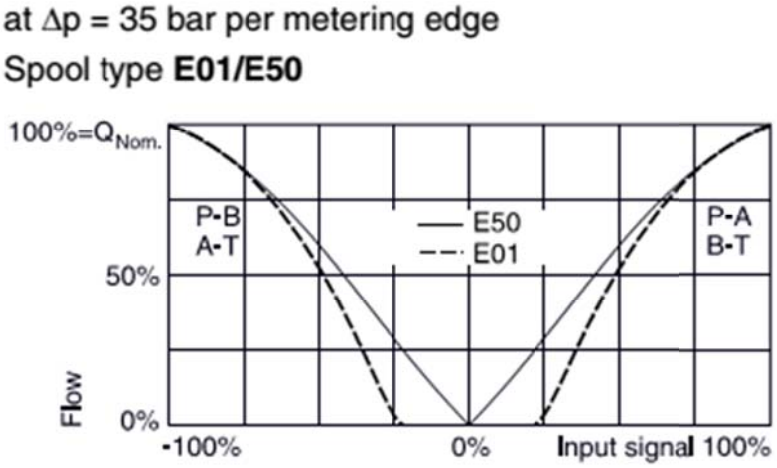

Figure 3-7 Percentage flow rate versus percentage input signal for the control valve – solid line for spool type E50 [42]

Introducing the steady state flow gain K_v into Equations from (3.3) to (3.6), the flow equations for steady state are obtained as follows:

- For positive valve opening $x_v \geq 0$,

$$Q_A = K_v x_v \sqrt{p_s - p_A} \tag{3.8}$$

$$Q_B = K_v x_v \sqrt{p_B} \tag{3.9}$$

- For negative input signal $x_v < 0$,

$$Q_A = K_v x_v \sqrt{p_A} \tag{3.10}$$

$$Q_B = K_v x_v \sqrt{p_s - p_B} \tag{3.11}$$

In addition, the steady state gain of the transfer function between the input voltage $U(s)$ and the spool position $X_v(s)$ can be assumed as unity for convenience to simplify to

$$G_a(s) = \frac{X_v(s)}{U(s)} = \frac{1}{T_a s + 1} \tag{3.12}$$

The MATLAB®/Simulink® model of the proportional control valve is obtained by using the Equations from (3.8) to (3.13) as shown in Figure 3-8. The valve model accepts the voltage signal u and the chamber pressures of the hydraulic actuator p_A and p_B as inputs. The output of the model is the flow rates through its ports A and B, which are Q_A and Q_B, respectively. The saturations of the valve input signal at $-u^{max}$ and u^{max} are also included in the model with a saturation block.

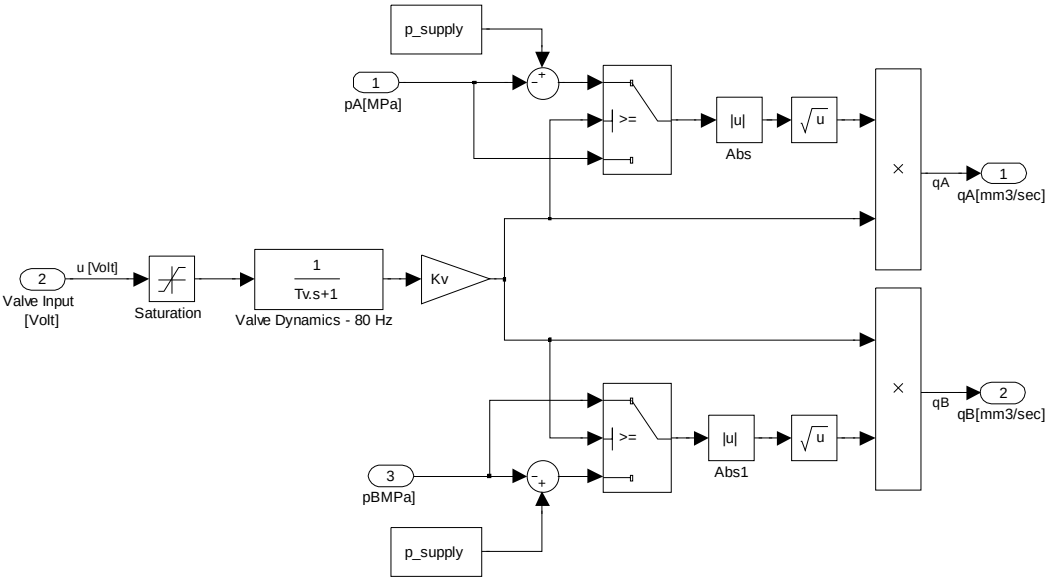

Figure 3-8 MATLAB®/Simulink® model of the proportional control valve

3.1.2 Hydraulic Actuator Model

In this sub-section, the mathematical model of the hydraulic actuator shown in Figure 3-1 is obtained. It is a single rod actuator, also called as an $A + \alpha A$ *configuration* [50]. The positive direction for the actuator motion, x_p, is compatible with the input signal to the valve, u. That is, a positive input signal to the control valve causes a positive velocity of the hydraulic actuator and vice versa. In addition, it is assumed that the actuator is at its mid-stroke when $x_d = 0$.

The effect of compressibility of the hydraulic fluid is taken into consideration in the model. The bulk modulus of the hydraulic fluid is represented by β and it is assumed to be constant. However, the compliance effect of the actuator structure is neglected. Also, the lines are assumed to be rigid and volume of the fluid between the valve and actuator is small since valve is very close to the actuator. In addition, the external and cross-port leakages of the hydraulic piston are not considered in the model. Hence, the flow continuity equations for both chambers of the hydraulic actuator are written as follows:

$$Q_A = A_A \dot{x}_p + \frac{V_A}{\beta}\frac{dp_A}{dt} \tag{3.13}$$

$$Q_B = A_B \dot{x}_p - \frac{V_B}{\beta}\frac{dp_B}{dt} \tag{3.14}$$

The force output of the hydraulic actuator, F_L, is obtained by

$$F_L = A_A p_A - A_B p_B \tag{3.15}$$

The piston and rod side volumes of the hydraulic actuator depend on the position of the hydraulic actuator. Hence, the piston side volume of the actuator, V_A, is

$$V_A = V_{A_0} + A_A x_p \tag{3.16}$$

whereas the rod side volume, V_B, is

$$V_B = V_{B_0} - A_B x_p \tag{3.17}$$

Here, V_{A_0} and V_{B_0} are the initial, or mid-stroke ($x_p = 0$), piston and rod side volumes of the hydraulic actuator, respectively.

The MATLAB®/Simulink® model of the hydraulic actuator, implementing Equations from (3.13) to (3.17), is given in Figure 3-9. The model accepts the flow rates Q_A and Q_B, the position x and velocity $\dot{x}$ of the actuator as inputs, and outputs the hydraulic load force F_L together with the chamber pressures p_A and p_B separately.

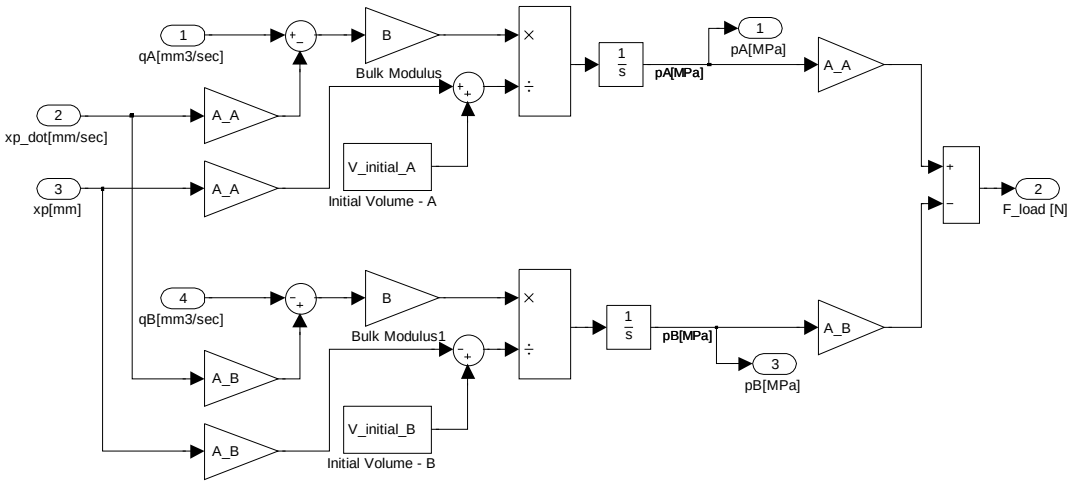

Figure 3-9 MATLAB®/Simulink® model of the hydraulic actuator

3.1.3 Load Model

Figure 3-1 shows the hydraulic actuator of the load simulator and its connection to the test actuator with a compliant spring with stiffness k_s. The mass of the piston is represented by the lumped mass m_p. A viscous friction is assumed between the cylinder and the piston and its coefficient is denoted by b_p. A rigid connection of the

test actuator to the force transducer is assumed, and the position of the test actuator is denoted by x_d. The application of the Newton's 2nd law of motion to the system yields to

$$m_p\ddot{x}_p + b_p\dot{x}_p + k_s x_p = A_A p_A - A_B p_B + k_s x_d \tag{3.18}$$

The ultimate control variable in the electro-hydraulic load simulator is the force exerted to the system under test F, and it is given by

$$F = k_s(x_p - x_d) \tag{3.19}$$

The MATLAB®/Simulink® model of the load is shown in Figure 3-10. The model is constructed by using Equations from (3.13) to (3.17). The inputs to this sub-model are the force generated by the hydraulic actuator F_L and the velocity of the actuator under test as the disturbance input $\dot{x}_d$. The output of the model are the position and velocity of the actuator of the load simulator $x_p$and $\dot{x}_p$, and the force exerted to the actuator under test F, which is the control variable. Furthermore, the non-linearity due to the limited stroke of the hydraulic actuator between $-x_p^{max}$ and x_p^{max} is included into the model.

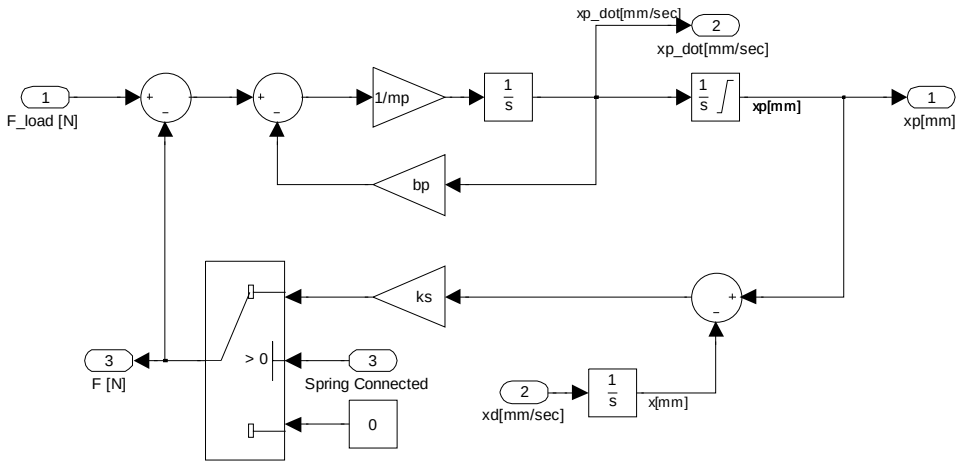

Figure 3-10 MATLAB®/Simulink® model of the load

3.2 Model Validation

In the previous section, the mathematical models of the proportional control valve, the hydraulic actuator, and the load are obtained and their simulation models are constructed by using MATLAB®/Simulink®. The inputs and outputs of each sub-model are clearly identified. In this section, these sub-models are combined to construct the whole system simulation model as seen in Figure 3-11. The model is validated with experimental test results in order to prove its reliability for the control system design and analysis.

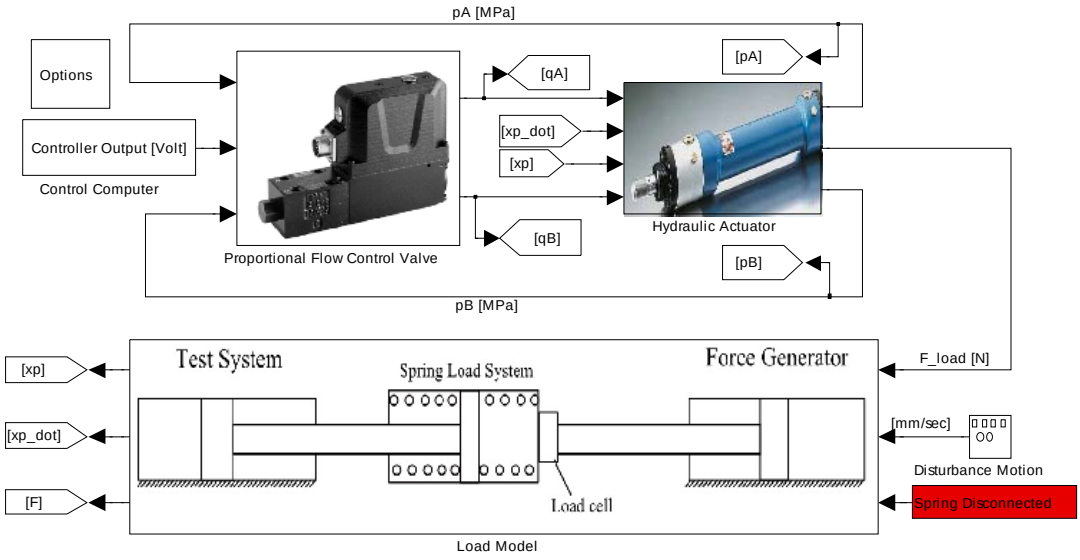

Figure 3-11 MATLAB®/Simulink® model of the whole system

Most model parameters are available in the manufacturers' catalogues and the technical drawings of the products. However, the friction characteristic of the hydraulic actuator, which is highly important in the pressure response of the hydraulic system, is not available and it has to be determined experimentally.

In order to determine the friction characteristic of the hydraulic actuator, a sinusoidal control input with a magnitude of $5\,Volts$ and frequency $1\,Hz$ is applied to the proportional control valve without saturating the hydraulic actuator. The test is

performed when only mounting parts are attached to the hydraulic cylinder and the supply pressure is adjusted to an operating pressure of $p_s = 120\ bar$. The actuator position x_p and the chamber pressures p_A and p_B are measured by a linear position encoder and pressure transducers at each chambers, respectively. Furthermore, the acceleration of the actuator is estimated by using a kinematic Kalman filter. Using Newton's second law of motion, the friction force is determined as follows [51]:

$$F_f = A_A p_A - A_B p_B - F - m_p \ddot{x}_p \tag{3.20}$$

The friction force is then plotted as a function of piston velocity as shown in Figure 3-12. There are 4 cycles available in the figure. As clearly seen in the figure, a Stribeck friction curve, which is commonly encountered in literature [51], can be utilized to represent the friction characteristic of the hydraulic actuator. It consists of static friction, Coulomb friction and viscous friction proportional to the actuator velocity.

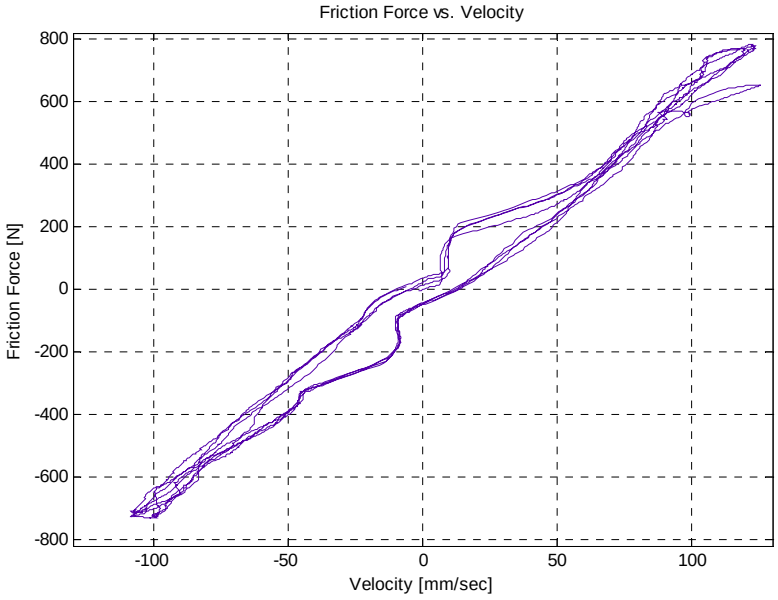

Figure 3-12 Measured friction force versus velocity of the hydraulic actuator – Supply pressure $p_s = 120\ bar$

Investigating the friction characteristic of the hydraulic actuator, it is seen that the effects of non-linear components of the friction can be neglected and only a viscous friction can be assumed. In addition, this assumption is reasonable since a linear analysis will be performed in the design and analysis of the controller.

In order to linearly represent the friction characteristic of the hydraulic actuator given in Figure 3-12 as a pure viscous friction, MATLAB®'s Curve Fitting Toolbox is utilized. The graphical interface of the toolbox is utilized to import the data and fit a linear polynomial of the form

$$F_f(\dot{x}_p) = p_1 \dot{x}_p \tag{3.21}$$

The coefficient of the polynomial is found as $p_1 = 6.5$. The goodness of the fit is given with a root mean square error of $47.4\ N$.

In Figure 3-13, it is seen that the viscous friction assumption represents the friction characteristic fairly well, and its static and Coulomb friction components are neglected.

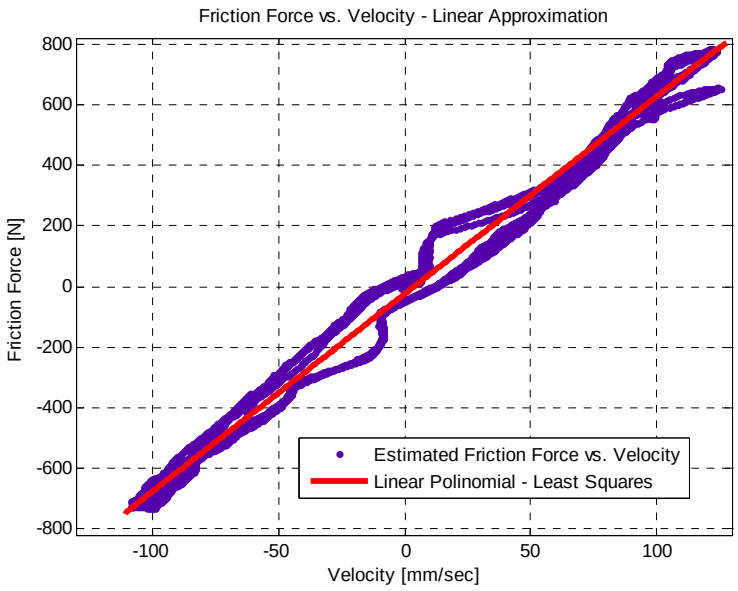

Figure 3-13 Viscous friction force approximation of the measured friction force

Most model parameters are obtained from the manufacturers' catalogs whereas only the friction characteristic of the hydraulic actuator is determined experimentally. In addition, the bulk modulus of the fluid is approximated from literature [41]. The nominal values for the model parameters are listed in Table 3-1.

Table 3-1 Nominal values of the model parameters

Parameter	**Symbol**	**Unit**	**Value**
Piston side area	A_A	mm^2	2827.4
Rod side area	A_B	mm^2	2120.6
Maximum actuator stroke	x_p^{max}	mm	200
Flow gain of the control valve	K_v	$\frac{mm^3}{sV\sqrt{MPa}}$	22270
Valve actuator time constant	T_a	s	0.002
Initial volume of the piston side chamber	V_{A_0}	mm^3	325200
Initial volume of the rod side chamber	V_{B_0}	mm^3	243900
Stiffness of the compliant spring	k_s	N/mm	1130
Viscous damping coefficient	b_p	$N \cdot s/mm$	6.5
Mass of the piston	m_p	kg	3
Bulk modulus of the hydraulic fluid	β	MPa	1300
Supply pressure	p_s	MPa	12
Tank pressure	p_t	MPa	0

The validity of the model with parameters given in Table 3-1 is evaluated by performing some open-loop tests, and comparing the results of these experimental tests with the simulation results. This approach is generally considered as the *most obvious and pragmatic* way to determine whether a model is *good enough* [52].

In the open-loop test, a sinusoidal input signal is applied to the valve driver. During the test, the valve spool position, the hydraulic actuator position, and pressures of both chambers are measured by means of corresponding transducers. The sinusoidal input signal to the valve has a magnitude $3\,Volt$ and frequency $1\,Hz$ as shown in Figure 3-14. The spool position is obtained via the LVDT of the valve. The measurement and simulation results are also given in this figure. In Figure 3-14, the residual error between the measured and simulated spool position responses is also given which is within an error band of $\pm 0.14\,Volt$. It is seen that the model is reasonable within $0.033\,Volt\ rms$.

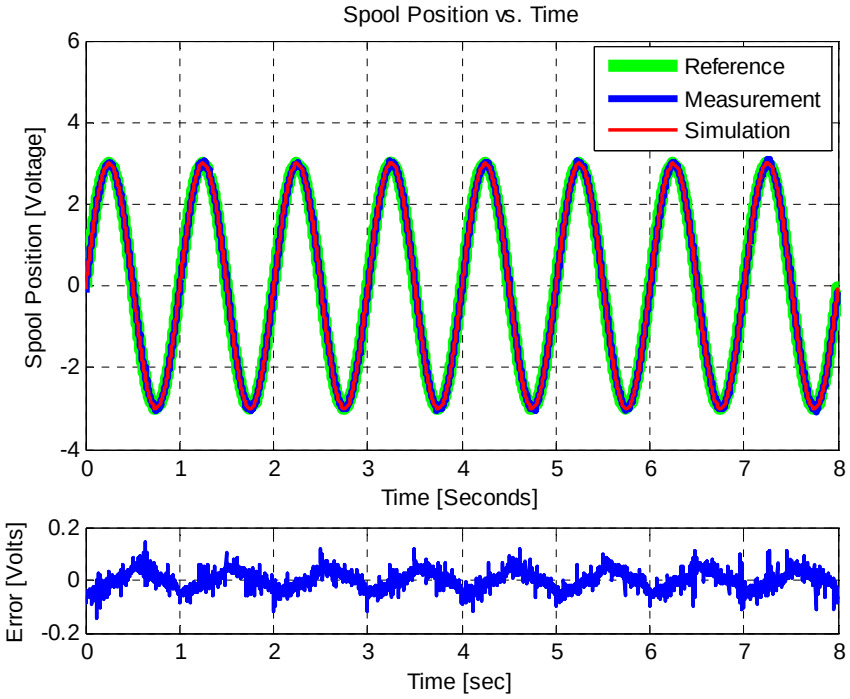

Figure 3-14 Measured and simulated spool position responses of the open-loop system to a reference sinusoidal input and residual error

In Figure 3-15, measured and simulated position responses of the hydraulic actuator are compared. Since the hydraulic actuator is a differential actuator, its extension velocity is greater than its retraction velocity, as expected. Therefore, a drift in extension direction of the actuator in each cycle of the sinusoidal control input is observed. In Figure 3-15, the residual error between the measured and simulated position responses is also shown. The residual error remains in an error band between -1 and $1\ mm$ with a root mean squared value of $0.33\ mm$.

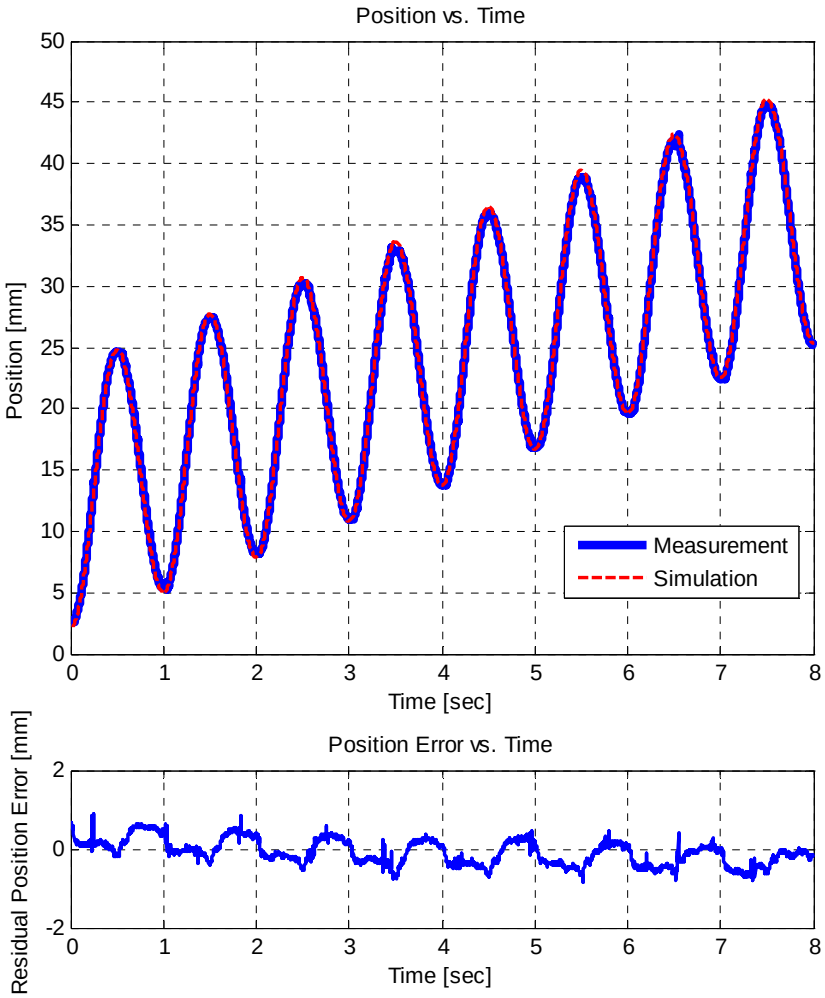

Figure 3-15 Measured and simulated position responses of the open-loop system and residual error

In Figure 3-16, measured and simulated velocity responses of the open-loop system are given. The velocity of the actuator is estimated from the position measurement by using a kinematic Kalman filter. The residual velocity error is between -17 and $23\,mm/s$ and has an rms value of $4.8\,mm/s$. Hence, the model is in good agreement with the experimental results.

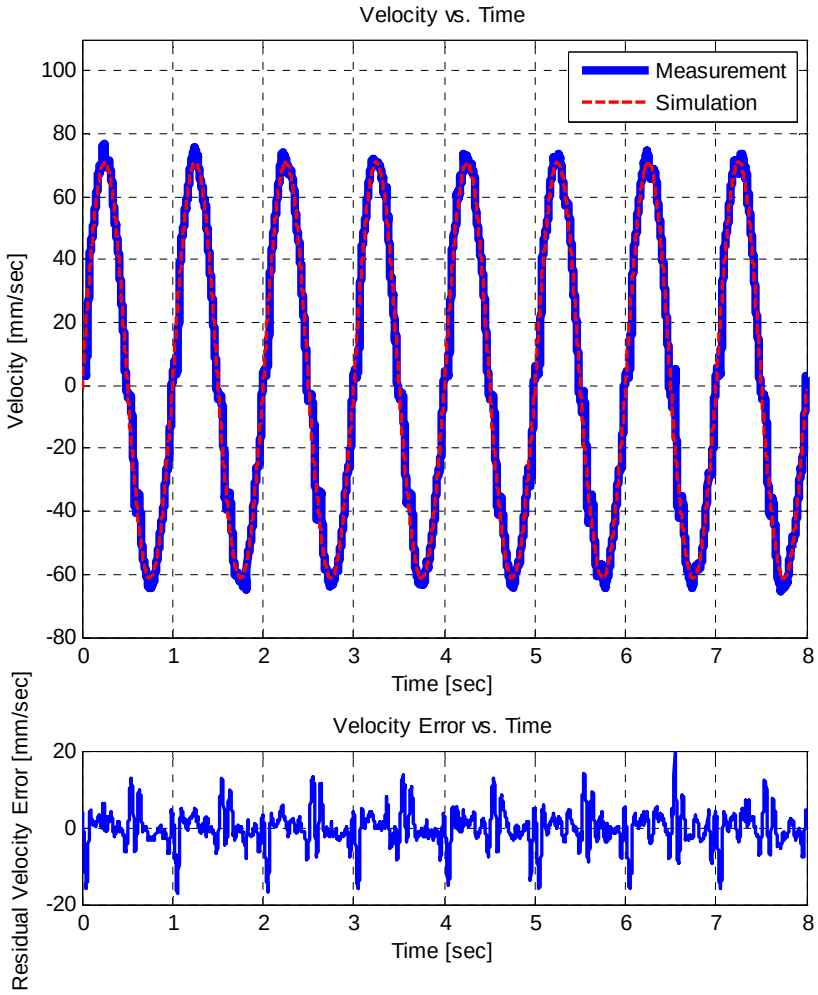

Figure 3-16 Measured and simulated velocity responses of the open-loop system and residual error

Chamber pressures of the hydraulic actuator are compared with the simulation results. In Figure 3-17, the piston (chamber A) and rod (chamber B) side actuator chamber pressure responses obtained during the open-loop tests are plotted and

compared with the simulation results. Although a small off-set between the experimental and simulation results is observed, the dynamic behaviors of the chamber pressures are compatible with the simulation results. This off-set occurs since the value of the supply pressure in the system is slightly higher than the one in the simulation model. However, since their dynamic behaviors are important, the load pressure, which corresponds to the load force obtained in Equation (3.15), is determined and presented in Figure 3-18. The model represents the load pressure dynamics of the system fairly well as seen in the figure. The residual error is between -0.38 and $0.28\ bar$ and its rms value is $0.15\ bar$.

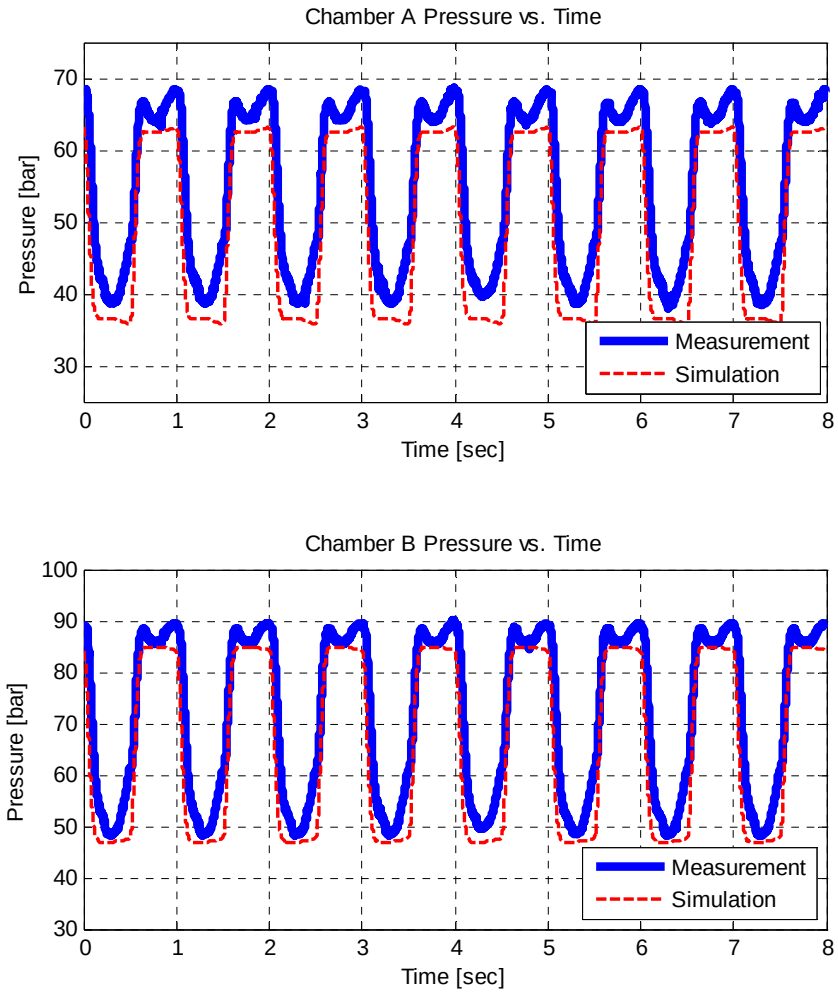

Figure 3-17 Measured and simulated rod and piston side pressure responses of the open-loop system

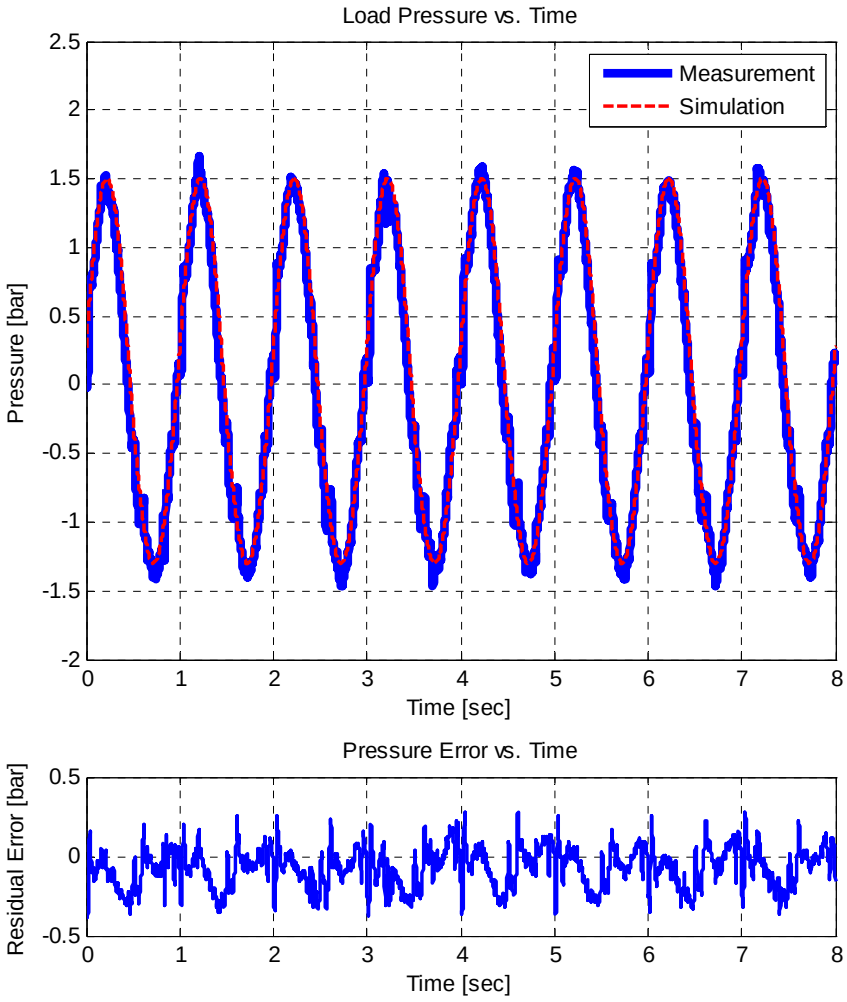

Figure 3-18 Measured and simulated load pressure responses of the open-loop system and residual error

CHAPTER 4

CONTROLLER DESIGN AND IMPLEMENTATION

In this chapter, a force control system of the electro-hydraulic load simulator is designed and implemented. A combined feedforward and feedback control strategy is utilized for the accurate force control of the load simulator. In Section 4.1, the non-linear mathematical model of the electro-hydraulic load simulator is linearized around an operating point and continuous time transfer functions of the system are obtained. In Section 4.2, designs of the disturbance rejection feedforward controller and the combined feedforward and feedback force controller to satisfy the given requirements are explained. A kinematic Kalman filter is designed and tuned in Section 4.3 in order to estimate the velocity of the actuator under test to be utilized in the disturbance feedforward controller. The implementation of the controllers for the real-time experiments by using MATLAB®/Simulink® is explained in Section 4.4.

4.1 Linearization of the Mathematical Model

There are two main non-linearities associated with the valve controlled differential hydraulic actuator, namely, the difference between the pressure areas in each chambers of the hydraulic actuator and the non-linear pressure – flow characteristic of the valve.

The difference between the pressure areas of the piston and rod side chambers of the hydraulic actuator results in different steady state velocities and different steady state chamber pressures for a given valve opening in retraction and extension of the

actuator. Therefore, the steady state characteristics of the system are investigated both for retraction and extension of the hydraulic piston. For these two cases, the algebraic non-linear flow equations describing the pressure – flow characteristic of the valve are separately linearized around an operating point. Transfer functions of the load simulator are determined for these two phases of motion.

For the hydraulic system shown in Figure 3-1, the piston and rod side areas are denoted by A_A and A_B, respectively. However, the piston area A_p, and the area ratio α are used in the remaining of this study for notational convenience. Their definitions are given below.

$$A_p = A_A, \qquad \alpha = \frac{A_B}{A_A} \tag{4.1}$$

where $\alpha < 1$.

4.1.1 Steady State Characteristics of the System

For a differential (or single rod) hydraulic actuator, the steady state retraction and extension velocities are different for the same valve opening because of different pressure areas of each chamber. The steady state extension velocity is greater than the steady state retraction velocity for the same valve opening. In addition, the steady state chamber pressures for extension and retraction cases are different from each other.

At steady state, effects of compressibility at both chambers of the hydraulic actuator die out, and the flow continuity equations given in Equations (3.13) and (3.14) become

$$Q_{A0} = A_p \dot{x}_{p0} \tag{4.2}$$

$$Q_{B0} = \alpha A_p \dot{x}_{p0} \tag{4.3}$$

At this stage, it is a common practice to introduce the *load pressure*, which is defined as follows [41]:

$$p_L = p_A - \alpha p_B \tag{4.4}$$

For a positive valve opening $x_v \geq 0$, the valve equations defined for the extension case in Equations (3.8) and (3.9) are combined with Equations (4.2) and (4.3) to yield to

$$\frac{Q_{A0}}{Q_{B0}} = \frac{K_v x_v \sqrt{p_s - p_{A0}}}{K_v x_v \sqrt{p_{B0}}} = \frac{A_p \dot{x}_{p0}}{\alpha A_p \dot{x}_{p0}} \tag{4.5}$$

which can be simplified to the following form so as to represent a steady state relationship between the chamber pressures.

$$\alpha^2 p_s = \alpha^2 p_{A0} + p_{B0} \tag{4.6}$$

By introducing the load pressure p_L defined in Equation (4.4) into the above equation, the steady state chamber pressures for extension ($x_v \geq 0$) are determined as

$$p_{A0} = \frac{1}{1+\alpha^3}(p_L + \alpha^3 p_s) \tag{4.7}$$

$$p_{B0} = \frac{-\alpha^2}{1+\alpha^3}(p_L - p_s) \tag{4.8}$$

For a negative valve opening $x_v < 0$, the valve equations defined for the retraction case in Equations (3.10) and (3.11) are combined with Equations (4.2) and (4.3) to yield to

$$\frac{Q_{A0}}{Q_{B0}} = \frac{K_v x_v \sqrt{p_{A0}}}{K_v x_v \sqrt{p_s - p_{B0}}} = \frac{A_p \dot{x}_{p0}}{\alpha A_p \dot{x}_{p0}} \tag{4.9}$$

which simplifies to the following form so as to represent a steady state relationship between the chamber pressures.

$$p_s = \alpha^2 p_{A0} + p_{B0} \tag{4.10}$$

By introducing the load pressure p_L defined in Equation (4.4) into the above equation, the steady state chamber pressures for retraction ($x_v < 0$) are determined as follows:

$$p_{A0} = \frac{1}{1+\alpha^3}(p_L + \alpha p_s) \tag{4.11}$$

$$p_{B0} = \frac{1}{1+\alpha^3}(p_s - \alpha^2 p_L) \tag{4.12}$$

4.1.2 Linearized Valve Coefficients

The non-linear algebraic equations representing the pressure – flow characteristic of the valve for the extension and retraction cases are linearized in this section.

The flow equation $Q = Q(x_{v_o}, p_o)$ given in Equation (3.2) can be linearized by using Taylor series expansion about an operating point $P_o(x_{v_o}, p_o)$ and by neglecting the higher order terms one obtains the following equation in terms of deviations of respective variables from the operating point. Note that Δ operator is utilized to indicate deviations in respective variables.

$$\Delta Q = \left.\frac{\partial Q}{\partial x_v}\right|_{x_{v_o}, p_0} \Delta x_v + \left.\frac{\partial Q}{\partial p}\right|_{x_{v_o}, p_o} \Delta p \tag{4.13}$$

where the *flow gain* K_q is defined by

$$K_q = \frac{\partial Q}{\partial x_v}\Big|_{x_{v_o}, p_0} \tag{4.14}$$

and the *pressure-flow coefficient* K_c is expressed by

$$K_c = -\frac{\partial Q}{\partial p}\Big|_{x_{v_o}, p_0} \tag{4.15}$$

Since $\partial Q/\partial p$ is always negative, the flow-pressure coefficient is also positive [40].

Therefore, the flow equations for extension, Equations (3.8) and (3.9), and for retraction, Equations (3.10) and (3.11), are linearized around an operating point $P_o(x_{v_o}, p_{A_o}/p_{B_o})$ to yield to the following linear expressions:

$$\Delta Q_A = K_{q_A}\Delta x_v - K_{c_A}\Delta p_A \tag{4.16}$$

$$\Delta Q_B = K_{q_B}\Delta x_v - K_{c_B}\Delta p_B \tag{4.17}$$

where the flow gains are

$$K_{q_A} = \frac{\partial Q_A}{\partial x_v}\Big|_{x_{v_o}, p_{A_o}} = \begin{cases} K_v\sqrt{p_s - p_{A_o}} & \text{for } x_v \geq 0 \\ K_v\sqrt{p_{A_o}} & \text{for } x_v < 0 \end{cases} \tag{4.18}$$

$$K_{q_B} = \frac{\partial Q_B}{\partial x_v}\Big|_{x_{v_o}, p_{B_o}} = \begin{cases} K_v\sqrt{p_{B_o}} & \text{for } x_v \geq 0 \\ K_v\sqrt{p_s - p_{B_o}} & \text{for } x_v < 0 \end{cases} \tag{4.19}$$

and the flow-pressure coefficients are

$$K_{c_A} = -\frac{\partial Q_A}{\partial p_A}\Big|_{x_{v_o}, p_{A_o}} = \begin{cases} \dfrac{K_v x_{v_o}}{2\sqrt{p_s - p_{A_o}}} & \text{for } x_v \geq 0 \\ -\dfrac{K_v x_{v_o}}{2\sqrt{p_{A_o}}} & \text{for } x_v < 0 \end{cases} \tag{4.20}$$

$$K_{c_B} = -\frac{\partial Q_B}{\partial p_B}\bigg|_{x_{v_o}, p_{B_o}} = \begin{cases} -\dfrac{K_v x_{v_o}}{2\sqrt{p_{B_o}}} & \text{for } x_v \geq 0 \\ \dfrac{K_v x_{v_o}}{2\sqrt{p_s - p_{B_o}}} & \text{for } x_v < 0 \end{cases} \tag{4.21}$$

4.1.3 Linear Transfer Function Models of the System

In this sub-section, the transfer functions of the system are derived to be used in control system design and analysis.

In order to eliminate the pressures p_A and p_B from Equations (4.16) and (4.17), the static relations, given in Equations (4.7) and (4.8), or equivalently in Equations (4.11) and (4.12), are linearized to yield to

$$\Delta p_A = \frac{1}{1+\alpha^3}\Delta p_L \tag{4.22}$$

$$\Delta p_B = -\frac{\alpha^2}{1+\alpha^3}\Delta p_L \tag{4.23}$$

Then, the linearized valve equations can be rewritten by using Equations (4.22) and (4.23) as follows:

$$\Delta Q_A = K_{q_A}\Delta x_v - K_{c_A}\frac{1}{1+\alpha^3}\Delta p_L \tag{4.24}$$

$$\Delta Q_B = K_{q_B}\Delta x_v + K_{c_B}\frac{\alpha^2}{1+\alpha^3}\Delta p_L \tag{4.25}$$

Since it is clear that only linear mathematical models are the concern of this chapter, the use of Δ operator will be omitted for the remaining of the study.

The flow continuity equations given in Equations (3.13) and (3.14) can be rearranged to give the pressure dynamics equations as follows:

$$\dot{p}_A = \frac{\beta}{V_A}\left(Q_A - A_p\dot{x}_p\right) \tag{4.26}$$

$$\dot{p}_B = \frac{\beta}{V_B}\left(-Q_B + \alpha A_p\dot{x}_p\right) \tag{4.27}$$

The load pressure equation in Equation (4.4) is differentiated to result into the following expression:

$$\dot{p}_L = \dot{p}_A - \alpha\dot{p}_B \tag{4.28}$$

Hence, first Equations (4.24) and (4.25) are inserted into Equations (4.26) and (4.27), respectively, in order to eliminate the flow terms, and then the resulting equations are substituted into Equations (4.28) to yield to

$$Q_L = K_q x_v - K_c p_L = C\dot{p}_L + A\dot{x}_p \tag{4.29}$$

where Q_L can be assumed as a *virtual load flow*.

Parameters K_q, K_c, C, and A used in Equations (4.29) are expressed by

$$K_q = K_{q_A} + \alpha\frac{V_A}{V_B}K_{q_B} \tag{4.30}$$

$$K_c = \frac{1}{1+\alpha^3}K_{c_A} - \frac{\alpha^3}{1+\alpha^3}\frac{V_A}{V_B}K_{c_B} \tag{4.31}$$

$$C = \frac{V_A}{\beta} \tag{4.32}$$

$$A = \left(1 + \alpha^2\frac{V_A}{V_B}\right)A_p \tag{4.33}$$

Furthermore, the load model given in Equation (3.18) is rewritten here by introducing load pressure in Equation (4.4) as follows:

$$m_p\ddot{x}_p + b_p\dot{x}_p + k_s x_p = A_p p_L + k_s x_d \tag{4.34}$$

The ultimate control variable for the load simulator is the force applied by the actuator of the load simulator onto the actuator under test and it is defined in Equation (3.19). Also, the transfer function representing the dynamics between the input signal to the valve driver $U(s)$ and the spool position $X_v(s)$ is given in Equation (3.12). Therefore, by taking the Laplace transforms of Equations (3.19), (4.29) and (4.34), and by using them with Equation (3.12), the block diagram representation of the hydraulic load simulator is obtained as given in Figure 4-1. It can be seen in the figure that the model has two inputs, namely, the control input to the valve $U(s)$ and the motion of the test actuator $X_d(s)$ which acts as a disturbance input. The controlled output of the system is the force applied onto the test actuator by the load simulator $F(s)$. Note that the block diagram representation of the system is valid both for extension and retraction cases of the hydraulic actuator of the load simulator, but the valve parameters K_q and K_c are to be evaluated for each case with the given control input and the corresponding steady state chamber pressures.

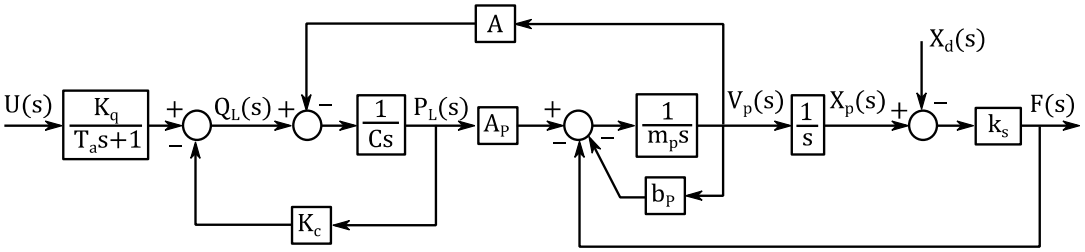

Figure 4-1 Block diagram representation of the hydraulic load simulator

By using Figure 4-1, the following expression for the output force applied $F(s)$ in terms of the input signal to the valve driver $U(s)$ and the disturbance input $X_d(s)$ is obtained:

$$F(s) = G_{FU}(s)U(s) + G_{FX_d}(s)X_d(s) \tag{4.35}$$

where the corresponding transfer functions are expressed as

$$G_{FU}(s) = \frac{K_q k_s A_p}{(T_a s + 1)\left(Cm_p s^3 + \left(Cb_p + K_c m_p\right)s^2 + \left(K_c b_p + AA_p + Ck_s\right)s + K_c k_s\right)} \tag{4.36}$$

$$G_{FX_d}(s) = -k_s \frac{Cm_p s^3 + \left(Cb_p + K_c m_p\right)s^2 + \left(K_c b_p + AA_p\right)s}{Cm_p s^3 + \left(Cb_p + K_c m_p\right)s^2 + \left(K_c b_p + AA_p + Ck_s\right)s + K_c k_s} \tag{4.37}$$

Valve coefficients, namely, the flow gain, K_q and the flow-pressure coefficient K_c are highly important model parameters while considering the stability and dynamic characteristics of the system [40]. The open-loop gain of the system is directly affected from the flow gain whereas the system damping depends on the flow-pressure coefficient of the valve.

Valve coefficients depend on the operating point as given in equations from (4.18) to (4.21), and the most crucial operating point is the origin of the flow pressure-flow curve, where $P_o\left(x_{v_o}, p_{L_o}\right) = P_o(0,0)$. At this point, the valve flow gain attains its maximum value, resulting in a high DC gain of the system, whereas the flow-pressure coefficient is at its minimum, giving a low damping ratio. Thus, P_o is the most crucial operating point for system stability, and generally, a system stable at this point results in stable operation at other operating points [40].

As a result, in this study, the valve coefficients are evaluated around the critical operating point $P_o(0,0)$ and the resulting coefficients are named as *null valve coefficients* [40]. The m-file used to determine the transfer functions of the system both in extension and retraction cases is supplied in Appendix E. The transfer functions of the system are determined by using numerical values for the model parameters given in Table 3-1 as follows:

- For the extension of the actuator $x_v \geq 0$,

$$G_{FU}^{ext}(s) = \frac{2.53 \cdot 10^4}{(0.002s + 1)(1.4 \cdot 10^{-7} s^3 + 1.14 \cdot 10^{-4} s^2 + s)} \tag{4.38}$$

$$G_{FX_d}^{ext}(s) = -1110\frac{1.43\cdot 10^{-7}s^2 + 1.17\cdot 10^{-4}s + 1}{1.4\cdot 10^{-7}s^2 + 1.14\cdot 10^{-4}s + 1} \tag{4.39}$$

- For the retraction of the actuator $x_v < 0$,

$$G_{FU}^{ret}(s) = \frac{2.19\cdot 10^4}{(0.002s+1)(1.4\cdot 10^{-7}s^3 + 1.14\cdot 10^{-4}s^2 + s)} \tag{4.40}$$

$$G_{FX_d}^{ret}(s) = -1110\frac{1.43\cdot 10^{-7}s^2 + 1.17\cdot 10^{-4}s + 1}{1.4\cdot 10^{-7}s^2 + 1.14\cdot 10^{-4}s + 1} \tag{4.41}$$

Note that around the critical operating point $P_o(0,0)$ the equivalent pressure-flow coefficients K_c are zero both for extension and retraction cases, and only the equivalent flow coefficients K_q are different from each other, i.e., $K_q^{ext} > K_q^{ret}$. The open-loop poles and zeros of the transfer functions in Equations (4.38), (4.39), (4.40), and (4.41) are given in Table 4-1. Bode magnitude and phase diagrams of the open-loop system for both extension and retraction cases are obtained in Figure 4-2 by using Equations (4.38) and (4.40).

Table 4-1 Open-loop poles and zeros of the plant transfer functions

	Poles $[rad/s]$	Zeros $[rad/s]$
$G_{FU}^{ext}(s)$	0 -500 $-407 \pm j2610$	$-$
$G_{FU}^{ret}(s)$	0 -500 $-407 \pm j2610$	$-$
$G_{FX_d}^{ext}(s), G_{FX_d}^{ret}(s)$	$-407 \pm j2610$	$-410 \pm j2613$

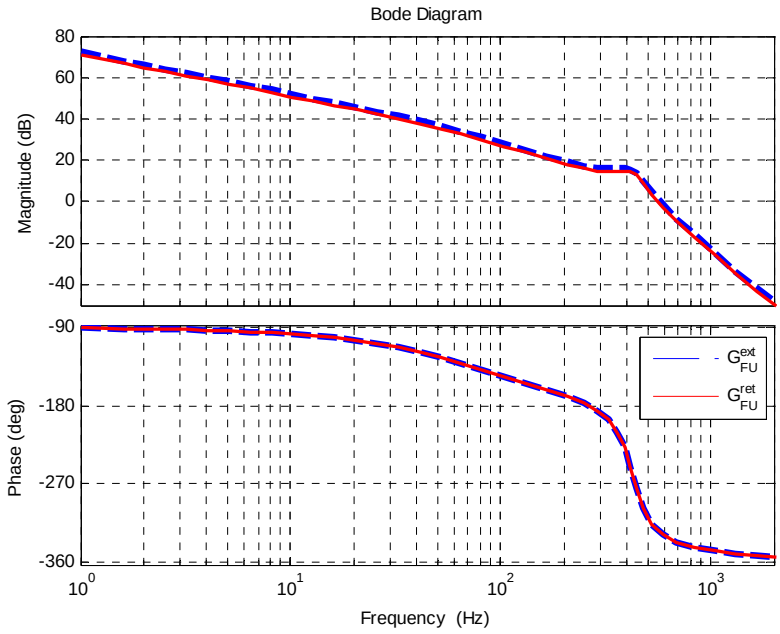

Figure 4-2 Open-loop Bode diagrams of the hydraulic load simulator

Two important behaviors of a hydraulic actuator can clearly be observed in the figure. One is the integrating nature of the hydraulic actuator and it is observed in the low frequency region with a slope of $-20\ dB/dec$. The other is the interaction of the mass of the hydraulic piston and the effect of compressibility of the hydraulic fluid resulting in a resonant mode as seen in the high frequency range at around $\omega = 425\ Hz\ (2670\ rad/s)$.

4.2 Controller Design

In this section, the design of the force control system for the electro-hydraulic load simulator is presented. The controller design is based on the continuous time transfer functions of the system, which are obtained in the previous section by linearizing the non-linear mathematical model of the system for both the extension and retraction phases of the actuator.

Performances of the load simulators are often evaluated based on the *dual ten index*, which requires that the amplitude and phase distinctions between the reference and the actual control variable are not more than $1\ dB$, and 10^o, respectively [53, 54]. Therefore, it is required that the dual ten bandwidth of the control system should be $10\ Hz$ to apply the dynamic loads specified in Chapter 2.1.

The overall control architecture together with the plant model is given in Figure 4-3. It consists of a force feedback controller, a force reference (or set-point) feedforward and a disturbance feedforward controller. Here, it is aimed to achieve an enhanced dynamic performance and stability with a closed-loop controller $G_c(s)$, whereas the dynamic errors are diminished thanks to the reference and disturbance feedforward controllers, which are denoted by $F_u(s)$ and $F_d(s)$, respectively.

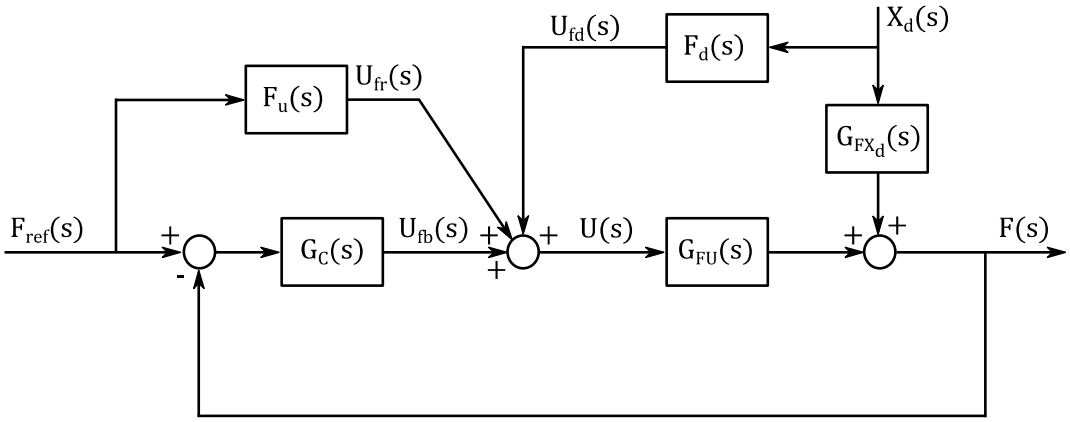

Figure 4-3 Overall control architecture

Even though the use of feedback is very effective in stabilizing and achieving an improved dynamics for a control system, the use of an additional feedforward is commonly considered to be a powerful technique complementing the feedback [55]. Since an error is to be developed before a feedback controller responds, it is considered as reactive. On the other hand, feedforward is pro-active as it responds to changes in the measured inputs before an error actually develops in the controlled

variable [56]. An important drawback of the feedforward is its dependency on modeling errors because of its open-loop nature. Therefore, a concurrent use of feedback and feedforward controllers is often considered to be highly advantageous [56].

A combined feedforward and feedback control strategy is utilized in this study in order to achieve an improved tracking performance to reference force inputs and to attenuate the undesirable effect of the disturbance motion of the hydraulic drive system under test at the same time. Thus, first a disturbance feedforward compensation scheme is developed, and then the reference tracking performance of the system is designed by assuming a disturbance free plant.

4.2.1 Disturbance Feedforward Controller

In order to attenuate the effect of the disturbance caused by the motion of the actuator under test, a feedforward compensator is designed in this section. The disturbance feedforward controller is denoted in Figure 4-3 by the transfer function $F_d(s)$. Assuming that $F_{ref}(s) = 0$, the transfer function between the disturbance $X_d(s)$ and the controlled output $F(s)$ is determined as

$$G_{FX_d}(s) = \frac{F_d(s)G_{FU}(s) + G_{FX_d}(s)}{1 + G_c(s)G_{FU}(s)} \tag{4.42}$$

where the ideal disturbance rejection performance can be obtained by letting

$$F_d(s) = -\frac{G_{FX_d}(s)}{G_{FU}(s)} \tag{4.43}$$

Similar to the reference feedforward design, the extension and retraction cases are considered separately since the open-loop gains of the system in these cases are

different. Therefore, by inserting Equations (4.38) and (4.39) into Equation (4.43), the disturbance feedforward compensator for extension case is obtained as follows:

$$F_d^{ext}(s) = 1.2 \cdot 10^{-11}s^4 + 1.6 \cdot 10^{-8}s^3 + 9.2 \cdot 10^{-5}s^2 + 0.043s \qquad (4.44)$$

Similarly, Equations (4.40) and (4.41) are inserted into Equation (4.43) to obtain the disturbance feedforward controller for retraction case as follows:

$$F_d^{ret}(s) = 1.4 \cdot 10^{-11}s^4 + 1.9 \cdot 10^{-8}s^3 + 10.6 \cdot 10^{-5}s^2 + 0.051s \qquad (4.45)$$

Last terms in Equations (4.44) and (4.45) represent the compensation of the disturbance caused by the velocity of the actuator under test whereas the remaining terms are the compensations for disturbances related to the higher order derivatives of its motion. Since in this study only the position of the actuator under test is measured via a linear encoder, the higher order derivatives of its motion have to be estimated. In this study, only the term related to the velocity of the actuator is considered in the feedforward controller by estimating its velocity. The other terms are neglected since it is generally very hard to estimate higher order derivatives with a reasonable accuracy, and their contributions to the overall control signal are relatively small. To illustrate, if the motion of the disturbance actuator is expressed by $x_d(t) = 5\sin(40 \cdot t)$ mm, then the control signals related to the compensations for its velocity, acceleration, and jerk are 10, 0.8 and 0.005 $Volt$, respectively.

Therefore, the disturbance feedforward controller is given for extension and retraction cases by

$$F_d^{ext}(s) = \frac{U_{fd}(s)}{X_d(s)} = 0.043s \qquad (4.46)$$

$$F_d^{ret}(s) = \frac{U_{fd}(s)}{X_d(s)} = 0.051s \qquad (4.47)$$

In the next section, a kinematic Kalman filter is designed to estimate the velocity of the actuator under test. Assuming ideal velocity estimation via the KKF, the normalized Bode magnitude diagrams $F(j\omega)/k_s X_d(j\omega)$ showing the expected improvement in disturbance rejection performance of the load simulator with the use of feedforward controllers in Equations (4.46) and (4.47) are illustrated in Figure 4-4.

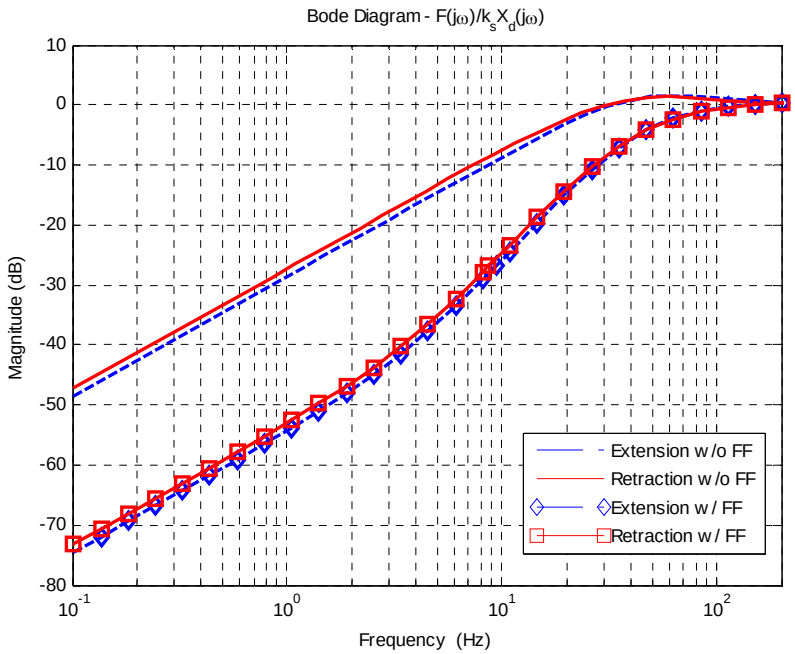

Figure 4-4 Bode magnitude diagram of $F(j\omega)/k_s X_d(j\omega)$

4.2.2 Force Feedback Controller with a Reference Feedforward

In this section, a combined feedforward and feedback force controller is designed by assuming that the effect of disturbance is completely eliminated by the disturbance feedforward controller designed in the previous section.

It is clear from Equations (4.38) and (4.40), and Figure 4-2 that the DC gain of the system in extension of the actuator is greater than that of the actuator in retraction. Therefore, in designing the feedback controller, first the extension case will be

considered since its stability is more critical. Then, the performance of the resulting controller will be observed to see whether it is acceptable for the retraction case.

Consider a proportional controller with a gain of K_p for the extension of the hydraulic actuator. The open-loop Bode plots of the system for the extension case are given for different values of the proportional controller gain in Figure 4-5 to result in stable closed-loop operations. The closed-loop Bode diagrams of the system for the same controller gains are also given in Figure 4-6. Although the $1\,dB$ magnitude requirement can be satisfied with the small values of the proportional controller gain ($K_p = 0.004$), the phase lag of the closed-loop system is considerably higher than the 10^o phase requirement (about -34^o). Thus, it is required to use greater controller gains, such as $K_p = 0.015$, as seen in Figure 4-6. As can be seen in the figure, for this controller gain, the closed-loop system satisfies the dual ten bandwidth

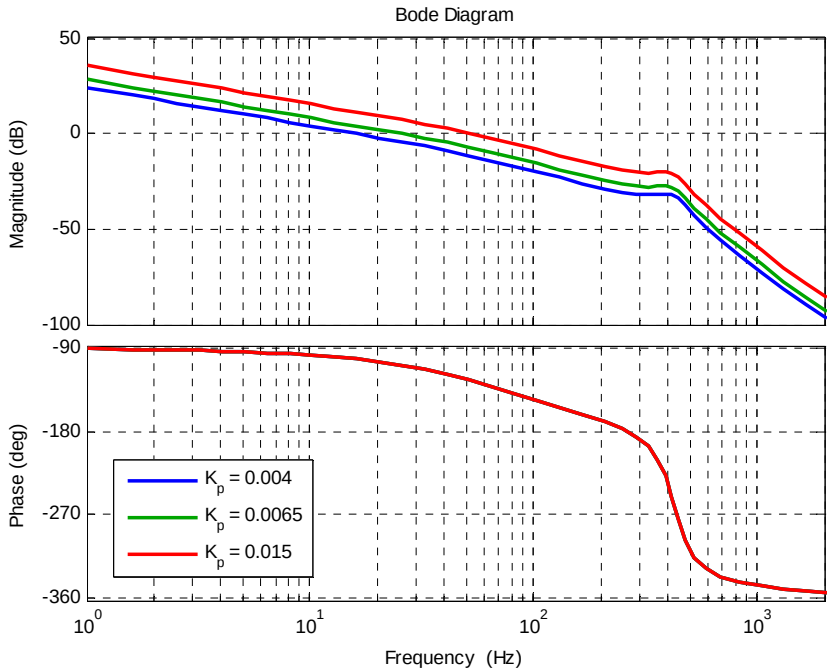

Figure 4-5 Open-loop Bode diagrams in extension case for different proportional controllers

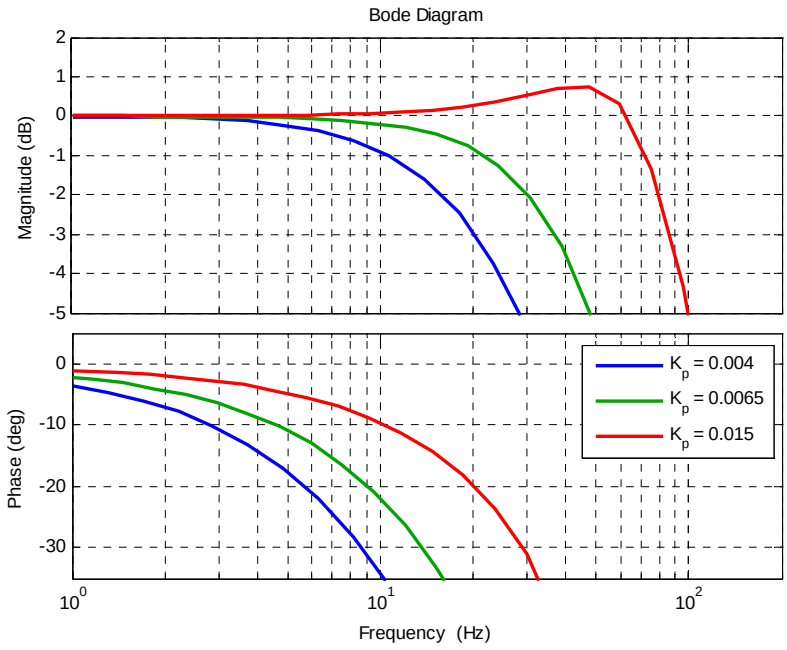

Figure 4-6 Closed-loop Bode diagrams in extension case for different proportional controllers

requirement, and the $-3\ dB$ bandwidth of the red curve is about $86\ Hz$. However, the use of large closed-loop controller gains is generally undesired since it increases the noise sensitivity, and causes both the saturation of the control valve and the excitation of the un-modeled dynamics.

A proportional controller can be utilized to achieve a reasonable bandwidth of the closed-loop system with a good phase margin. In order to achieve an improved tracking performance, a reference feedforward compensation can then be introduced without affecting the stability of the closed-loop system. Hence, dynamic errors are further reduced with the use of the feedforward compensation.

Since the type number of the open-loop transfer functions obtained by linearization around the critical operating point (zero valve opening and load pressure) is unity, and thanks to the high flow gain of the control valve, the integral action is not considered for the force control loop. Although it is known that the integral action is

also effective in rejecting the disturbance in low and mid-frequency range, a disturbance feedforward controller is considered in the next section to fulfill this requirement.

The gain of the proportional controller is selected as $K_p = 0.0065$, which satisfies the magnitude requirement but not the phase requirement. The open-loop and closed-loop Bode diagrams of the system with the proportional controller are given in Figure 4-7 and Figure 4-8, respectively, and its frequency domain specifications are summarized in Table 4-2 for both extension and retraction cases.

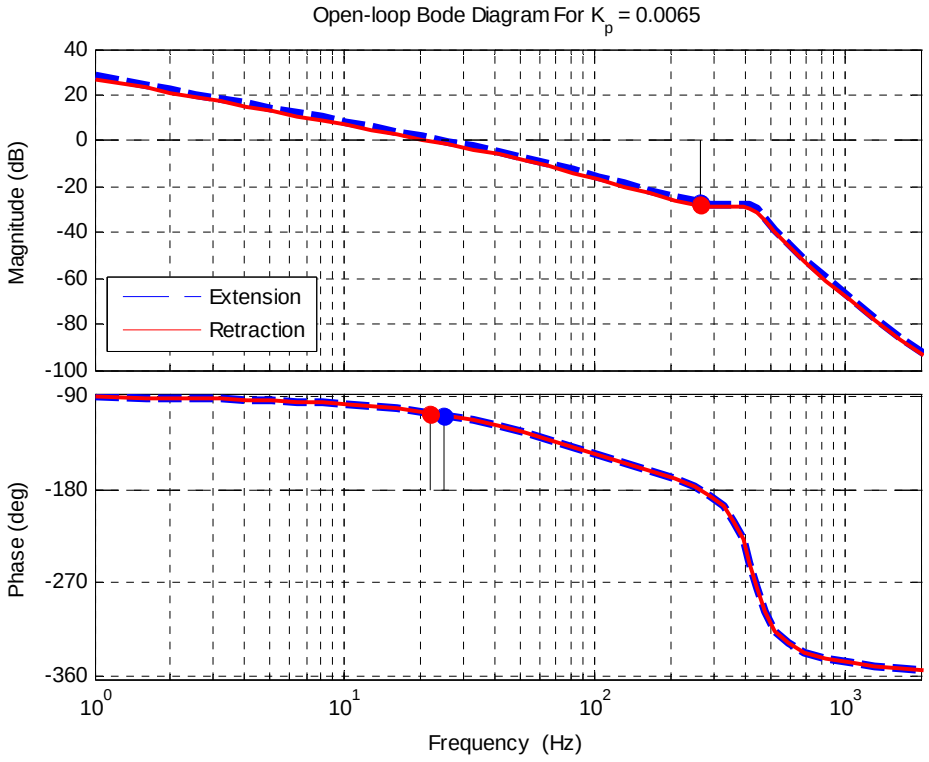

Figure 4-7 Open-loop Bode diagrams for $K_p = 0.0065$

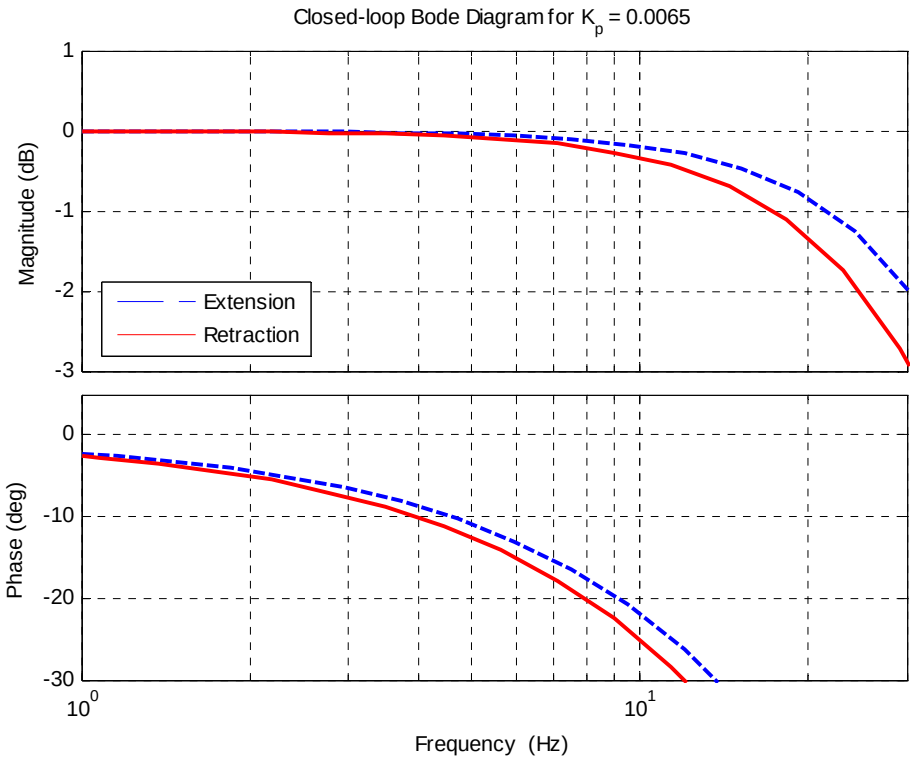

Figure 4-8 Closed-loop Bode diagrams for $K_p = 0.0065$

Table 4-2 Specifications of the closed-loop system with $K_p = 0.0065$

			Extension	Retraction
Bandwidth $(-3\ dB)$		$[Hz]$	36.5	30.6
Phase margin		$[degree]$	71.5	73.8
Gain margin		$[dB]$	26.9	28.2
Dual ten bandwidth	$1\ dB$	$[Hz]$	21.4	17.2
	10^o	$[Hz]$	4.6	3.9
Velocity error constant			164.8	142.7

In order to improve the tracking performance of the system, a reference feedforward controller, $F_u(s)$, is designed by considering the closed-loop block diagram of the system given in Figure 4-3. Assuming that $V_d(s) = 0$, the transfer function between the reference force input, $F_{ref}(s)$, and the force output, $F(s)$, is written as follows:

$$G_{FF_{ref}}(s) = \frac{G_c(s)G_{FU}(s)}{1 + G_c(s)G_{FU}(s)}\left(1 + \frac{F_u(s)}{G_c(s)}\right) \tag{4.48}$$

where the ideal compensation can be obtained by letting

$$F_u(s) = \frac{1}{G_{FU}(s)} \tag{4.49}$$

However, from the open-loop Bode diagrams of the plant given in Figure 4-2, it is seen that the valve dynamics and the resonant mode due to the interaction of the fluid compressibility and piston mass occur at relatively high frequencies. Therefore, only the integrating behavior of the hydraulic system is considered in the design of the feedforward controller. By neglecting these high dynamics in Equation (4.36), the feedforward compensator is obtained by using (4.49) as

$$F_u(s) = K^* \frac{AA_p + Ck_s}{K_q k_s A_p} \frac{s}{T_{LP}s + 1} \tag{4.50}$$

where a low pass filter with a time constant of T_{LP} is utilized to casually realize the compensator, and a scaling factor K^* is introduced to prevent the over-compensation of the controller [57]. It should also be noted here that since the DC gain of the hydraulic system is different in extension and retraction cases, the resulting controllers for these cases are also be different and they will be switched depending on the spool position.

The controller defined by Equation (4.50) introduces a real zero and pole to provide a lead effect in the closed-loop system as given in (4.48). Assuming $K^* = 1$, the

angular contribution of the controller to the closed-loop system at a frequency ω, which is denoted by ϕ, is given as

$$\phi = \tan^{-1}\left(\omega\left(T_{LP} + \frac{AA_p + Ck_s}{K_q k_s A_p}\frac{1}{K_p}\right)\right) - \tan^{-1}(\omega T_{LP}) \tag{4.51}$$

In order to have a phase contribution of about $\phi = 20^{\circ}$ at around $\omega = 10\,Hz$, the time constants of the low pass filter T_{LP} are set to $0.001\,s$ by utilizing Equation (4.51). Then, the scaling factors K^* are tuned by using MATLAB®/SISO design tool so as to suppress the resulting resonant peak in the closed-loop responses, and they are found as 0.75 and 0.78 for extension and retraction cases, respectively. The resulting controllers for extension and retraction cases are given in Equations (4.52) and (4.53) as follows:

$$F_u^{ext}(s) = (0.75)(4 \cdot 10^{-5})\frac{s}{0.001s + 1} \tag{4.52}$$

$$F_u^{ret}(s) = (0.78)(4.6 \cdot 10^{-5})\frac{s}{0.001s + 1} \tag{4.53}$$

The closed-loop Bode diagrams of the system with the feedforward compensators are given in Figure 4-9, in which it is clearly seen that the system satisfies the dual ten bandwidth requirement. In addition, the resonant peak of the closed-loop system is limited by $1\,dB$, which is also satisfactory for the transient performance of the system [58].

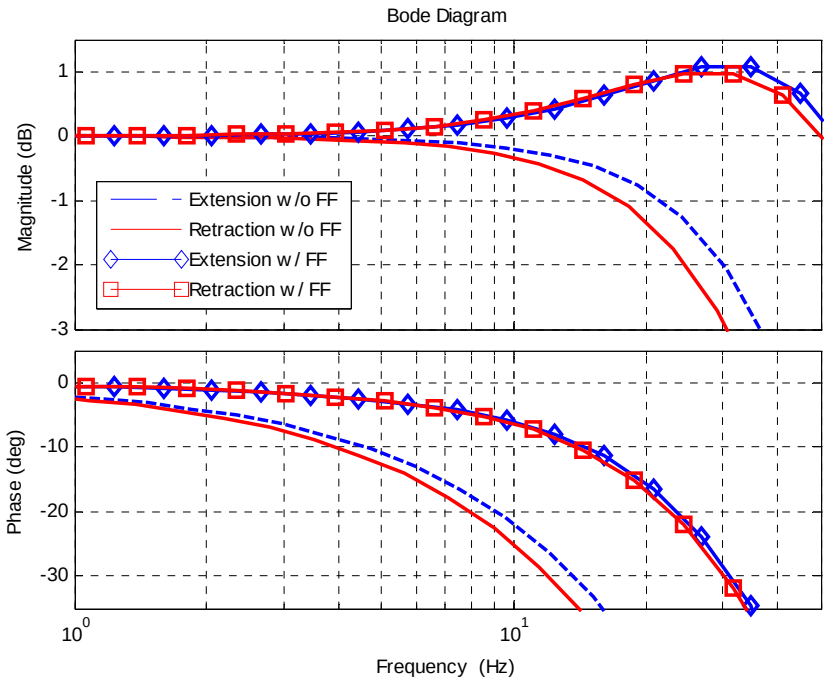

Figure 4-9 Closed-loop Bode diagrams with K_p and F_u

4.3 Velocity Estimation

In this study, an incremental encoder is utilized for the position measurement of the actuator under test and it provides pulses proportional to the velocity of the actuator. Therefore, the velocity of the actuator is to be estimated from these discrete signals, which is a challenging work, particularly in low velocity ranges [59]. Although the use of difference equations to estimate the velocity is the easiest way, it is prone to discretization errors. Hence, there are many methods considered in literature in order to reduce these undesirable effects [60].

The velocity of the test actuator, which is considered as the disturbance input to the load simulator, is estimated by using a discrete Kalman filter with a kinematic model, or a kinematic Kalman filter (KKF). The main advantage of the estimation based on kinematic models is that the filter is independent of the dynamics of the plant. Therefore, it is not affected by the parameter variations or external disturbances [61].

In addition, a Kalman filter provides optimal state estimation by minimizing the mean of the squared error [62].

In this study, the generalized coordinate of the test actuator is denoted by x_d. Hence, the state vector for estimation is given as

$$\mathbf{x} = \begin{bmatrix} x_d \\ \dot{x}_d \\ \ddot{x}_d \end{bmatrix} \tag{4.54}$$

In the following sub-sections, the continuous time kinematic model is first introduced, and then it is discretized. The recursive Kalman filter algorithm is also explained. The filter algorithm developed is implemented in MATLAB®/Simulink® and it is tuned offline by using experimental measurements.

4.3.1 Kinematic Model

In literature, constant velocity and constant acceleration models are commonly used for estimating the velocity of a moving object [63]. They correspond to either second or third order models obtained from simple equations of motion. In this study, a third order model is preferred since it provides an improved velocity estimate with a better estimation error over a second order model [64].

The third order model is generally called as *Wiener process acceleration state model* [64]. In this section, a continuous time Wiener process acceleration model is introduced, and then it is discretized.

It is assumed that the rate of change of the acceleration is modeled by a zero mean white noise $\widetilde{w}(t)$ as follows:

$$\dddot{x}_d = \widetilde{w}(t) \tag{4.55}$$

where the expected value of the noise $E[\widetilde{w}(t)]$ is

$$E[\tilde{w}(t)] = 0 \tag{4.56}$$

Therefore, by using Equation (4.55), the state equation for the continuous time model of the system can be written as

$$\dot{\mathbf{x}}(t) = \mathbf{A}\mathbf{x}(\mathrm{t}) + \mathbf{B}_{\mathbf{w}}\tilde{w}(t) \tag{4.57}$$

where

$$\mathbf{A} = \begin{bmatrix} 0 & 1 & 0 \\ 0 & 0 & 1 \\ 0 & 0 & 0 \end{bmatrix} \qquad \mathbf{B}_{\mathbf{w}} = \begin{bmatrix} 0 \\ 0 \\ 1 \end{bmatrix} \tag{4.58}$$

The corresponding discrete time model with a sample time of T_s is then given as

$$\mathbf{x}_{k+1} = \mathbf{\Phi}\mathbf{x}_k + \mathbf{w}_k \tag{4.59}$$

where Φ is the state transition matrix given as

$$\mathbf{\Phi} = e^{\mathbf{A}T_s} = \begin{bmatrix} 1 & T_s & T_s^2/2 \\ 0 & 1 & T_s \\ 0 & 0 & 1 \end{bmatrix} \tag{4.60}$$

and $\mathbf{w}_k$ is the value of the process noise at the k^{th} step, whose covariance matrix $\mathbf{Q}$ is obtained in [63] as follows:

$$\mathbf{Q} = E[\mathbf{w}_k \mathbf{w}_k^T] = \begin{bmatrix} T_s^5/20 & T_s^4/8 & T_s^3/6 \\ T_s^4/8 & T_s^3/3 & T_s^2/2 \\ T_s^3/6 & T_s^2/2 & T_s \end{bmatrix} \tilde{q} \tag{4.61}$$

Here, $\tilde{q}$ is denoted as the power spectral density of the continuous time process noise and it is a design parameter for tuning this model to represent the actual motion.

4.3.2 The Discrete Kalman Filter Algorithm

In 1960, Kalman proposed a recursive solution method to estimate the state of a process by minimizing the mean of the squared error between the measured and estimated states [62]. The method is applicable for a system described by a linear stochastic difference equation

$$\mathbf{x}_{k+1} = \mathbf{\Phi}\mathbf{x}_k + \mathbf{w}_k \tag{4.62}$$

with an equation for the measurement $\boldsymbol{y}_k$ as

$$\boldsymbol{y}_{\mathrm{k}} = \mathbf{H}\mathbf{x}_k + \mathbf{v}_k \tag{4.63}$$

where $\mathbf{H}$ is the output matrix. The process noise $\mathbf{w}_k$ and measurement noise $\mathbf{v}_k$ are assumed to possess a zero-mean, white Gaussian distribution with the following covariance matrices, $\mathbf{Q}$ and $\mathbf{R}$, respectively.

$$\mathbf{Q} = E[\mathbf{w}_k \mathbf{w}_k^T] \tag{4.64}$$

$$\mathbf{R} = E[\mathbf{v}_k \mathbf{v}_k^T] \tag{4.65}$$

The equations of the Kalman filter algorithm are divided into two main groups, namely, the time update and measurement update equations. The time update and measurement update equations are also called as predictor and corrector equations, respectively.

The predictor equations are responsible for projecting the current state $\mathbf{x}_{k-1}$ and error covariance estimates $\mathbf{P}_{k-1}$ so as to get the priori estimates $\hat{\mathbf{x}}_k^-$ and $\mathbf{P}_k^-$ for the next time step. Time update equations are given as

$$\hat{\mathbf{x}}_k^- = \mathbf{\Phi}\hat{\mathbf{x}}_{k-1} \tag{4.66}$$

$$\mathbf{P}_k^- = \mathbf{\Phi}\mathbf{P}_{k-1}\mathbf{\Phi}^T + \mathbf{Q} \tag{4.67}$$

On the other hand, the corrector equations incorporate the new measurement into the priori estimates $\hat{\mathbf{x}}_k^-$ and $\mathbf{P}_k^-$ to have an improved posteriori estimates $\hat{\mathbf{x}}_k$ and $\mathbf{P}_k$. In the measurement update stage, initially the Kalman gain $\mathbf{K}_k$ is computed as

$$\mathbf{K}_k = \mathbf{P}_k^- \mathbf{H}^T (\mathbf{H}\mathbf{P}_k^- \mathbf{H}^T + \mathbf{R})^{-1} \tag{4.68}$$

which minimizes the error covariance between the measured and estimated states [62].

By using the Kalman gain obtained in Equation (4.68) as the blending factor of the priori estimates and measurements, the posteriori estimates are obtained as

$$\hat{\mathbf{x}}_k = \hat{\mathbf{x}}_k^- + \mathbf{K}_k(\mathbf{y}_k - \mathbf{H}\hat{\mathbf{x}}_k^-) \tag{4.69}$$

$$\mathbf{P}_k = (\mathbf{I} - \mathbf{K}_k\mathbf{H})\mathbf{P}_k^- \tag{4.70}$$

The Kalman filter algorithm is initialized with the initial estimates for the state $\hat{\mathbf{x}}_{k-1}$ and the error covariance $\mathbf{P}_{k-1}$. Then, the predictor-corrector algorithm of the Kalman filter is recursively operated at each time step as seen in Figure 4-10.

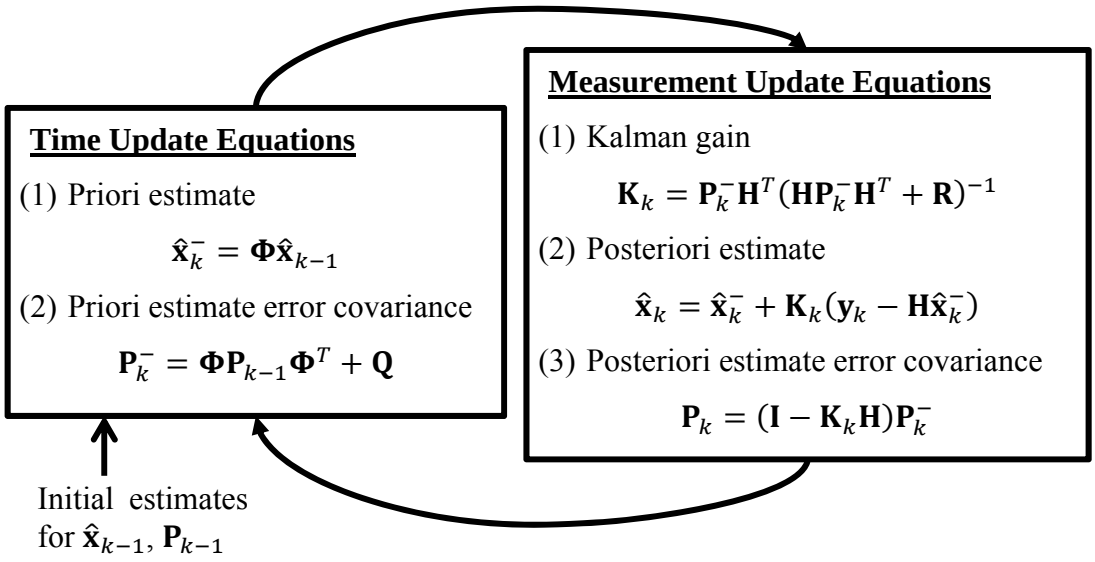

Figure 4-10 Recursive Kalman filter algorithm

4.3.3 Filter Implementation and Tuning

The discrete Kalman filter algorithm to estimate the velocity and acceleration of the actuator under test is realized in MATLAB®/Simulink® as seen in Figure 4-11. In each sub-system, one of the time update (predictor) and measurement update (corrector) equations given in Figure 4-10 is implemented. In addition, the state transition and the output matrices of the kinematic model are specified in the filter as well as the measurement and noise covariance matrices.

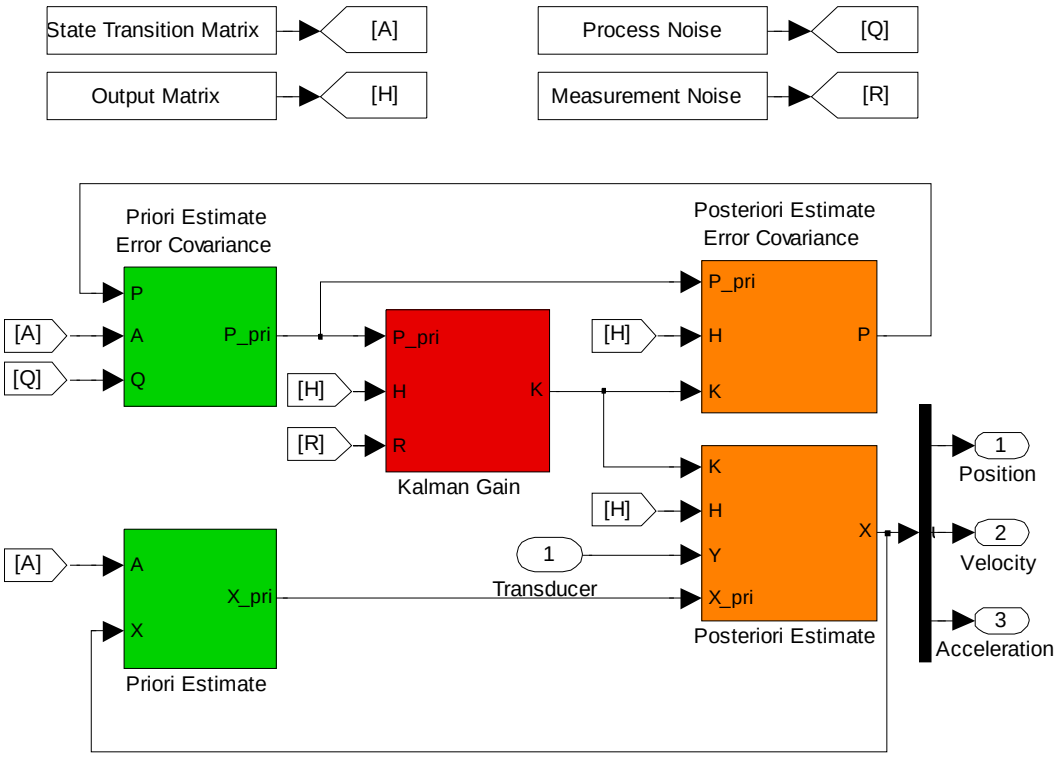

Figure 4-11 MATLAB®/Simulink® implementation of the Kalman filter

The measurement noise covariance **R** is a measure of the quality of the measurement device and can be approximated from the transducer resolution. Further, the process noise covariance matrix **Q** is a measure of the quality of the mathematical model to represent the system, but generally it is not easy to obtain as measurement noise covariance. It is given in Equation (4.61) for the kinematic model described by

Equation (4.59), and it is expressed in terms of the sample time T_s of the DAQ system and the power spectral density of the process $\tilde{q}$. The power spectral density $\tilde{q}$ is a design parameter, and it can be selected such that the value of the expected change in the acceleration over a sample time T_s is in the order of the following expression [63]:

$$\sqrt{Q_{33}} = \sqrt{\tilde{q}T_s} \tag{4.71}$$

Therefore, the selection of a relatively small intensity $\tilde{q}$ results in a nearly constant acceleration (NCA) model and vice versa.

On the other hand, the performance of the filter depends on the relative relationship between the process noise covariance matrix **Q** and the measurement noise covariance matrix **R** [65]. The measurement noise covariance, a scalar in our case since there is a single measurement, is initially fixed according to the resolution of the encoder ($R = 0.005^2\ mm^2$). As the initial starting point for the process noise covariance matrix **Q**, Equation (4.71) is utilized by assuming a reasonable value ($300\ mm/s^2$) to represent the change of acceleration over a sample time T_s. Then, the process noise covariance matrix **Q** is obtained via off-line tuning by using experimental data. It is observed as expected that as the value of the process intensity $\tilde{q}$ increases, the filter yields to noisy velocity and acceleration estimation. On the other hand, the velocity and acceleration estimations become smoother as the process noise covariance is decreased. By tuning the process intensity with experimental data, the process noise covariance matrix **Q** and the measurement noise covariance R are obtained as

$$\mathbf{Q} = \begin{bmatrix} 5 \cdot 10^{-10} & 1.25 \cdot 10^{-6} & 1.67 \cdot 10^{-3} \\ 1.25 \cdot 10^{-6} & 3.33 \cdot 10^{-3} & 5 \\ 1.67 \cdot 10^{-3} & 5 & 10^{4} \end{bmatrix}, \quad R = 25 \cdot 10^{-6} \tag{4.72}$$

The experimental results are given in Figure 4-12 and Figure 4-13 in which the velocity and acceleration estimates obtained by kinematic Kalman filter and backward difference formulas are compared. Note that the velocity is estimated by directly applying the first order backward difference formula for the first derivative, whereas the position data is pre-filtered before applying the first order backward difference formula for the second derivative.

In Figure 4-12, it is seen that the numerical differentiation method (1st order

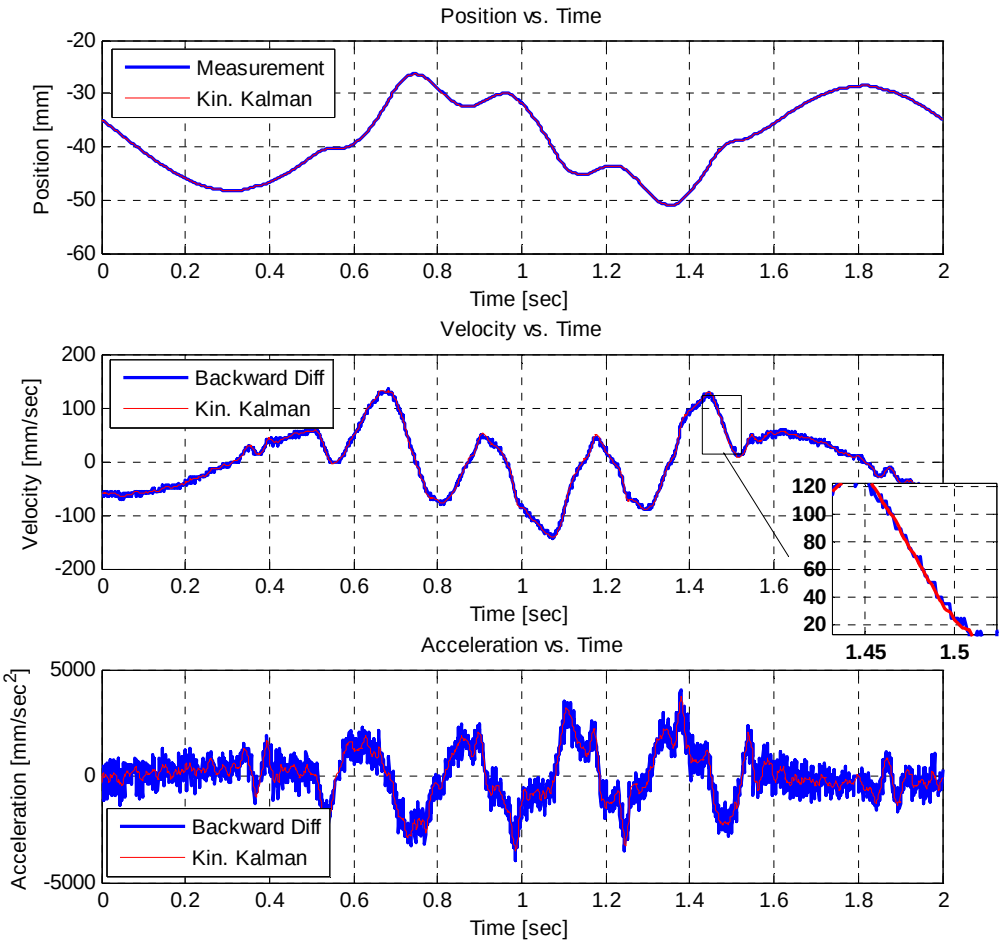

Figure 4-12 Velocity and acceleration estimations with backward difference formula and kinematic Kalman filter – High velocity

backward difference equation) provides relatively good results for velocity estimation at high speeds. However, the consequence of discretization error in low speeds becomes more noticeable as seen in Figure 4-13. On the other hand, kinematic Kalman filter provides better results for both low and high velocities. It is observed that the kinematic Kalman filter provides highly smooth acceleration estimates compared to numerical differentiation as seen both in Figure 4-12 and Figure 4-13.

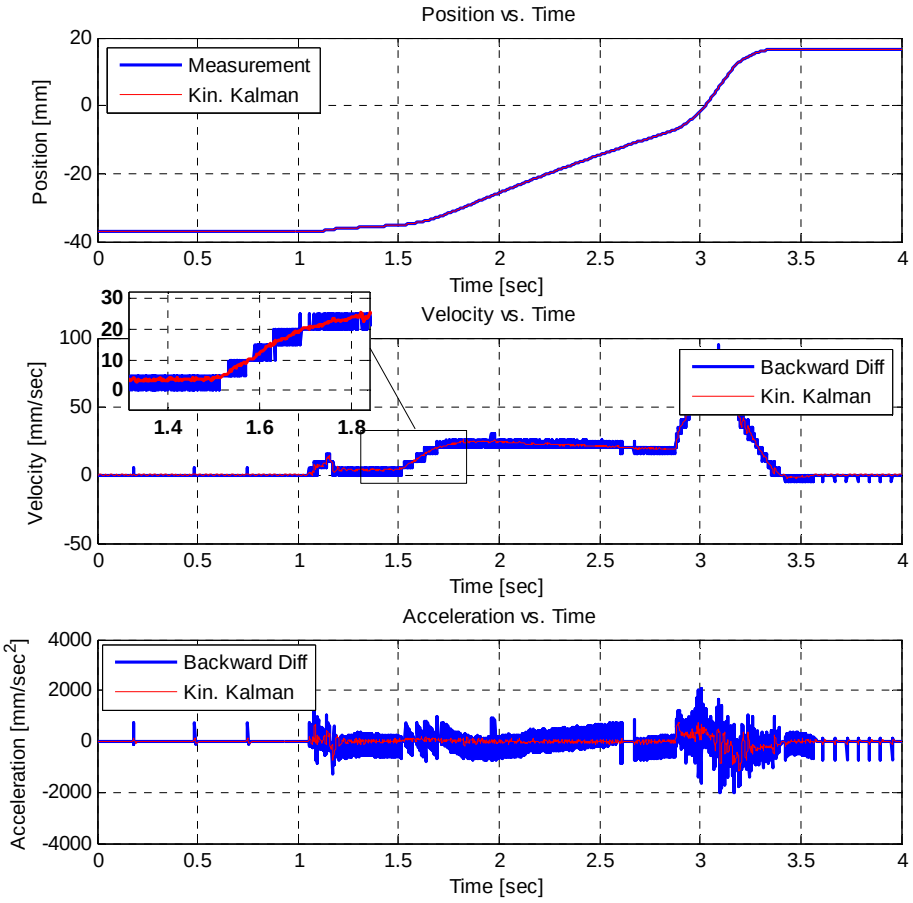

Figure 4-13 Velocity and acceleration estimations with backward difference formula and kinematic Kalman filter – low velocity

4.4 Implementation

In this section, the implementation of the controllers designed in the previous sections into the real-time target machine is explained. A MATLAB®/Simulink® model of the controllers is constructed, compiled, and downloaded to the target machine. This model is utilized in order to perform the real-time experiments to evaluate the performance of the load simulator in the next chapter.

In Figure 4-14, the MATLAB®/Simulink® model of the controllers is illustrated. The model accepts the applied force, spool position, chamber pressures, and the actuator positions of the load simulator and the hydraulic drive system under test as the inputs. The input blocks for the real-time target machine are used under the receive subsystem of the model in order to read the data from terminal boards. The measured analog signals in Volts are converted into the corresponding physical units as N and MPa for applied force and chamber pressure readings, respectively. For pressure readings, look-up tables are constructed by using the calibration results given in Appendix B.1. Similarly, the counter of the incremental encoder is converted into the length unit of mm.

The input signals are then utilized for the control computations. The position of the disturbance actuator is used by the kinematic Kalman filter in order to estimate its velocity so that it is used in the disturbance feedforward controller. On the other hand, reference force signals for the load simulator can easily be created by using the source blocks available in the library of the Simulink®. The reference signal is directly fed through the reference, or set-point, feedforward controller. For both the feedforward controllers, the sign of the spool position feedback determines the required controller gains to be used. For the feedback controller, the error is determined by comparing the reference signal and the measured force signal. The outputs of each controller, in Volts, are summed to get the overall manipulated input signal, which corresponds to the desired valve spool opening.

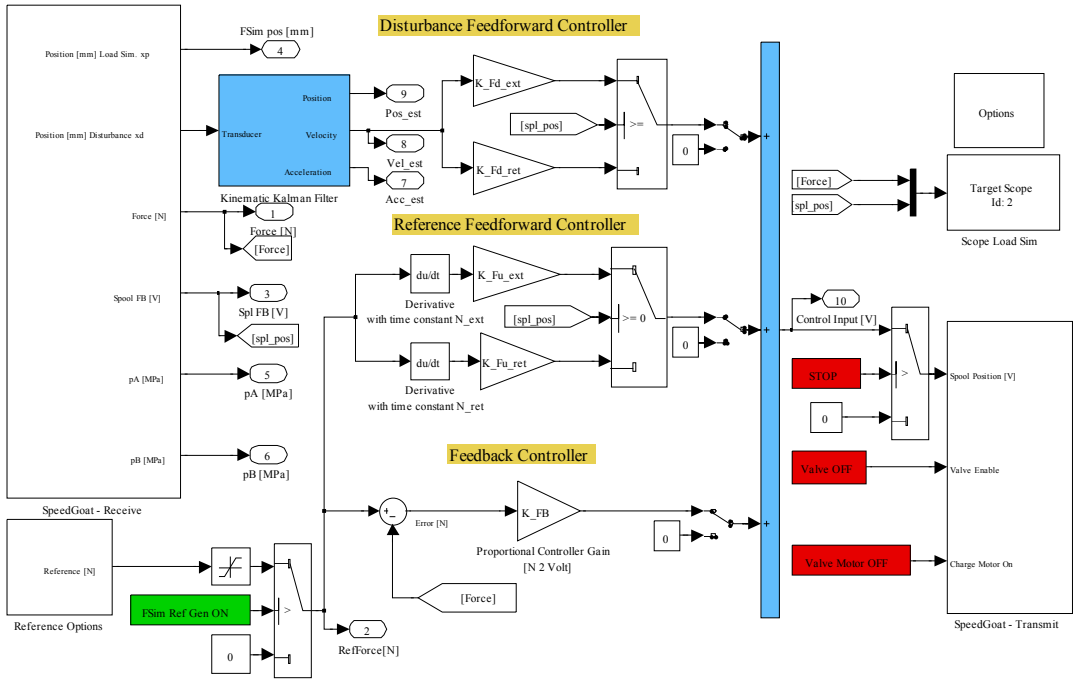

Figure 4-14 Real-time controller of the electro-hydraulic load simulator in MATLAB®/Simulink®

The model outputs the computed value of the manipulated input in order to drive the flow control valve as voltage output. In addition, the enable signals for the valve driver and the AC motor of the constant pressure power pack are also adjusted in the model by using a number of buttons. The output blocks for the real-time target machine are available under the transmit subsystem of the model so as to write the data to the terminal boards.

It should also be stated that although the controller of the hydraulic drive system under test is implemented in the same model, it is not shown in Figure 4-14 as it is not the subject of this study.

The model is developed in a host PC having MATLAB® R2011a (win32) installed together with Simulink® and xPC Target™. A fixed step Runge-Kutta 4th order solver with a sampling time of $1\,ms$ is utilized. From Table 4-2, since the $-3\,dB$

bandwidth of the system is about $\omega_b = 35\ Hz$, a sampling rate of $\omega_s = 1000\ Hz$ is selected, which satisfies the requirement that $20 < \omega_s/\omega_b < 40$ [66]. The controller model is compiled in the host PC and downloaded to the real-time target machine.

CHAPTER 5

PERFORMANCE EVALUATION OF THE LOAD SIMULATOR

In this chapter, the performance of the electro-hydraulic load simulator is evaluated by performing real-time experiments and comparing them with model responses. In Section 5.1, the disturbance rejection performance of the electro-hydraulic load simulator is considered under the influence of a sinusoidal disturbance motion of the hydraulic actuator under test. The effectiveness of the disturbance feedforward controller is shown by comparing the results with and without the feedforward controller. The tracking performance of the load simulator is evaluated in Section 5.2 by performing a frequency sweep for the force reference covering the frequency range of interest. The improvement in the tracking performance is indicated by comparing the results obtained with and without the reference feedforward controller. Some experiments at various loads and frequencies are performed to indicate the operational limits of the electro-hydraulic load simulator in Section 5.3.

5.1 Disturbance Rejection Performance

The motion of the actuator under test is a highly strong disturbance, affecting the force control performance of the electro-hydraulic load simulator. In order to evaluate the disturbance rejection performance of the force controlled load simulator, the actuator under test is requested to apply a disturbance position chirp with a frequency range starting from $0.1\ Hz$ to $7\ Hz$ and a magnitude of $5\ mm$.

Initially the disturbance feedforward controller of the electro-hydraulic load simulator, $F_d(s)$, is disabled, and a zero reference force input is applied, $F_{ref} = 0\ N$. The applied disturbance position x_d and the corresponding velocity v_d are given in Figure 5-1.

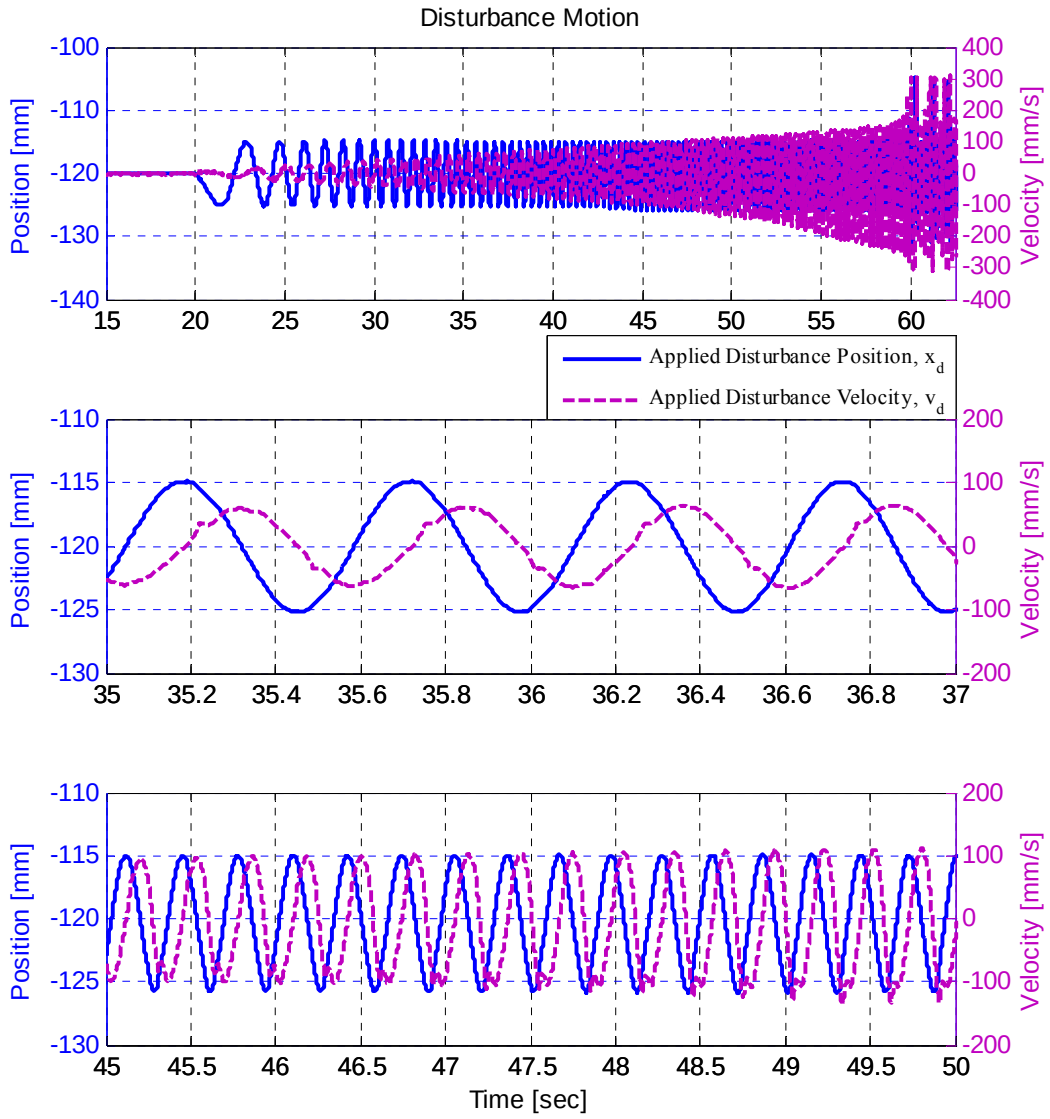

Figure 5-1 Disturbance input applied to the load simulator, x_d, when $F_d(s)$ is disabled

The response of the closed-loop force controlled load simulator, F, under the influence of sinusoidal disturbance motion, x_d, is given in Figure 5-2. It is seen in this figure that as the frequency of the applied disturbance increases the error in the force also increases. To illustrate, when the frequency of the disturbance is about $1.7\ Hz$ the error in the force is about $500\ N$ whereas the error increases up to $1200\ N$ when the frequency of the disturbance reaches to $4\ Hz$.

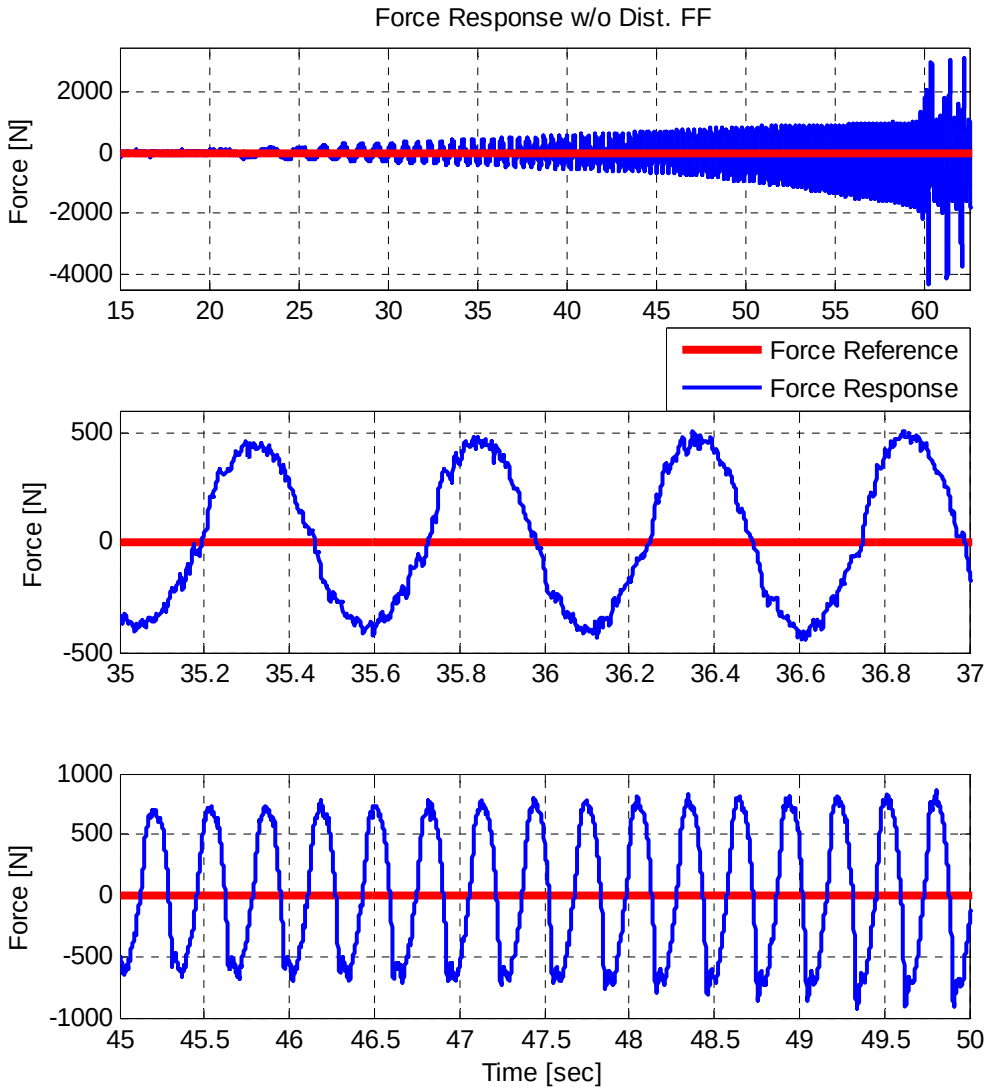

Figure 5-2 Force response when $F_d(s)$ is disabled

It is also observed in the Figure 5-2 that around $t = 60\,s$ the error in the force drastically increases. Note that the maximum velocity of the disturbance is about $219\,mm/s$, when the frequency of x_d is $7\,Hz$. Since the velocity of the disturbance exceeds the maximum retraction velocity of the hydraulic load simulator ($200\,mm/sec$), the saturation of the flow valve occurs at that moment. Therefore, the saturation of the control valve causes this increase in the force error. In addition, the effect of this large force error leads to the deterioration of the position response of the actuator under test as seen in Figure 5-1.

In Figure 5-3, the Bode magnitude diagram between the force error and the applied disturbance motion is given by normalizing it with the equivalent stiffness of the load system, i.e., $F(j\omega)/k_s X_d(j\omega)$. The linearized model responses for extension and retraction cases determined in the previous chapter are also plotted on the same figure.

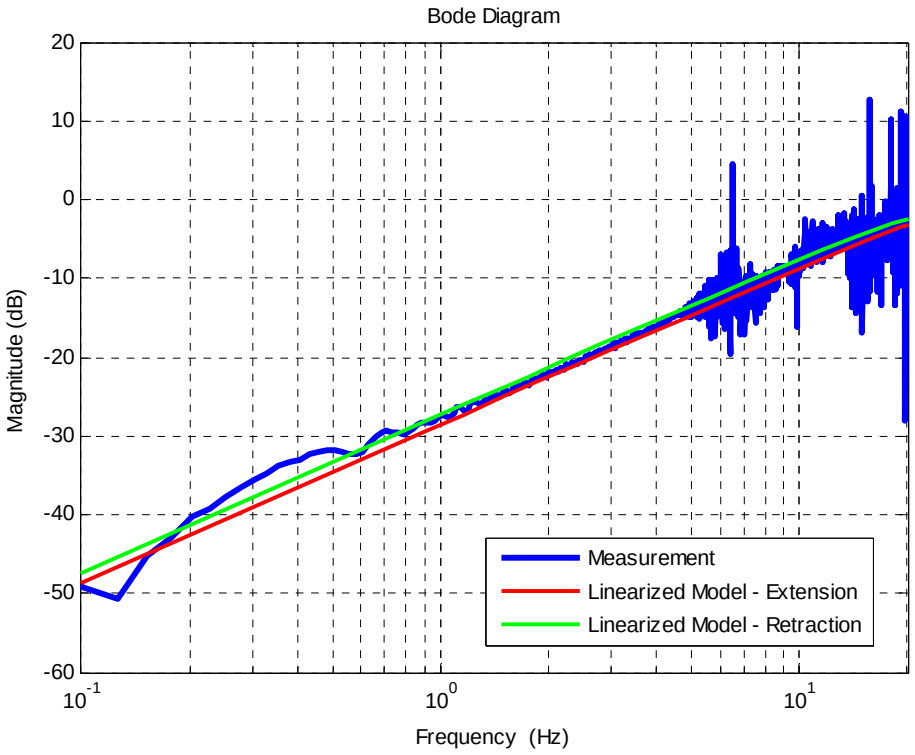

Figure 5-3 Bode magnitude diagram of $F(j\omega)/k_s X_d(j\omega)$when $F_d(s)$ is disabled

In order to show the improvement in the disturbance rejection performance of the load simulator with the use of the feedforward controller, $F_d(s)$, the same chirp signal for the disturbance, x_d, is applied where $F_d(s)$ is enabled. In Figure 5-4, the applied disturbance position x_d and its velocity v_d are shown.

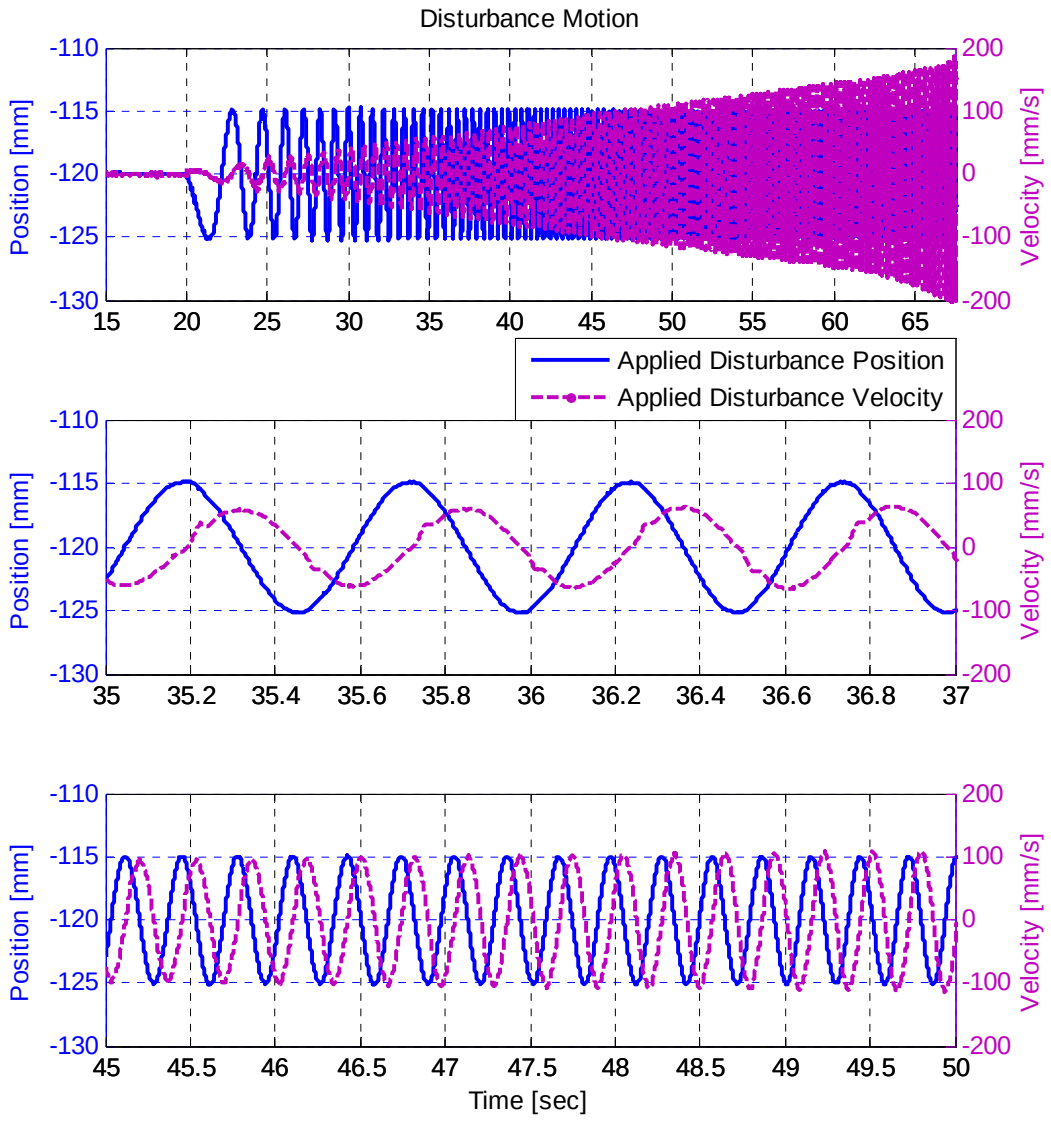

Figure 5-4 Disturbance input applied to the load simulator, x_d, when $F_d(s)$ is enabled

The force response of the electro-hydraulic load simulator as a result of the applied disturbance is given in Figure 5-5, where still a zero reference force is applied. The error is within $100\ N$ when the frequency of the disturbance is about $1.7\ Hz$ whereas it approaches to $200\ N$ as the frequency of the disturbance reaches to $7\ Hz$.

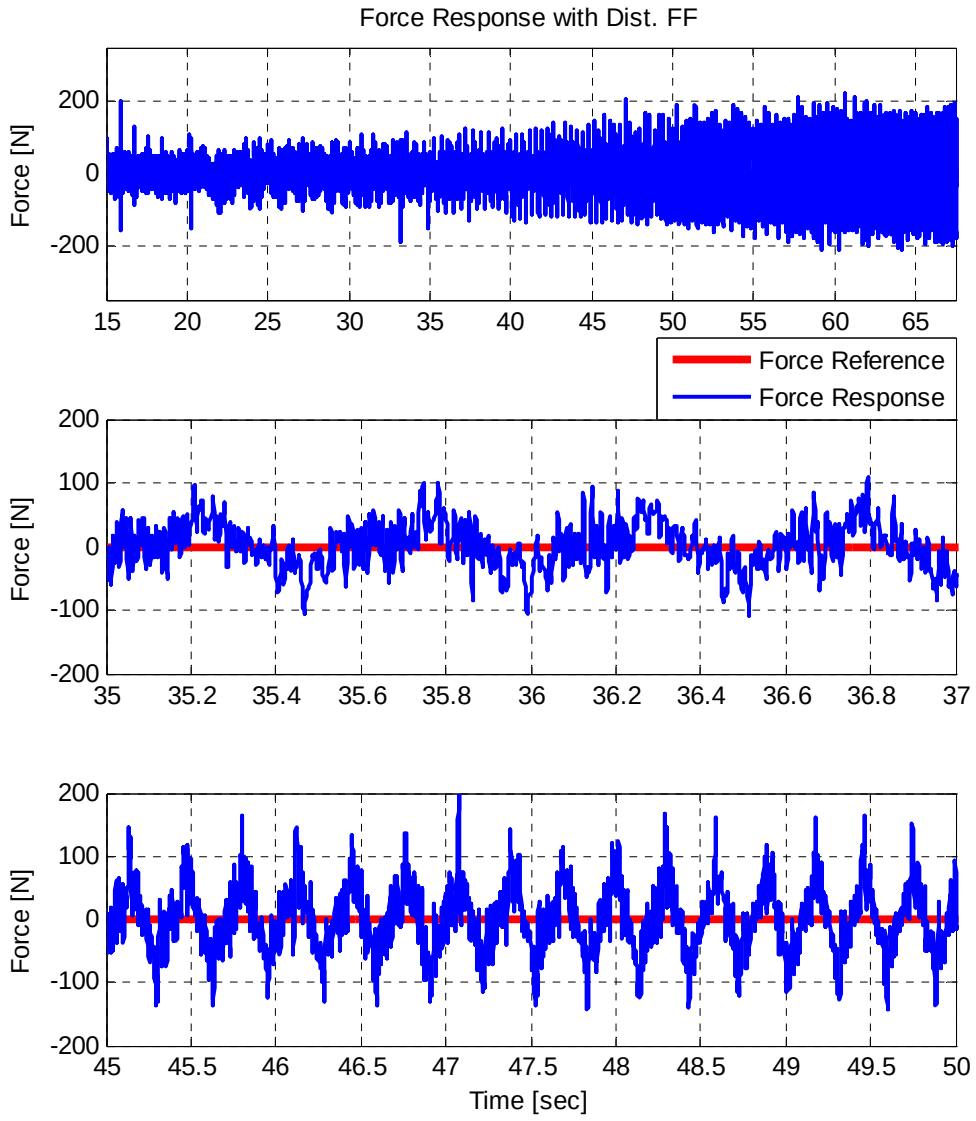

Figure 5-5 Force response when $F_d(s)$ is enabled

The Bode magnitude diagram between the force error and the applied disturbance motion is given in Figure 5-6 by normalizing it with the equivalent stiffness of the load system, i.e., $F(j\omega)/k_s X_d(j\omega)$. The linearized model responses by considering a perfect estimation of the disturbance velocity are also plotted on the same figure. It is seen that although a good improvement is achieved, the result is slightly poorer than the expected performance. Since the linearized models assume that the velocity of the disturbance actuator is perfectly estimated, they result in better disturbance rejection, whereas kinematic Kalman filter provides only an accurate enough estimate of the velocity. In addition, in the low frequency region it is observed that the blue curve becomes constant at about $-53\,dB$, which corresponds to the noisy force reading between $\pm 100\,N$ obtained from the load transducer when the frequency of the disturbance is low, or even zero.

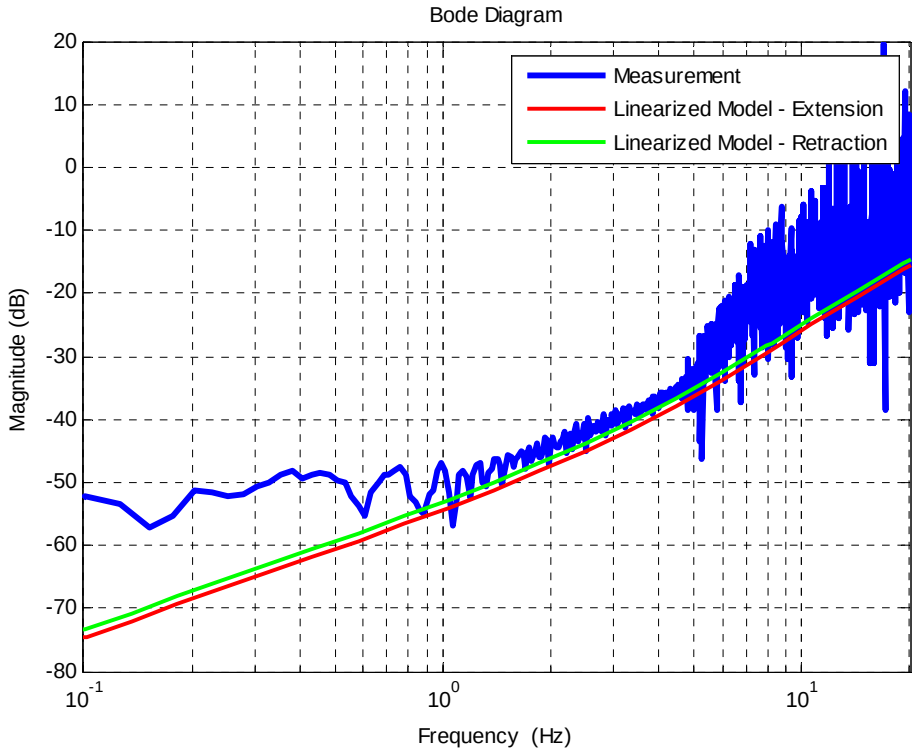

Figure 5-6 Bode magnitude diagram of $F(j\omega)/k_s X_d(j\omega)$when $F_d(s)$ is enabled

The decrease in the force error with the use of the disturbance feedforward controller, $F_d(s)$, is shown in time domain as given in Figure 5-7. In the figure, the results with and without the use of feedforward controller, $F_d(s)$, are plotted together, and the decrease in the error, especially in the high frequency excitations, is clearly seen. Actually, for the applied sinusoidal disturbance input, x_d, with 5 mm magnitude, the error is bounded between $\pm 200\ N$ for the frequencies up to 7 Hz when $F_d(s)$ is enabled.

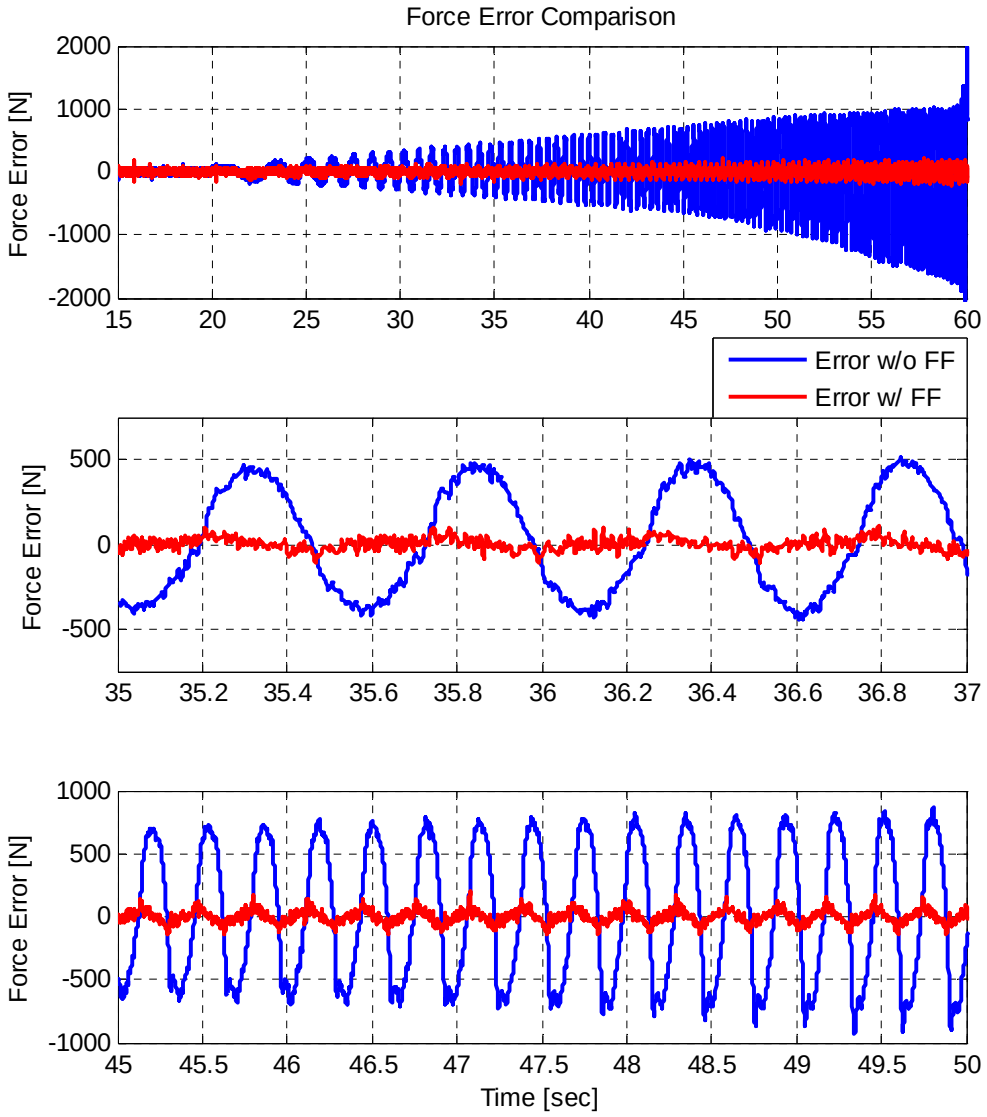

Figure 5-7 Improvement in disturbance rejection performance with the use of $F_d(s)$

In the previous experiments, the reference force for the electro-hydraulic load simulator is set as zero. Since the controller parameters are determined in the previous chapter for null valve coefficients, their validity for other loading conditions should also be evaluated. Now, the same tests will be performed for a reference force of $F_{ref} = 5000\ N$ and when the feedforward controller $F_d(s)$ is enabled. Figure 5-8

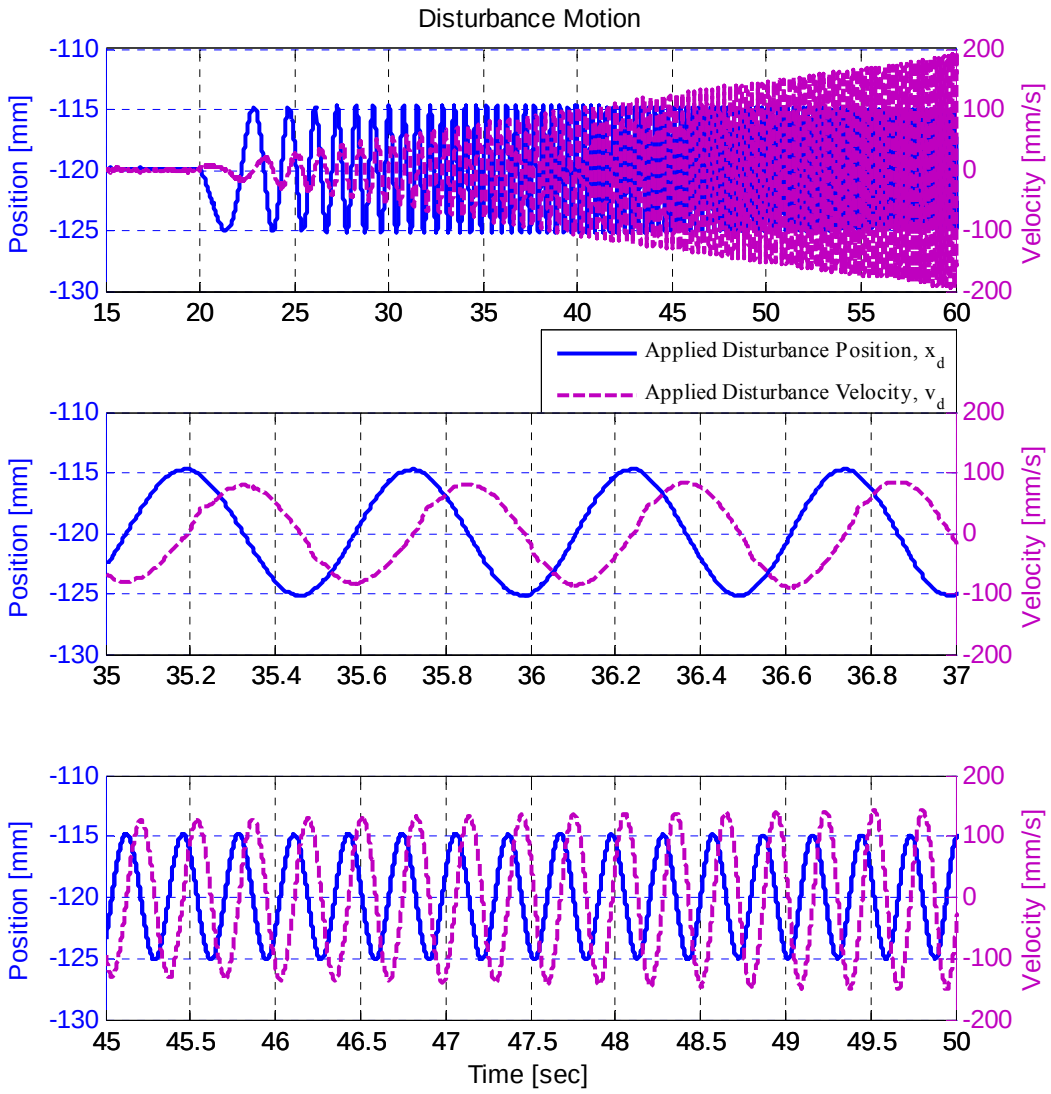

Figure 5-8 Disturbance input applied to the load simulator, x_d, when $F_d(s)$ is enabled and $F_{ref} = 5000\ N$

illustrates the disturbance motion (x_d and v_d)applied to the load simulator. In Figure 5-9, the response of the load simulator is given. It is seen that only a slight increase compared to previous experiments is observed in the force error. Hence, the error is between $-260\ N$ and $200\ N$ for the same disturbance.

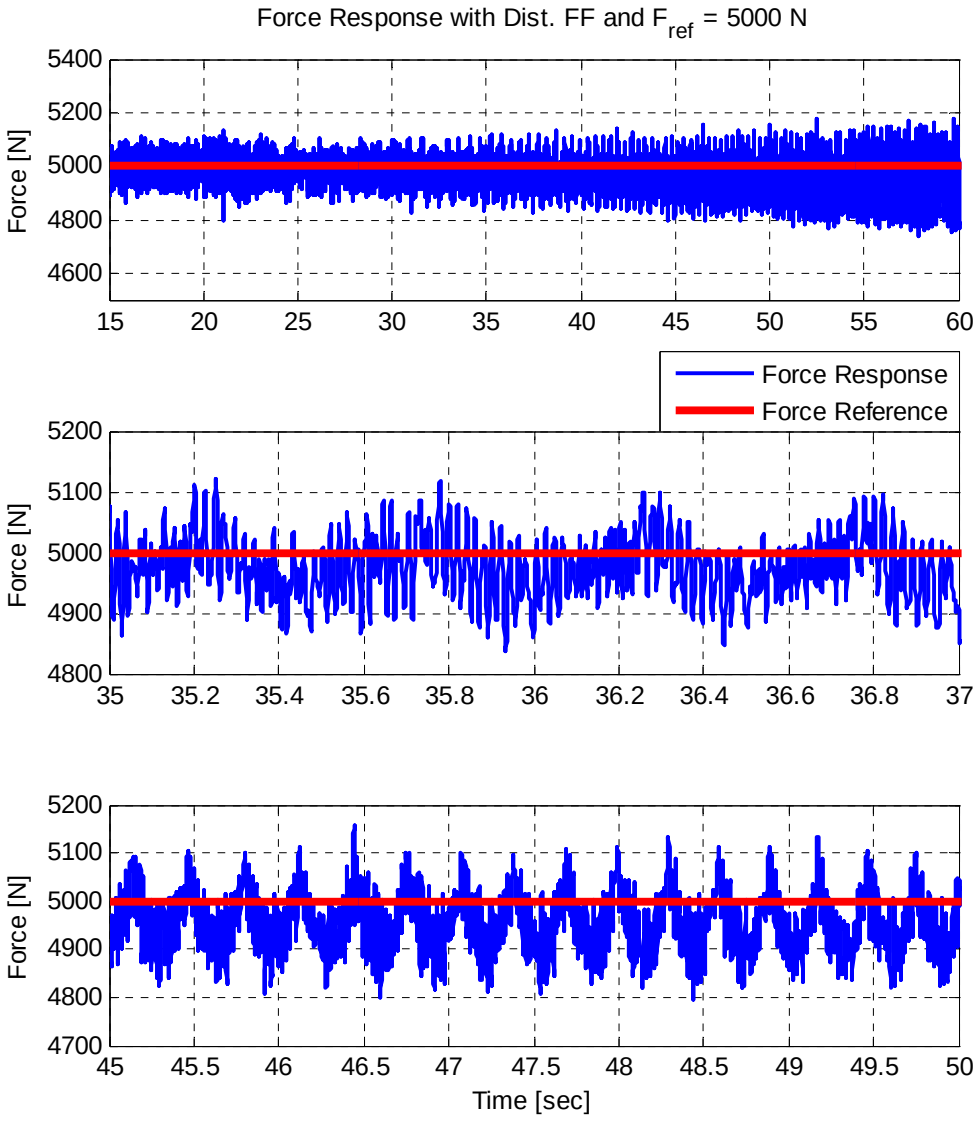

Figure 5-9 Force response when $F_d(s)$ is enabled and $F_{ref} = 5000\ N$

5.2 Force Tracking Performance

In this section, the force tracking performance of the electro-hydraulic load simulator is evaluated by applying a sinusoidal force onto the actuator of the hydraulic drive system under test. In all of the following experiments, the disturbance feedforward controller, $F_d(s)$, is enabled in order to reject the disturbance motion, x_d, of the actuator under test as response to the applied forces. In Figure 5-10, the

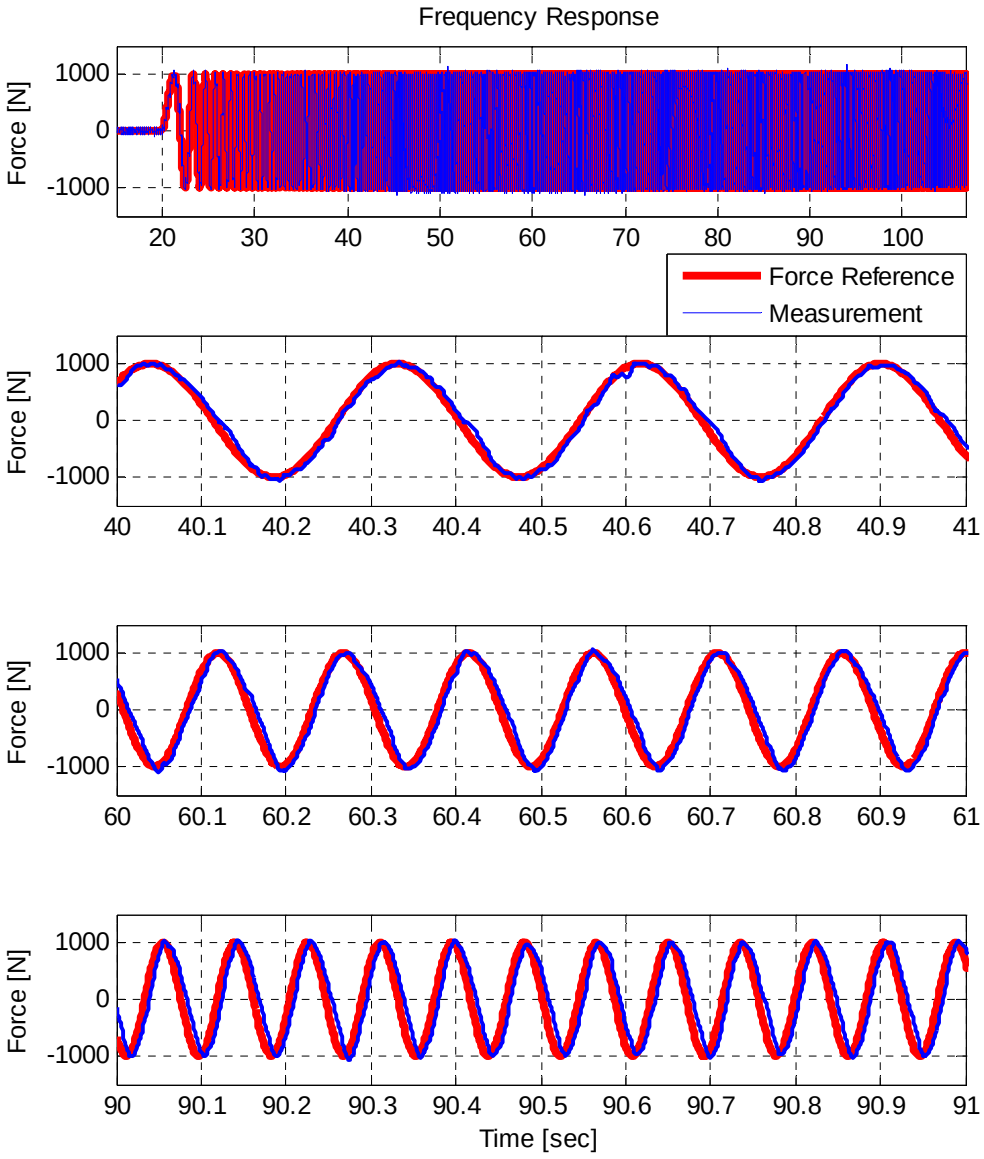

Figure 5-10 Force tracking performance when F_u(s) is disabled

reference force input to the hydraulic load simulator and its response are given. A chirp signal with frequency ranging from $0.1\,Hz$ to $15\,Hz$ with a magnitude of $1000\,N$ is used as the reference input. Initially, the reference, or set-point, feedforward controller, $F_u(s)$ is disabled. In Figure 5-11, the Bode

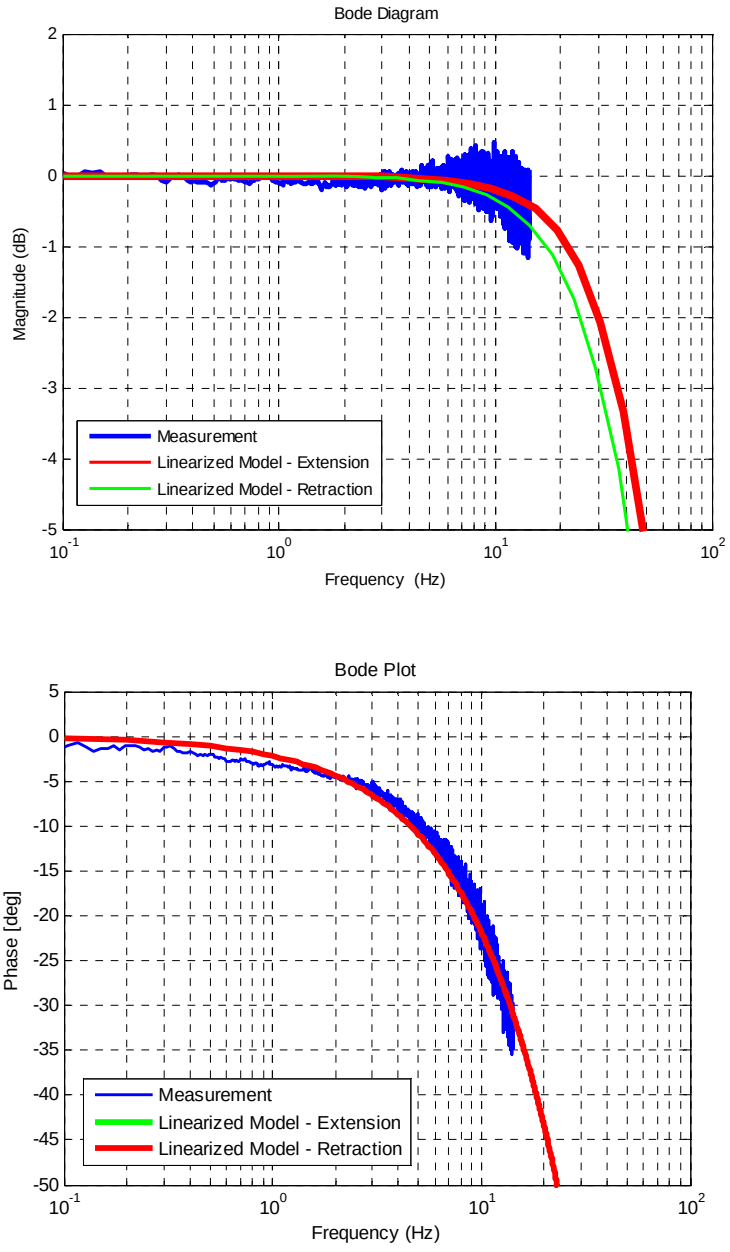

Figure 5-11 Bode diagrams of $F(j\omega)/F_{ref}(j\omega)$ when $F_u(s)$ is disabled

magnitude and phase diagrams of the force controlled system are given. The linear model responses are also plotted on the figures and they accurately predict the closed-loop system response. It is seen in the magnitude curve that the closed-loop system satisfies the 1 dB magnitude requirement of the dual ten criteria. On the other hand, 10^{o} phase lag requirement is only satisfied up to about 5 Hz, as expected by the linear models. Although the magnitude of the response clearly follows the reference as seen in Figure 5-10, the increased phase lag with increasing frequency of the reference signal leads to an increased instantaneous force error as indicated in Figure 5-12.

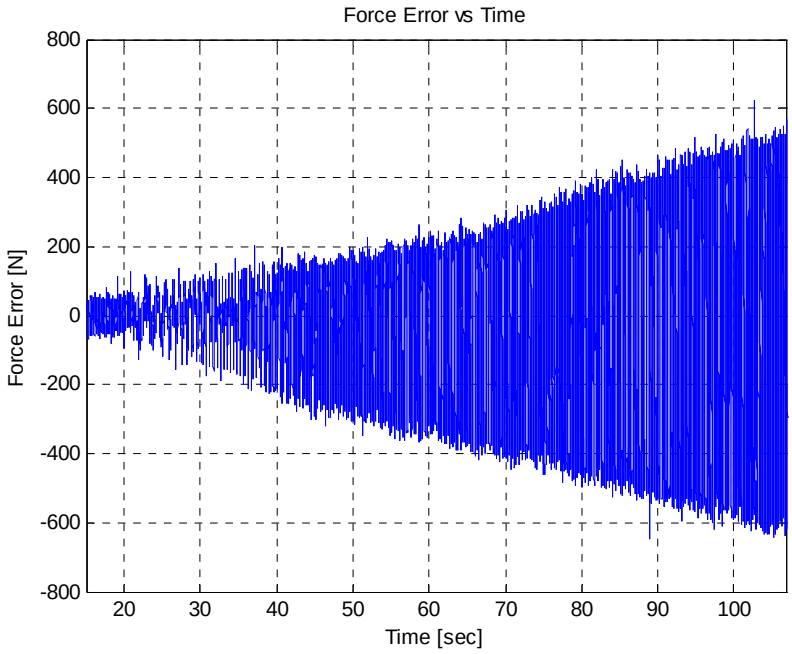

Figure 5-12 Instantaneous force error when $F_u(s)$ is disabled

In order to decrease the phase lag of the closed-loop system to the reference signals, the reference feedforward controller, $F_u(s)$, is enabled. The response of the system to the same sinusoidal reference input is given in Figure 5-13.

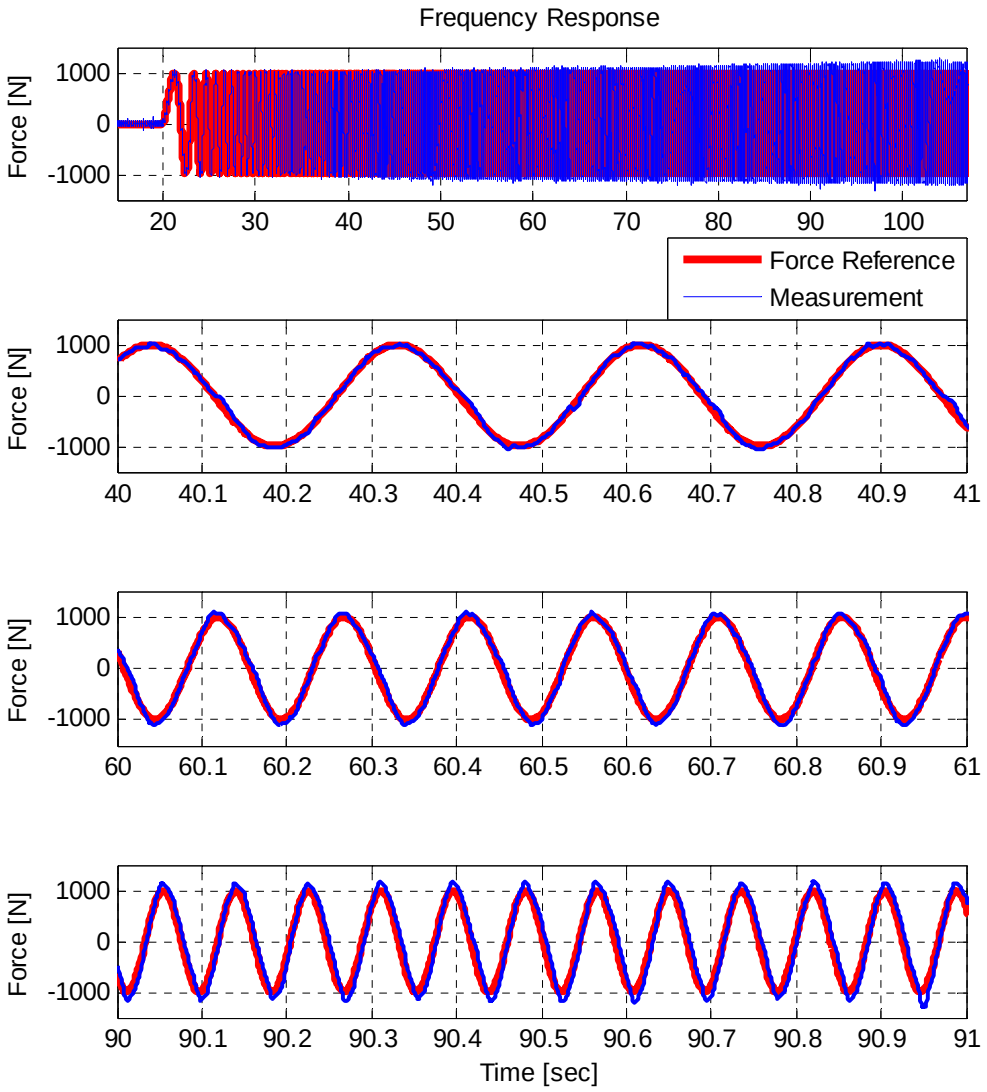

Figure 5-13 Force tracking performance when $F_u(s)$ is enabled

In Figure 5-14, the Bode magnitude and phase diagrams of the closed-loop system are given. The linearized model responses are also illustrated on the same figures. It is seen in the magnitude plot that as the frequency of the excitation increases the magnitude of the response also increases around 10 Hz. Although the expected value at 10 Hz is about 0.35 dB, the test results yield to a value of about 0.7 dB. However, since it is still less than 1 dB satisfying the magnitude requirement of dual-ten index, it is quite acceptable.

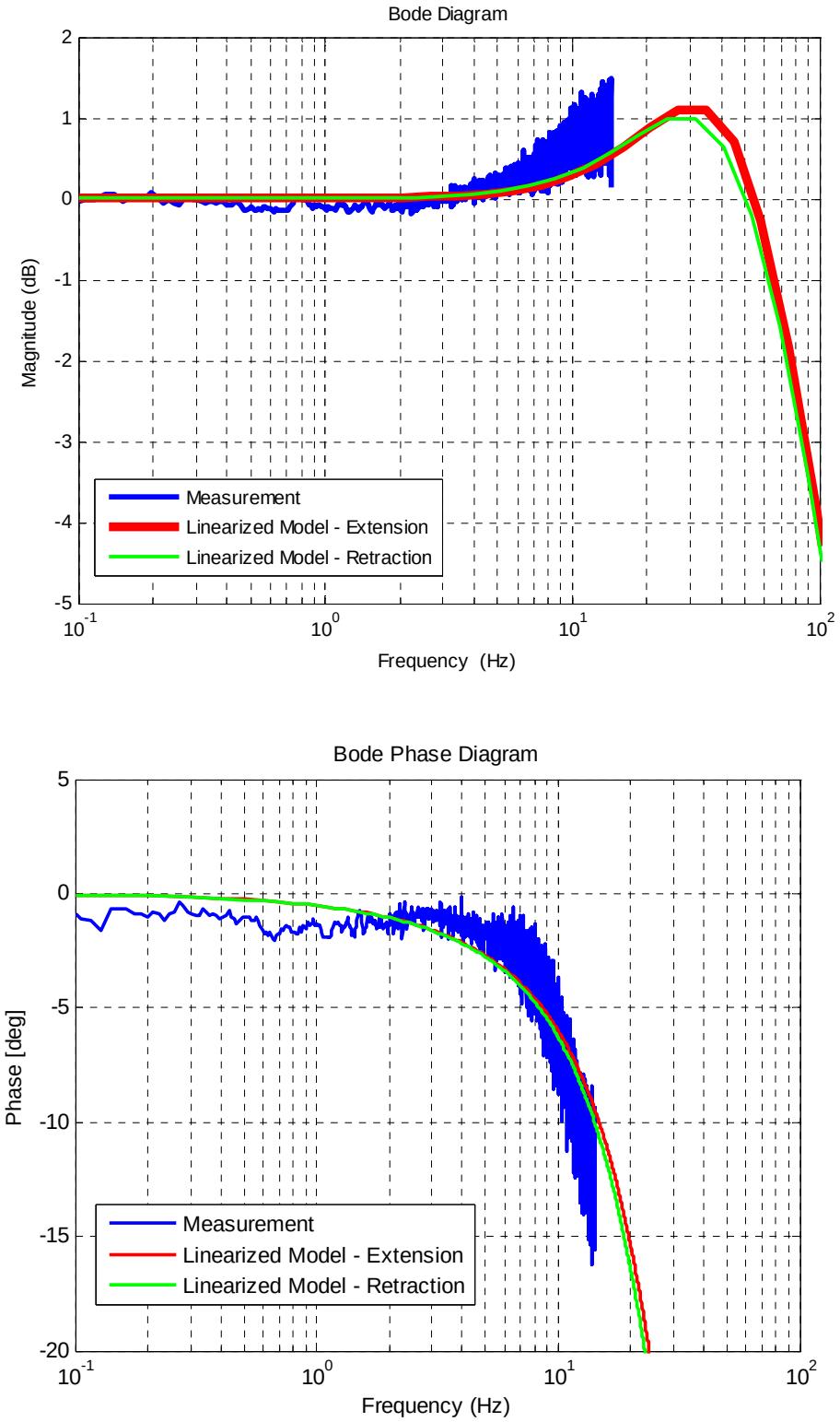

Figure 5-14 Bode diagrams, $F(j\omega)/F_{ref}(j\omega)$ when $F_u(s)$ is enabled

With the use of the feedforward controller $F_u(s)$, the phase lag of the system is considerably decreased to the value of about -6^o, and hence, it satisfies the 10^o phase lag requirement of the dual-ten index. While the dual-ten requirements are satisfied, the decrease in the instantaneous force error is illustrated in Figure 5-15.

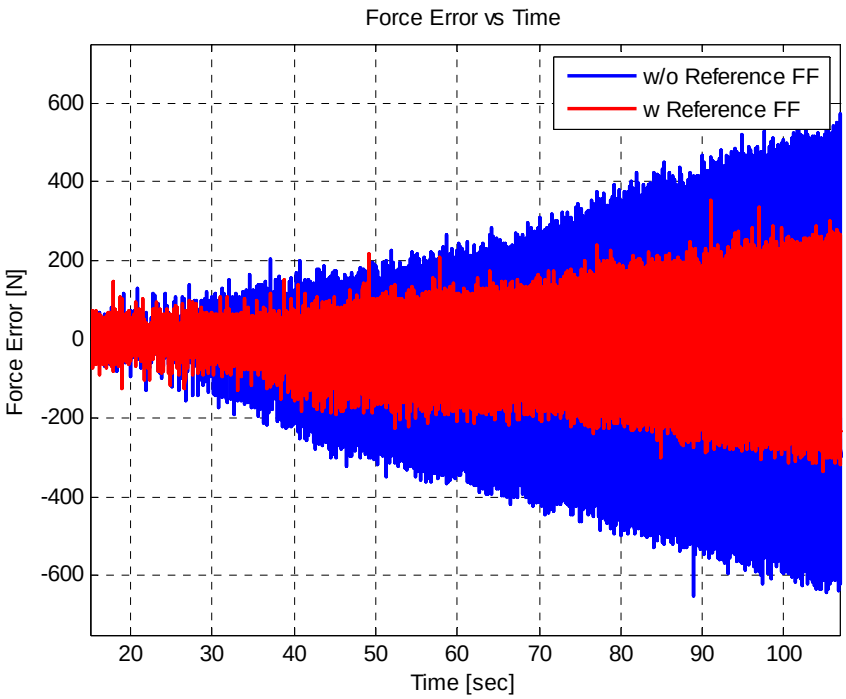

Figure 5-15 Decrease in the instantaneous force error with the use of $F_u(s)$

5.3 Loading Limits of the Electro-Hydraulic Load Simulator

In the previous section, the force tracking performance of the electro-hydraulic load simulator is indicated by performing a frequency sweep test ranging from $0.1\ Hz$ to $15\ Hz$ with a magnitude of $1000\ N$. In this section, the saturation limits of the hydraulic system of the load simulator are investigated by applying some sinusoidal test inputs of higher magnitudes, and the results are compared with the non-linear simulation results.

A sinusoidal reference force input with a magnitude of 3000 N and a frequency of 5 Hz is applied to the electro-hydraulic load simulator. The reference input and the response of the hydraulic load simulator are given together with the simulation results in Figure 5-16. A Fourier analysis of the experimental data shows that the magnitude ratio and phase lag at this frequency are 0.26 dB and -2.1^{o}, respectively.

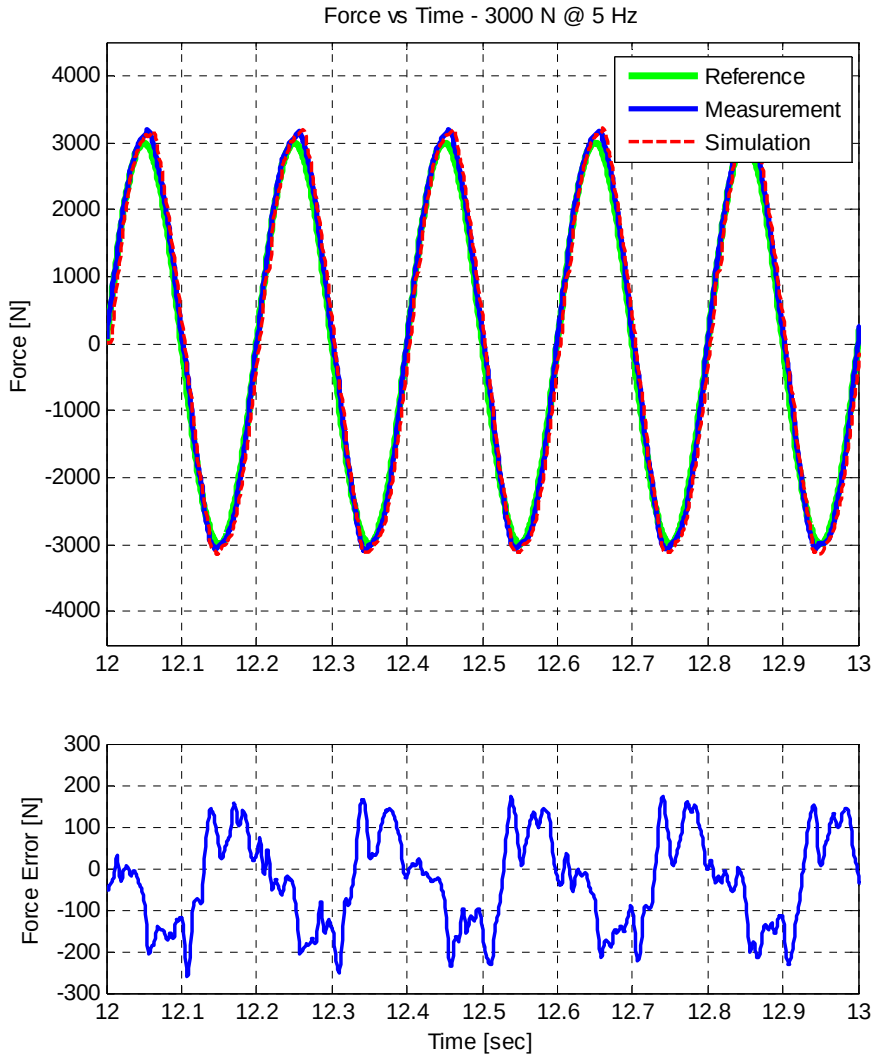

Figure 5-16 Force response at 3000 N and 5 Hz

The velocity responses of the actuators of the load simulator and the hydraulic drive system under test are given in Figure 5-17. Although a constant position reference input is applied for the actuator of the hydraulic drive system under test, it is seen that the velocity of this actuator reaches up to $100\ mm/sec$ with the application of the reference force by the load simulator. Thanks to the disturbance feedforward controller, the effect of the disturbance motion is considerably attenuated, and a smooth force output is obtained as seen in Figure 5-16. Therefore, the estimated velocity of the test actuator during the tests is also provided to the non-linear simulation model as input in addition to the sinusoidal force reference input.

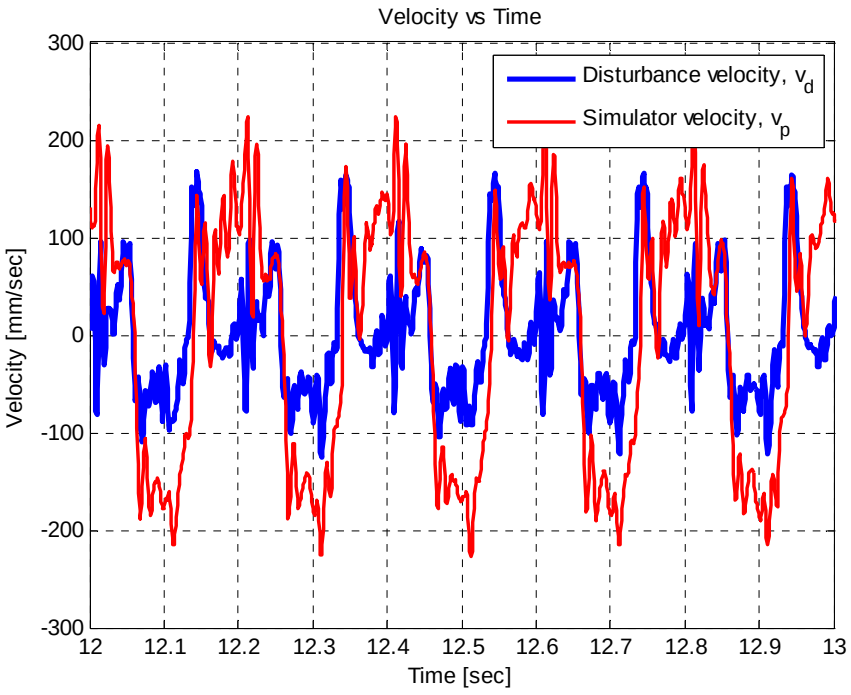

Figure 5-17 Actuator velocities at $3000\ N$ and $5\ Hz$

The spool feedback obtained through the test is compared with the simulation results in Figure 5-18. As seen in Figure 5-16 and Figure 5-18, the non-linear simulation results closely predict the force and spool position measurements obtained from the load simulator. Hence, the non-linear simulation model of the electro-hydraulic load

simulator can be utilized as an offline tool to predict the experimental test results if an accurate enough dynamic model of the test system is available.

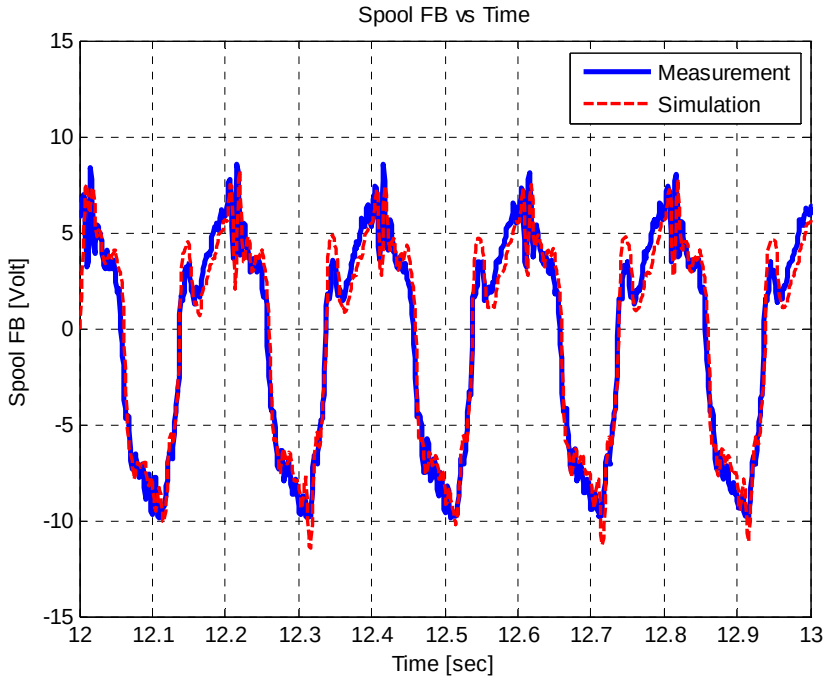

Figure 5-18 Spool position feedback at 3000 N and 5 Hz

The results of this test clearly indicate the loading limits given in Figure 2-8. In the figure, it is shown that if the velocity of the disturbance actuator reaches to 100 mm/s, the loading condition of 2500 N at 5 Hz, which is green load locus curve in Figure 2-8, is very close to the saturation curve of the proportional control valve (purple curve). As a result, as expected from Figure 2-8, the valve input signal is just about to saturate in Figure 5-18 since the disturbance velocity approaches to, or even exceeds 100 mm/s as seen in Figure 5-17.

The same tests are also performed for different sinusoidal inputs and again compared with non-linear simulation results. In Figure 5-19, the response of the system to a sinusoidal reference force input of 7500 N at 1 Hz is given. In addition, the

estimated velocities of the actuators of the load simulator and the hydraulic drive system under test are given in Figure 5-20.

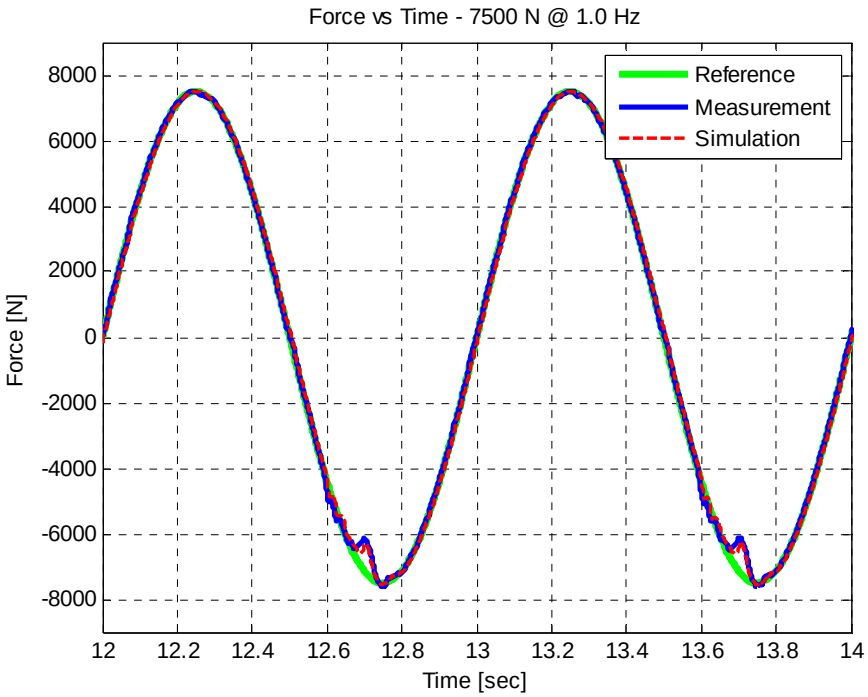

Figure 5-19 Force response at 7500 N and 1 Hz

Similarly, the disturbance velocity of the actuator under test is given as input to the non-linear simulation model. In Figure 5-21, the spool position feedback obtained through the measurements and simulation results are illustrated. The saturation of the hydraulic system is clearly observed in the figure. The instants at which the saturation of the hydraulic actuator of the load simulator occurs as in Figure 5-21 are due to the high velocity of the disturbance actuator as seen in Figure 5-20. The disturbance velocity even exceeds the maximum steady state velocity of the actuator at some instants. Therefore, the disruption in the force tracking exactly at the saturation instants is clearly observed in the force response given in Figure 5-19.

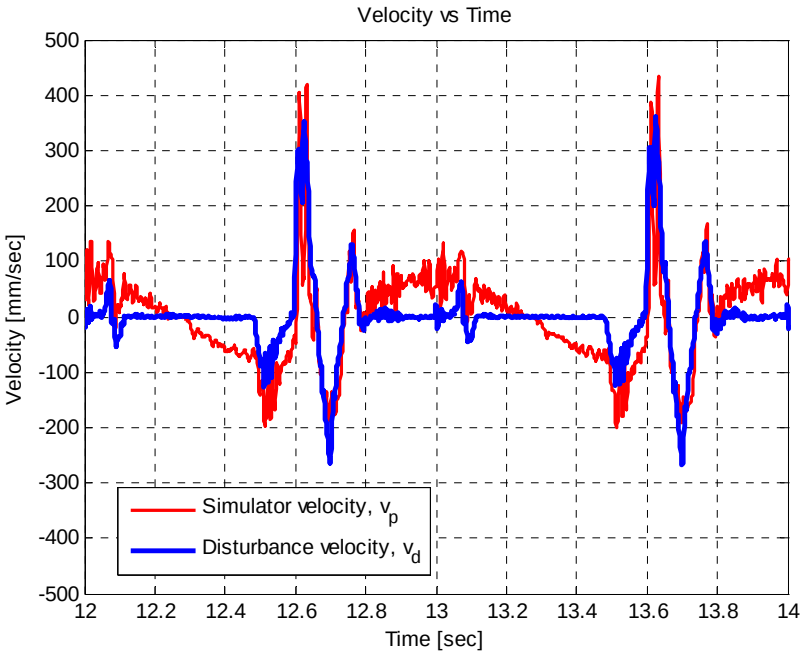

Figure 5-20 Actuator velocities at 7500 N and 1 Hz

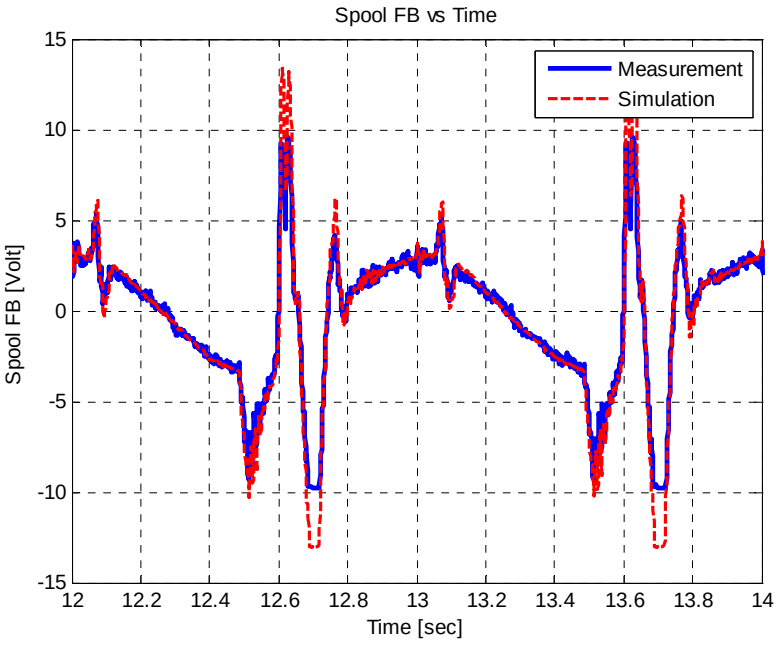

Figure 5-21 Spool position feedback at 7500 N and 1 Hz

Hence, it is crucial to perform the tests on the load simulator test bench within its limits in order to get satisfactory results without saturation. Furthermore, the effectiveness of the simulation model in approaching the actual test results is shown once again, and its use before the actual tests is emphasized again.

The same test is performed for the sinusoidal force reference input of 10 kN at 1 Hz. Knowing that the actuator under test has a highly low dynamic stiffness and exhibits large deflections at these loads, the saturation of the loading system is still expected. However, in order to provide an example loading at relatively large forces, the response of the system to 10 kN at 1 Hz sinusoidal input is given in Figure 5-22.

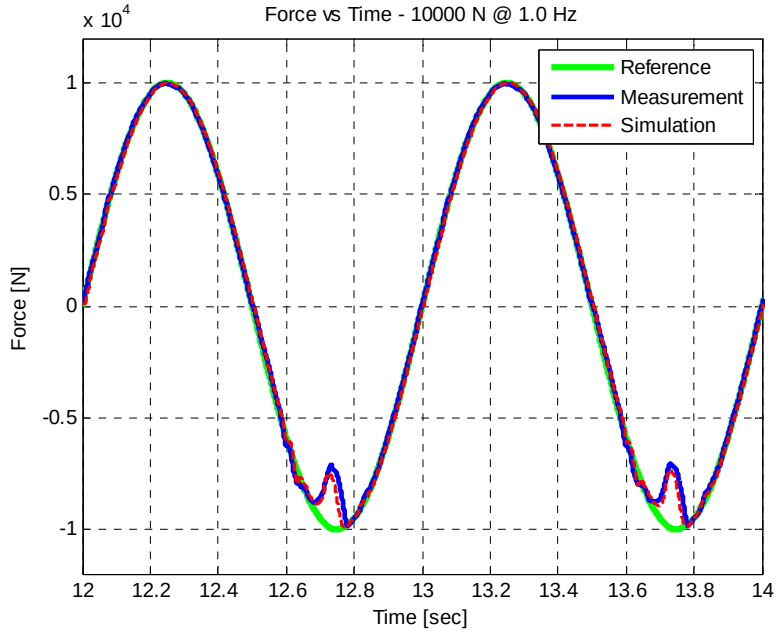

Figure 5-22 Force response at 10 kN and 1 Hz

The estimated velocities of the actuators during experimental test are given in Figure 5-23. It is clearly seen that the velocity of the disturbance actuator exceeds 200 mm/s, which is the maximum steady state velocity of the loading actuator. The spool feedback measurement is compared with simulation results in Figure 5-24.

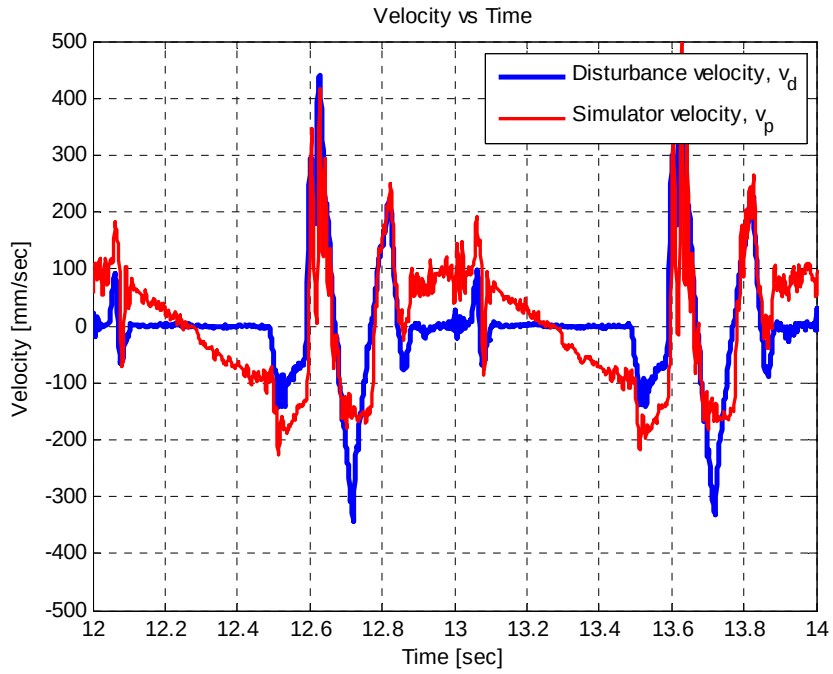

Figure 5-23 Actuator velocities at 10 kN and 1 Hz

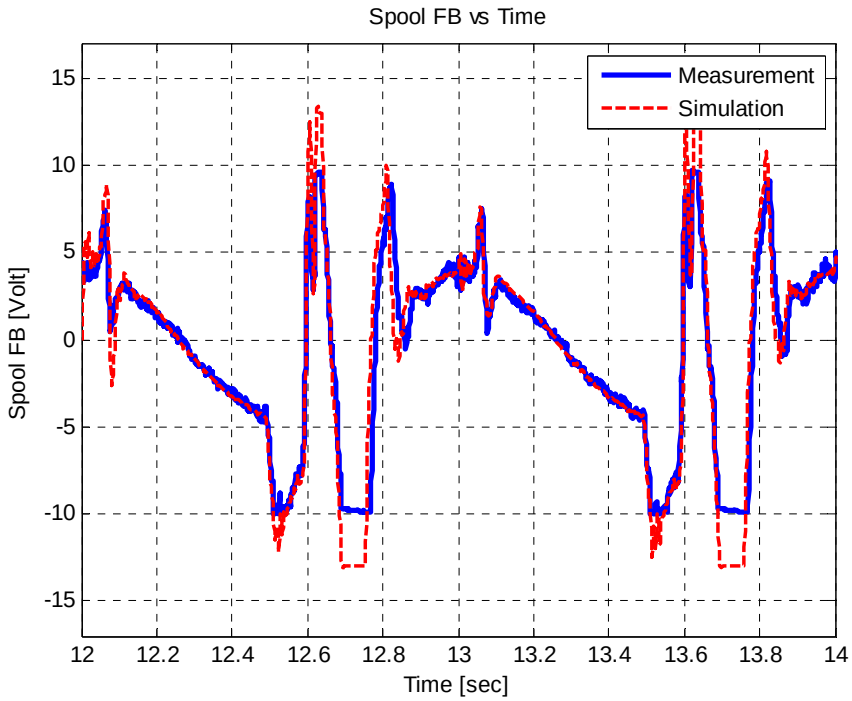

Figure 5-24 Spool position feedback at 10 kN and 1 Hz

The model accurately estimated the force and spool position responses. The large force errors at saturation instants are also estimated accurately by the simulation results as in Figure 5-22.

The loading capacity of the simulator is summarized in Figure 2-8 and Figure 2-9 with the selected components to fulfill the given requirements. In this section, a number of reference force inputs at different magnitudes and frequencies are applied to the electro-hydraulic load simulator to show that the requirements are satisfied. The spool position feedback of the flow control valve is taken and its saturation instants are observed. It is clearly shown by the experimental results that the simulator satisfies the requirements. To illustrate, the test with a reference force input of $3000\ N$ at $5\ Hz$ shows that this reference input can be applied if the velocity of the disturbance actuator is less than $100\ mm/s$ and the saturation of the flow control valve is observed when this velocity is exceeded. In addition, the experimental results are compared with the non-linear simulation results and the validity of the simulation model is clearly indicated. Therefore, the limits of the simulator summarized in Table 2-2 and Table 2-3 are validated and the simulation model is proposed as an offline tool to predict the test results before performing them on the load simulator.

CHAPTER 6

SUMMARY, CONCLUSION AND FUTURE WORK

6.1 Summary and Conclusion

In this thesis, an electro-hydraulic load simulator is designed and constructed as an experimental loading unit in order to carry out the performance and stability tests of newly developed hydraulic drive and control systems in controlled laboratory conditions. Therefore, by designing such a test system, it is aimed to eliminate the strong need to the actual plant to be readily built, or available so as to perform the necessary tests, and hence to facilitate these research activities in a highly cost and time effective way.

The design of the electro-hydraulic load simulator mainly includes the development of a valve-controlled hydraulic loading unit, the instrumentation of the loading unit with necessary feedback transducers and a real-time control computer, and the design and implementation of a force control algorithm. A test bench, or stand, is also designed and constructed within the scope of this study in order to accommodate the actuators of the load simulator and the hydraulic drive system under test. In this thesis, the overall design process is presented in detail.

The valve-controlled hydraulic loading system is initially developed to satisfy the given dynamic loading requirements. The selection and use of the components of the hydraulic loading system are explained in detail. Since the hydraulic load simulator is *a series elastic actuator* to be used in a closed-loop force control application, a compliant spring load system is also designed in order to reduce the output

impedance of the system. So as to determine the stiffness of the load system, an analysis of the load is performed by considering the saturation limit of the proportional control valve, and the dynamic loading limits of the simulator are indicated. Moreover, the hydraulic power pack providing the required power at constant pressure for the operation of the proportional control valve is explained with all its components.

The hydraulic load simulator is instrumented with a number of transducers, namely, a force transducer, two pressure transducers for each chambers of the hydraulic actuator, and a position transducer. The force transducer provides the feedback for the controlled variable to be used in the closed-loop control. Additionally, an incremental encoder is used to measure the actuator position of the hydraulic drive system under test, and its output is also used by the force control system. A real-time control computer with its various input and output modules is setup as the DAQ system and the real-time control computer.

The construction of the test bench to accommodate the actuators of the hydraulic load simulator and the hydraulic drive system under test is briefly explained in this study. It is specifically aimed to test a variable speed pump controlled hydraulic drive system with a single rod hydraulic actuator. Therefore, the design of the test bench is performed according to the dimensions of the actuator to be tested. The solid model of the test bench is created by using SolidWorks 2010. The closed frame design of the test bench results in a compact and easily transportable structure without allowing the created forces to be transferred to its environment.

A non-linear mathematical model of the electro-hydraulic load simulator is obtained with the purpose of control system design and analysis, and a numerical simulation model is constructed by using MATLAB®/Simulink®. Most of the model parameters are determined from the technical drawings and/or catalogs of the manufacturers of the components. However, the friction characteristic of the hydraulic actuator is determined by performing open-loop tests, and the bulk modulus of the hydraulic fluid is obtained from the literature. The validity of the model with these parameters

is shown by performing open-loop experiments and comparing them with simulation results.

The validated mathematical model is linearized around a critical operating point, and the continuous time transfer functions of the system are obtained. By utilizing these transfer functions, a combined feedforward and feedback force controller, and a velocity feedforward controller to reject the disturbance motion of the system under test are designed. It is aimed to achieve an enhanced dynamic performance and stability with a proportional closed-loop controller whereas the dynamic errors are diminished thanks to the reference and disturbance feedforward controllers.

In addition, a Kalman filter with a kinematic model is designed in order to estimate the actuator velocity of the hydraulic drive system under test since only its position is measured with an incremental encoder. The implementation and tuning of the filter are explained. The estimation results are compared with the ones obtained via finite difference equations, and it is concluded that the KKF provides smooth velocity estimation, especially in low velocities. Hence, it is used in the disturbance feedforward controller. Although the KKF provides an estimate of the acceleration, it is observed that its use in the controller causes chattering of the control valve. Hence, the acceleration estimation is not as smooth as the velocity estimate.

The performance of the electro-hydraulic load simulator is evaluated by performing real-time experiments and comparing them with model responses. The disturbance rejection performance of the system is evaluated under the influence of a sinusoidal disturbance motion of the hydraulic actuator under test. The method is highly powerful since the development of large force errors in the force control loop is prevented by synchronizing the velocity of load simulator with that of the disturbance actuator. The force tracking performance of the load simulator is evaluated by applying a sinusoidal force onto the actuator under test. The improvement in the force tracking performance and the resulting decrease in the instantaneous force error with the use of the reference feedforward controller are also shown.

The saturation limits of the electro-hydraulic load simulator are investigated by applying some sinusoidal force inputs of different magnitudes and frequencies. It is concluded that the design requirements stated in Chapter 2.1 are satisfied. The experimental results are compared with the non-linear simulation results and it is also proposed that the non-linear simulation model can be utilized as an offline test platform before performing the real-time experiments.

To conclude, the whole design process of the electro-hydraulic load simulator is presented and the dynamic loading limits of the simulator are clearly indicated in this study. It is currently being used for the testing of a variable speed pump controlled hydraulic drive system. Since its limits are well-defined, similar systems can also be tested by using the simulator. Therefore, the load simulator is a convenient testing platform for the research activities related to the development of new drive and control systems as its use shortens the development period and saves the research funds.

6.2 Future Work

In this study, a differential hydraulic actuator is used as the actuator of the electro-hydraulic load simulator since it is readily available for use. Although differential actuators are preferred because of their compact structures, they exhibit some important drawbacks due to their inherent nonlinearity. Since the DC gains of the actuator in extension and retraction cases are different, the feedforward controllers are separately designed in this study. Even though the feedforward controller gains are switched during tests depending on the sign of the spool position, a constant feedback gain is preferred since gain switching in feedback loop may cause stability problems. Hence, a gain scheduling method or a feedback linearizing controller can be utilized to further diminish the effect actuator nonlinearity.

Another drawback of the differential actuator is that since the maximum achievable forces and velocities in each direction of the actuator motion are different from each

other, the performance of the simulator in each direction is different. That is, the maximum achievable velocity and the maximum force that can be applied are limited by the rod side of the actuator. Therefore, the specifications of the hydraulic system are given for this chamber of the actuator. Therefore, a double-rod hydraulic actuator can be selected to have symmetrical performance.

An important use of the load simulators is observed in hardware-in-the-loop simulations and tests. In these applications, a physical simulation model of the plant is constructed and the forces determined by the real-time solution of this model are applied to the actuator under test by the load simulator. In this study, the controller of the hydraulic load simulator is implemented by using MATLAB®/Simulink® in an xPC target machine, and the used software and hardware provide the HIL simulations by their real-time capabilities.

Besides the development of new hydraulic drive and control systems, the test bench can also be utilized to evaluate the performance of newly developed force control algorithms. Therefore, the research activities related to the active suspension systems, injection molding machines, and etc. can also be carried out with the electro-hydraulic load simulator designed and constructed in this study.

To improve the disturbance rejection performance of the system, an accelerometer can be utilized so that both the compensation related to the acceleration of the actuator is included to the control signal, and also the accuracy of the velocity estimation obtained by kinematic Kalman filter can be improved.

In this study, a number of simple buttons and switches are utilized in Simulink® model to control the load simulator. However, a graphical user interface (GUI) can be developed in order to provide the user with the required options to select and modify the tests more practically. In addition, the GUI can provide a mean for formatting and displaying the test results, which can also be adjusted through the GUI options.

REFERENCES

[1] Mavroidis, C., Pfeiffer, C., Mosley, M., "Conventional actuators, shape memory alloys, and electrorheological fluids", Invited Chapter in *Automation, Miniature Robotics and Sensors for Non-Destructive Testing and Evaluations*, Y. Bar-Cohen Edition, The American Society for Nondestructive Testing, April 1999.

[2] Mayr, O., *Origins of Feedback Control*, Cambridge: MIT Press, 1970.

[3] Maskrey, R. H., Thayer, W. J., "A brief history of electrohydraulic servomechanisms", *Journal of Dynamic Systems, Measurement, and Control*, vol. 100, pp. 110-116, June 1978.

[4] Zheng, C., Le Duigou, J., Bricogne, M., Eynard, B., "Survey of design process models for mechatronic systems engineering", *Proceedings of 10th International Congress of Industrial Engineers (CIGI 2013)*, La Rochelle, 2013. Retrieved from http://cigi13.eigsi.fr/Documents/Articles/MI1/cigi2013_submission_38.pdf, last viewed on 26.01.2014.

[5] Brezina, T., Singule, V., Hadas, Z., "Model based design of mechatronic systems at BRNO University of Technology", *Proceeding of the 2nd International Scientific and Practical Conference: Modern Engineering, Education and Science*, St. Petersburg, Russia, pp. 197-206, 2012. Retrieved from http://www.mmf.spbstu.ru/mese/2012/197-206.pdf, last viewed on 30.12.2013.

[6] Albayrak, O., "Modelling and real-time control system implementation for a Stewart platform", M.Sc. thesis, Department of Mechanical Engineering, METU, Ankara, Turkey, 2006.

[7] Rito, D. G., Denti, E., Galato, R., "Robust force control in a hydraulic workbench for flight actuators", *Proceedings of the 2006 IEEE Conference on Computer Aided Control Systems Design*, Munich, Germany, pp. 807-813, 04-06 October 2006.

[8] Platin, B. E, Çalışkan, M., Özgüven, H. N., *Dynamics of Engineering Systems*, METU, Ankara, Turkey, 1988.

[9] Smith, M. J., Byington, C. S., Watson, M. J., Bharadwaj, S., Swerdon, G., Goebel, K., Balaban, E., "Experimental and analytical development of health management for electro-mechanical actuators", *Proceedings of IEEE Aerospace Conference*, Big Sky, MT, USA, pp. 1-14, 07-14 March 2009.

[10] Lamming, C., Plummer, A., Hillis, A., Robust electrohydraulic force control, The Centre for Power Transmission and Motion Control, Department of Mechanical Engineering, University of Bath, Bath, UK. Retrieved from http://www.bath.ac.uk/mech-eng/files/ptmc/ca-robust-electro.pdf, last viewed on 12.01.2014.

[11] Li, J., Shao, J., Han, G., Wang, Z., Wu, B., "Study of the Electro-hydraulic Load Simulator Based on Flow-Press Servo Valve and Flow Servo Valve Parallel Control", *Proceedings of 2009 International Conference on Intelligent Human-Machine Systems and Cybernetics*, vol. 2, Hangzhou, Zhejiang, China, pp. 70-74, 26-27 August 2009.

[12] Kim, J. W., Xuan, D. J., Zang, J. I., Nan, Y. H., Kim, Y. B., "The force control system design of road simulator using QFT", *Proceedings of International Conference on Control, Automation and Systems*, Seoul, Korea, pp. 1634-1638, 17-20 October 2007.

[13] Karpenko, M., Sepehri, N., "Hardware-in-the-loop simulator for research on fault tolerant control of electrohydraulic actuators in a flight control application", *Mechatronics*, vol. 19, issue 7, pp. 1067-1077, October 2009.

[14] Isermann, R., Schaffnit, J., Sinsel, S., "Hardware–in-the-loop simulation for the design and testing of engine control systems", *Control Engineering Practice*, vol. 7, issue 5, pp. 643-653, May 1999.

[15] Signorelli, C. D., Villegas, C. Ringwood, J. V., "Hardware-in-the-loop simulation of heaving wave energy converter", *Proceedings of the 9th European Wave and Tidal Energy Conference (EWTEC)*, Southampton, UK, 5-9 September 2011.

[16] Çalışkan, H., Akova, H. U., Balkan, T., Platin, B. E., "Electro-hydraulic lift system with single acting actuator", *Proceedings of the 8th International Conference on Fluid power Transmission and Control (ICFP 2013)*, Hangzhou, China, pp. 139-143, 9-11 April 2013.

[17] Akova, H. U., Çalışkan, H., Balkan, T., Platin, B. E., "Elektrohidrolik abkant pres tasarımı – I: modelleme ve benzetim", *Proceedings of the 15th National Automatic Control Conference*, Malatya, Turkey, pp.745-750, 26-28 September 2013.

[18] Çalışkan, H., Akova, H. U., Balkan, T., Platin, B. E., "Elektrohidrolik abkant pres tasarımı – II: kontrol sistemi", *Proceedings of the 15th National Automatic Control Conference*, Malatya, Turkey, pp. 1328-1333, 26-29 September 2013.

[19] Çalışkan, H., Akova, H. U., Balkan, T., Platin, B. E., "Elektro-hidrostatik tahrikli bir hareket benzetimcisinin alt sistemlerinin ortak simülasyonu", *Proceedings of 5th National Defense Applications Modelling and Simulation Conference*, Ankara, Turkey, pp. 465-474, 11-12 June 2013.

[20] Guerrier, P. K., Edge, K. A., "Evaluation of P-Q controllers for an injection moulding machine", *ASME International Mechanical Engineering Congress and Exposition*, Chicago, IL, USA, 5-10 November 2006.

[21] Sam, Y. M., Hudha, K., "Modelling and force tracking control of hydraulic actuator for an active suspension system", *1st IEEE Conference on Industrial Electronics and Applications (ICIEA 2006)*, Singapure, pp. 1-6, 24-26 May 2006.

[22] Kim, W., Won, S., "Modeling and control for an asymmetric hydraulic active suspension system", *JSME International Journal*, vol. 44, no. 2, pp. 397-403, 2001.

[23] Pierrot, F, Dombre, E., Degoulange, E., Urbain, L., Caron, P., Boudet, S., Gariepy, J., Megnien, J., "Hippocrate: a safe robot arm for medical applications with force feedback", *Medical Image Analysis*, vol. 3, issue. 3, pp. 285-300, September 1999.

[24] Eppinger, S. D., Seering, W. P., "Three dynamic problems in robot force control", *IEEE Transactions on Robotics and Automation*, vol. 8, no. 6, pp. 751-758, December 1992.

[25] Carignan, C. R., Cleary, K. R., "Closed-loop force control for haptic simulation of virtual environments", *The Electronic Journal of Haptics Research (Haptics-e)*, vol. 1, no. 2, 23 February 2000.

[26] Nachtigal, C. L., *Instrumentation and Control: Fundamentals and Applications*, Wiley Series in Mechanical Engineering Practice, New York, John Wiley and Sons, 1990.

[27] Sivaselvan, M. V., Reinhorn, A. M., Shao, X., Weinreber, S., "Dynamic force control with hydraulic actuators using added compliance and displacement compensation", *Earthquake Engineering and Structural Dynamics*, vol. 37, issue 15, pp. 1785-1800, December 2008.

[28] Ahn, K. K., Dinh, Q. T., "Self-tuning of quantitative feedback theory for force control of an electro-hydraulic test machine", *Control Engineering Practice*, vol. 17, issue 11, pp. 1291-1306, November 2009.

[29] Pratt, J., Krupp, B., Morse, C., "Series elastic actuators for high fidelity force control", *Industrial Robot: An International Journal*, vol. 29, no. 3, pp. 234-241, 2002.

[30] Robinson, D. W., "Design and analysis of series elasticity in closed-loop actuator force control", Ph.D. dissertation, Department of Mechanical Engineering, Massachusetts Institute of Technology, Cambridge, MA, USA, June 2000.

[31] Reinhorn, A. M., Sivaselvan, M. V., Weinreber, S., Shao, X., "A novel approach to dynamic force control", *Proceedings of the Third European Conference on Structural Control*, Vienna, Austria, 12-15 July 2004.

[32] Karpenko, M., Sepehri, N., "Electrohydraulic force control design of a hardware-in-the-loop load emulator using a nonlinear QFT technique", *Control Engineering Practice*, vol. 20, pp. 598-609, 2012.

[33] Plummer, A. R., "Robust electrohydraulic force control", *Proceedings of Institution of Mechanical Engineers, Part I: Journal of Systems and Control Engineering*, vol. 221, pp. 717-731, 2007.

[34] Diming, J., Shield, C., French, C., Balley, F., Clark, A., "Effective force testing: a method of seismic simulation for structural testing", *Journal of Structural Engineering*, American Society of Civil Engineers, vol. 125, No. 9, pp. 1028-1037, September 1999.

[35] Alleyne, A., Liu, R., "A simplified approach to force control for electro-hydraulic systems", *Control Engineering Practice*, vol. 8, pp. 1347-1356, 2000.

[36] Jacazio, G., Balossini, G., "Real-time loading actuator control for an advanced aerospace test rig", *Proceedings of the Institution of Mechanical Engineers, Part I: Systems and Control Engineering*, pp. 199-209, 2007.

[37] Garcia, A., Cusido, J., Rosero, J. A., Ortega, J. A., Romeral, L., "Reliable electro-mechanical actuators in aircraft", *IEEE A&E Systems Magazine*, vol. 23, issue 8, pp. 19-25, August 2008.

[38] Zongxia, J., Jurrxia, G., Qing, H, Shaoping, W., "The velocity synchronizing control on the electro-hydraulic load simulator", *Chinese Journal of Aeronautics*, vol. 17, no. 1, February 2004.

[39] Kashi, K., Söffker, D., Nissing, D., Kesselgruber, D., "Vehicle dynamics investigation using a hydraulic hardware-in-the-loop test-rig", *Proceedings of Conference Proceedings for 1st International Conference on Computational Methods in Fluid Power Technology*, Fluid Power Net Publications, Melbourne, Australia, 2003.

[40] Merritt, H. E., *Hydraulic Control Systems*, John Wiley & Sons, Inc., 1967.

[41] Jelali, M., Kroll, A., *Hydraulic Servo-systems: Modelling, Identification and Control*, Springer, 2003.

[42] *Direct Operated Proportional DC Valve Series D1FP Catalogue HY11-3500/UK*, pp. 3.81-3.86, Parker Hannifin Corporation, retrieved from http://www.parker.com/literature/Hydraulic%20Controls%20Europe/HY11-3500UK/HY11-3500UK_10.2011_PDFoverall.pdf, last viewed on 04.03.2014.

[43] *Pressure Relief Cartridge Valve*, Bucher Hydraulics, retrieved from http://www.bucherhydraulics.com/bausteine.net/f/7654/DVPA-1_400-P-280101-E-01.pdf?fd=3, last viewed on 18.03.2014.

[44] *Hydropneumatic accumulators – Pulsation dampeners*, SAIP, retrieved from http://www.saipusa.com/uploads/Catalogo_Saip_2008_NUOVO.pdf, last viewed on 19.03.2014.

[45] *Reservoirs, Hydraulics and Pneumatics*, retrieved from http://hydraulicspneumatics.com/200/TechZone/ReservoirsAcces/Article/False/6448/TechZone-ReservoirsAcces, last viewed on 18.03.2014.

[46] Watton, J., *Fundamentals of Fluid Power Control*, Cambridge University Press, 2009.

[47] *Burster Tension and Compression Load Cell Model 8524*, Burster, retrieved from http://www.burster.com/fileadmin/Documents/Products/Data_Sheets/Section_8/8524_EN.pdf, last viewed on 10.03.2014.

[48] *Trafag 8472 Economic Industrial Pressure Transmitter*, Trafag Sensors and Controls, retrieved from http://www.trafag.com/pdfs/pdfdatasheets/H72324k_Economic_Industrial_Pressure_Transmitter_ECT_8472.pdf, last viewed on 10.03.2014.

[49] *Novotechnik Transducer up to 4500 mm touchless absolute*, retrieved from http://www.alfasanayi.com/urun/PDF/TMI_GB.pdf, last viewed on 10.03.2014.

[50] Backe, W., *Servohydraulik. Lecture Notes*, Technical University of Aachen, Germany, 1992.

[51] Rahmfeld, R., "Development and control of energy saving hydraulic servo drives for mobile systems", PhD. dissertation, Institute for Aircraft Systems Engineering, Technical University of Hamburg, Germany, December 2002.

[52] Ljung, L., "Perspectives on the process of identification", *Proceedings of the 12th World Congress IFAC*, Sydney, Australia, vol. 7, pp. 511-516, 1993.

[53] Wang, X., Dongzhou, F., "A study on dynamics of electric load simulator using spring beam and feedforward control technique", *Proceedings of IEEE Chinese Control and Decision Conference*, Guilin, China, pp. 301-306, 17-19 June 2009.

[54] Shang, Y., Wu, S., Jiao, Z., Wang, X., "Study on ultimate performance of light-duty electro-hydraulic torque-load simulator", *Proceedings of IEEE Conference on Robotics, Automation and Mechatronics*, Chengdu, China, pp. 387-392, 21-24 September 2008.

[55] Aström, K. J., Murray, R. M., *Feedback Systems An Introduction for Scientists and Engineers*, Princeton University Press, Princeton, NJ, USA, 2009.

[56] Aström, K. J., *Introduction to Control, Department of Automatic Control*, Lund Institute of Technology, Lund University, Sweden, 2004.

[57] Mare, J. C., "Dynamic loading systems for ground testing of high speed aerospace actuators", *Aircraft Engineering and Aerospace Technology: An International Journal*, vol. 78, no. 4, pp 275-282, 2006.

[58] Ogata, K., *Modern Control Engineering*, Fifth Edition, Prentice Hall, 2010.

[59] Kim, H. W., Sul, S., K., "A new motor speed estimator using Kalman filter in low-speed range", *IEEE Transactions on Industrial Electronics*, vol. 43, no. 4, pp. 498-504, August 1996.

[60] Bideci, S., "Control system design for a haptic device", M.Sc. thesis, Mechanical Engineering Department, METU, Ankara, Turkey, 2007.

[61] Jeon, S., "State estimation based on kinematic models considering characteristics of sensors", *Proceedings of the American Control Conference (ACC)*, Baltimore, MD, USA, pp. 640-645, June, 2010.

[62] Welch, G., Bishop, G., An Introduction to the Kalman Filter, Department of Computer Science, University of North Carolina at Chapel Hill, retrieved from http://www.cs.unc.edu/~welch/media/pdf/kalman_intro.pdf, last viewed on 15.04.2014.

[63] Shalom, Y. B., Kirubarajan, T., *Estimation with Applications To Tracking and Navigation*, John Wiley & Sons, Inc., 2001.

[64] Belanger, P. R., "Estimation of angular velocity and acceleration from shaft encoder measurements", *Proceedings of the 1992 IEEE International Conference on Robotics and Automation*, Nice, France, Vol. 1, pp. 585-592, 1992.

[65] Wang, J. J., Ding, W., Wang, H., "Improving adaptive Kalman filter in GPS/SDINS integration with neural network", *Proceedings of the 20th International Technical Meeting of the Satellite Division of the Institute of Navigation (ION GNSS 2007)*, Fort Worth, TX, USA, pp. 571-578, September 2007.

[66] Franklin, F. G., Powell, J. D., Workman, M., *Digital Control of Dynamic Systems*, Third Edition, Ellis-Kagle Press, 1998.

[67] How to Calibrate a Pressure Gauge with a Dead Weight Tester, retrieved from http://www.instrumentationtoolbox.com/2013/08/how-to-calibrate-pressure-gauge-with.html#axzz2sx5FeQiD, last viewed on 10.02.2014.

[68] *Burster Amplifier Module Model 9243*, Burster, retrieved from http://burster.de/fileadmin/Documents/Products/Manuals/Section_9/BA_9243_EN.pdf, last viewed on 10.03.2014.

APPENDIX A

ELECTRICAL CONNECTIONS

A.1 Real-Time Target Machine Connections

- **I/O105 Analog Input Module**

Pin on Terminal Board	Single Ended Mode	Differential Mode	
1	Input01	Input01 (+)	
2	Input02	Input01 (-)	
3	Input03	Input02 (+)	
4	Input04	Input02 (-)	
5	Input05	Input03 (+)	
6	Input06	Input03 (-)	
7	Input07	Input04 (+)	
8	Input08	Input04 (-)	
9	Input09	Input05 (+)	
10	Input10	Input05 (-)	
11	Input11	Input06 (+)	
12	Input12	Input06 (-)	
13	Input13	Input07 (+)	
14	Input14	Input07 (-)	
15	Input15	Input08 (+)	Pressure transducer, Piston-side pressure, p_A
16	Input16	Input08 (-)	
17	GROUND	GROUND	
18	GROUND	GROUND	
19	Input17	Input09 (+)	Pressure transducer, Rod-side pressure, p_B
20	Input18	Input09 (-)	
21	Input19	Input10 (+)	
22	Input20	Input10 (-)	
23	Input21	Input11 (+)	Force transducer, F
24	Input22	Input11 (-)	
25	Input23	Input12 (+)	Proportional control valve spool position, LVDT
26	Input24	Input12 (-)	
27	Input25	Input13 (+)	
28	Input26	Input13 (-)	
29	Input27	Input14 (+)	Position transducer, x
30	Input28	Input14 (-)	
31	Input29	Input15 (+)	
32	Input30	Input15 (-)	
33	Input31	Input16 (+)	
34	Input32	Input16 (-)	

Figure A.1-1 Analog input connections

- **I/O111 Analog Output Module**

Pin on Terminal Board	D/A Channel	Q-DAC	Q-DAC Internal D/A Channel	
1	Output01	1	A	
2	Output02		B	
3	Output03		C	
4	Output04		D	
5	Output05	2	A	
6	Output06		B	
7	Output07		C	
8	Output08		D	
9	Output09	3	A	
10	Output10		B	Valve command signal, u
11	Output11		C	Valve spool actuator enable
12	Output12		D	
13	Output13	4	A	
14	Output14		B	
15	Output15		C	
16	Output16		D	
17				
18				
19				
20				
21				
22				
23				
24				
25				
26				
27				
28				
29				
30				
31				
32				
33				
34				

Figure A.1-2 Analog output connections

- **I/O 401 TTL/SSI Encoder Module**

Pin on Terminal Board	SSI Signal (TTL and RS422)	Counter Signal (TTL and RS422)	Pin on Terminal Board	SSI Signal (for RS422 only)	Counter Signal (for RS422 only)	
1		QAD_A01 (+)	35		QAD_A01 (-)	Channel A , signals A and /A
2	CLK IN01 (+)	QAD_B01 (+)	36	CLK IN01 (-)	QAD_B01 (-)	Channel B , signals B and /B
3	DATA01 (+)	QAD_I01 (+)	37	DATA01 (-)	QAD_I01 (-)	Channel Z , signals Z and /Z
4	CLK OUT01 (+)		38	CLK OUT01 (-)		
5	GROUND		39	GROUND		
6		QAD_A02 (+)	40		QAD_A02 (-)	
7	CLK IN02 (+)	QAD_B02 (+)	41	CLK IN02 (-)	QAD_B02 (-)	
8	DATA02 (+)	QAD_I02 (+)	42	DATA02 (-)	QAD_I02 (-)	
9	CLK OUT02 (+)		43	CLK OUT02 (-)		
10		QAD_A03 (+)	44		QAD_A03 (-)	
11	CLK IN03 (+)	QAD_B03 (+)	45	CLK IN03 (-)	QAD_B03 (-)	
12	DATA03 (+)	QAD_I03 (+)	46	DATA03 (-)	QAD_I03 (-)	
13	CLK OUT03 (+)		47	CLK OUT03 (-)		
14	GROUND		48	GROUND		
15		QAD_A04 (+)	49		QAD_A04 (-)	
16	CLK IN04 (+)	QAD_B04 (+)	50	CLK IN04 (-)	QAD_B04 (-)	
17	DATA04 (+)	QAD_I04 (+)	51	DATA04 (-)	QAD_I04 (-)	
18	CLK OUT04 (+)		52	CLK OUT04 (-)		
19		QAD_A05 (+)	53		QAD_A05 (-)	
20	CLK IN05 (+)	QAD_B05 (+)	54	CLK IN05 (-)	QAD_B05 (-)	
21	DATA05 (+)	QAD_I05 (+)	55	DATA05 (-)	QAD_I05 (-)	
22	CLK OUT05 (+)		56	CLK OUT05 (-)		
23	GROUND		57	GROUND		
24		QAD_A06 (+)	58		QAD_A06 (-)	
25	CLK IN06 (+)	QAD_B06 (+)	59	CLK IN06 (-)	QAD_B06 (-)	
26	DATA06 (+)	QAD_I06 (+)	60	DATA06 (-)	QAD_I06 (-)	
27	CLK OUT06 (+)		61	CLK OUT06 (-)		
28			62			
29	24V Digital Input 01		63	24V Digital Input 01 Ground		
30	24V Digital Input 02		64	24V Digital Input 02 Ground		
31	24V Digital Input 03		65	24V Digital Input 03 Ground		
32	24V Digital Input 04		66	24V Digital Input 04 Ground		
33	24V Digital Input 05		67	24V Digital Input 05 Ground		
34	24V Digital Input 06		68	24V Digital Input 06 Ground		

Figure A.1-3 Incremental encoder connections

A.2 Proportional Directional Control Valve Connections

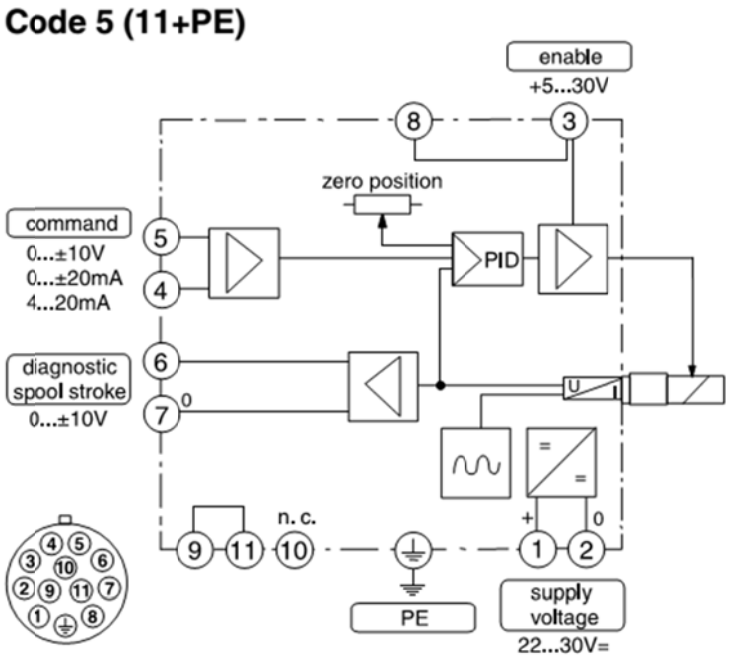

Figure A.2-1 Proportional valve connections

The command signal for the valve spool position from IO111 module of real-time target machine is connected to the pins 4 and 5 of the electronic driver of the valve. The actual position of the valve spool is available through pins 6 and 7.

For the continuous operation of the proportional control valve a permanent supply voltage of $24\ V\ DC$ is provided at pin 3 with respect to PE.

APPENDIX B

CALIBRATION AND SETTINGS OF TRANSDUCERS

B.1 Calibration of Pressure Transducers

The pressure transducers are calibrated by using a dead weight pressure tester which is seen in Figure B.1-1. It consists of a weight carrier, a screw pump, an oil reservoir, and a test port.

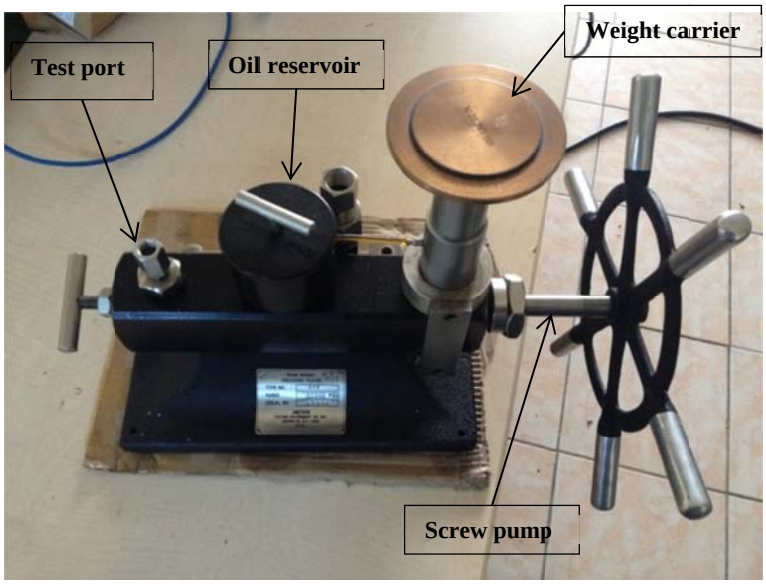

Figure B.1-1 Dead weight pressure tester

The calibration procedure is summarized as follows [67]:

- The transducer to be calibrated is connected to the test port.
- A calibration load with a known weight is placed onto the weight carrier.
- The oil pressure is increased by using the screw pump and the weight carrier with the calibration load is raised by the oil pressure.
- Having the pressure oscillations damped out, the voltage output of the transducer is read.
- The previous steps are repeated for different calibration loads.

The calibration curves of the pressure transducers are given in Figures B.1-2 and B.1-3 for the rod and piston sides.

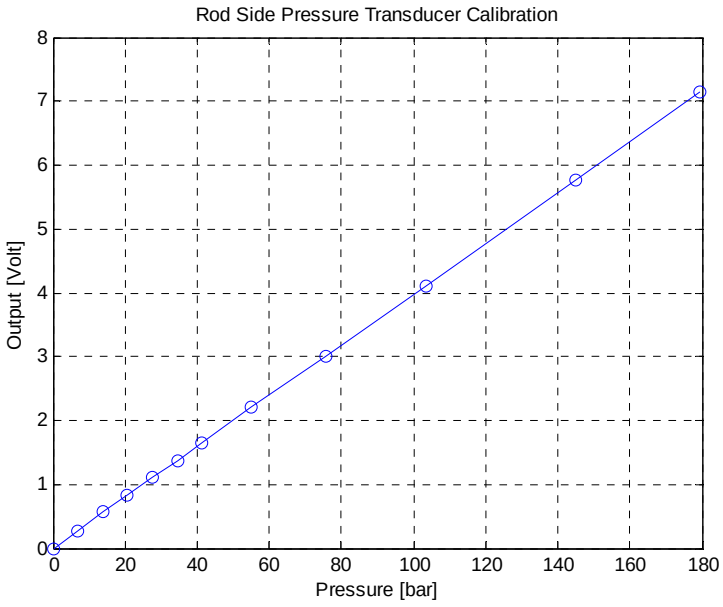

Figure B.1-2 Rod side pressure transducer calibration

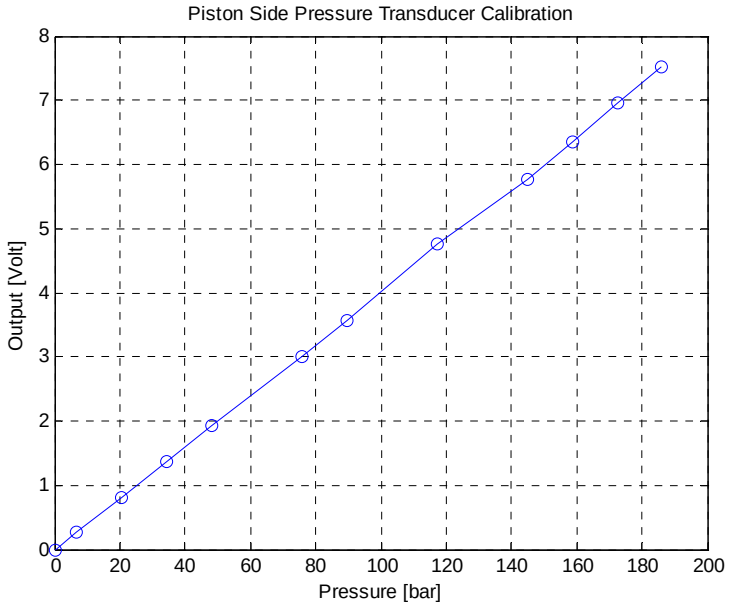

Figure B.1-3 Piston side pressure transducer calibration

B.2 Gain Setting and Calibration of Power Amplifier

A signal amplifier, Burster Amplifier Module 9243 [68], is utilized in this study in order to amplify the output of the force transducer, which is a signal in the order of a few millivolts. In Figure B.2-1, the front view of the amplifier module together with the terminal assignment table is given. In the figure, the fine gain adjustment & zero point potentiometers can also be seen.

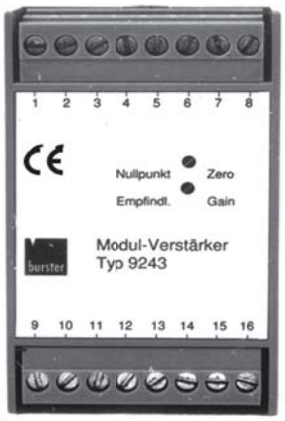

Terminal	Function		Description
1	Input:	+ / ~	Supply voltage
2	Input:	- /~	Supply voltage
3	Output:	-	Ground for the current output
4	Output:	+	Current output
5	Output:	-	Ground for the voltage output
6	Output:	+	*10 V output
7	Output:	+	±5 V monitor output
8	Output:	+	Calibration voltage 5 mV
9	Sensor:	-	Sensor excitation, shield
10	Sensor:	-	Sense
11	Sensor:	+	Sensor excitation
12	Sensor:	+	Sense
13	Sensor:	-	Signal input
14	Sensor:	+	Signal input
15	Input:		Calibration shunt
16	Input:		Calibration shunt

Figure B.2-1 Burster Amplifier Module 9243 - Front view & Terminal assignment table [68]

The desired gain of the amplifier module V_{total} is determined as follows:

$$V_{total} = \frac{U_r}{U_a} \tag{B.1}$$

where U_a is the maximum voltage output of the force transducer at maximum deflection, and U_r is the required voltage output of the amplifier at U_a.

The maximum output of the force transducer is determined as $7.5\ mV$ in Chapter 2, and the required output of the amplifier is $U_r = 10\ V$ since the analog input range of the DAQ system is $10\ V$. Therefore, the gain of the amplifier, from Equation (B.1), is to be

$$V_{total} = \frac{U_r}{U_a} = \frac{10\ V}{7.5\ mV} \cong 1333 \tag{B.2}$$

The required gain of the amplifier module is adjusted coarsely from the DIP switches available on the left side of the amplifier module (Figure B.2-2) and finely from the fine adjustment potentiometer on the front of the amplifier module as

$$V_{total} = V_{stage1} \cdot V_{stage2} \cdot V_{stage3} \cdot (0.85 \dots 1.11) \quad \text{(B.3)}$$

where the first three gains, V_{stage1}, V_{stage2}, V_{stage3}, are for the coarse adjustment stages, and the last term represents the fine adjustment stage.

Hence, the coarse adjustment gains are set as $10, 16.75,$ and 8, respectively. Therefore, the product of these three gains yields to a gain of 1340. These gains are set by properly adjusting the DIP (dual in-line package)switches as seen in Figure B.2-2. Finally, the desired gain of 1333 is obtained by the fine adjustment potentiometer.

The calibration of the amplifier module is performed by using the highly precise $5.0\ mV$ voltage source available on the module. The corresponding terminal of the precision voltage source is terminal 8 (Figure B.2-1). Hence, the following steps are followed for the calibration of the amplifier module:

- Disconnect the transducer,
- Connect the input terminals (13, 14) to the ground terminal (9),
- Adjust "0 V" at the output of the module via the zero point potentiometer,
- Connect terminal 14 to terminal of the precision voltage source (8),
- Adjust the calculated voltage output with the set gain V_{total},
- Connect the transducer and adjust the zero point through the potentiometer.

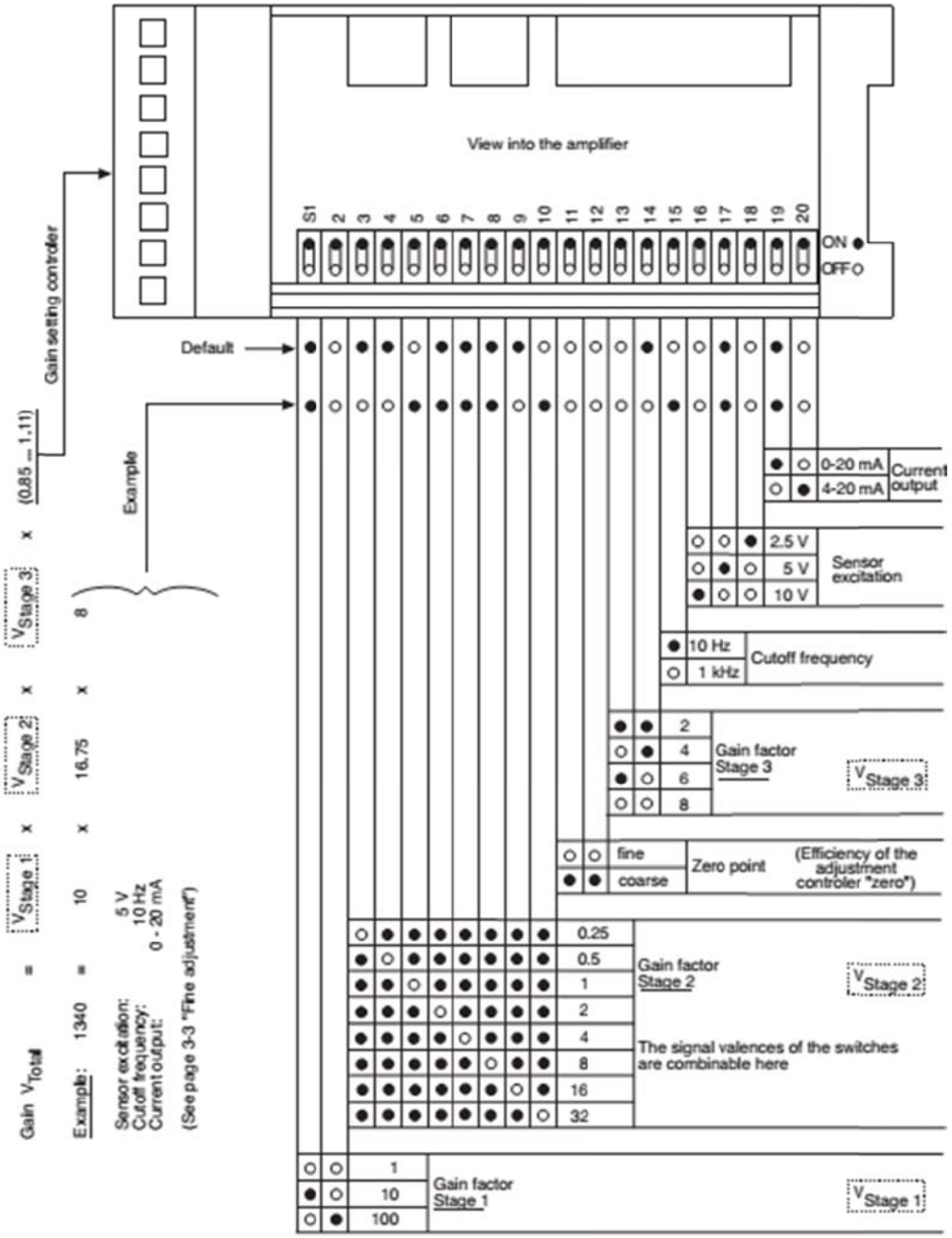

Figure B.2-2 Gain adjustment of the amplification module by DIP switches [68]

APPENDIX C

TECHNICAL DRAWINGS WITH NOMINAL DIMENSIONS

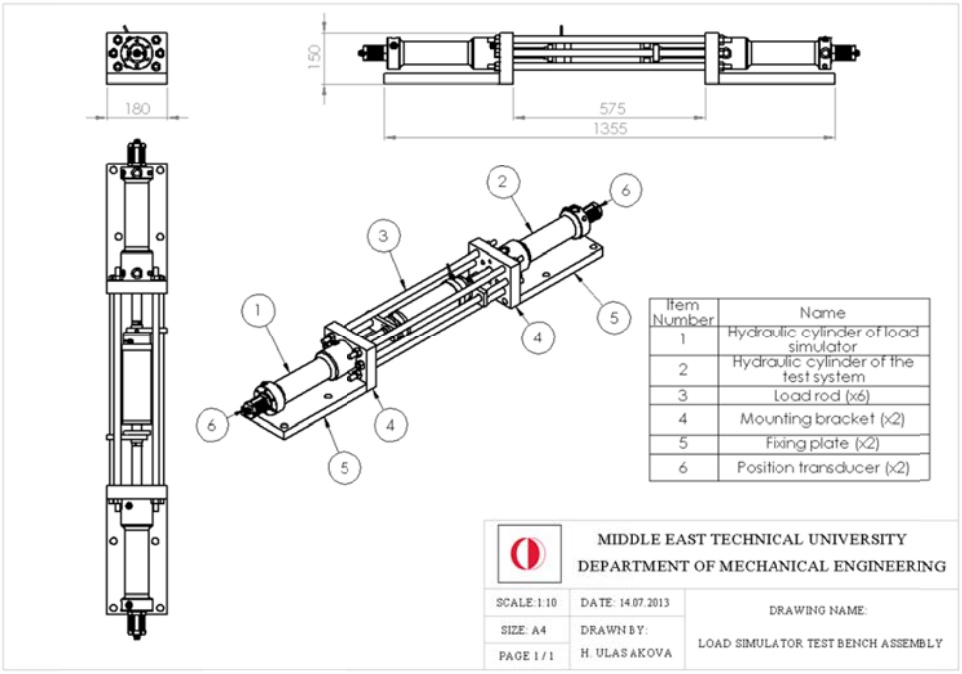

Figure C-1 Load simulator test bench assembly

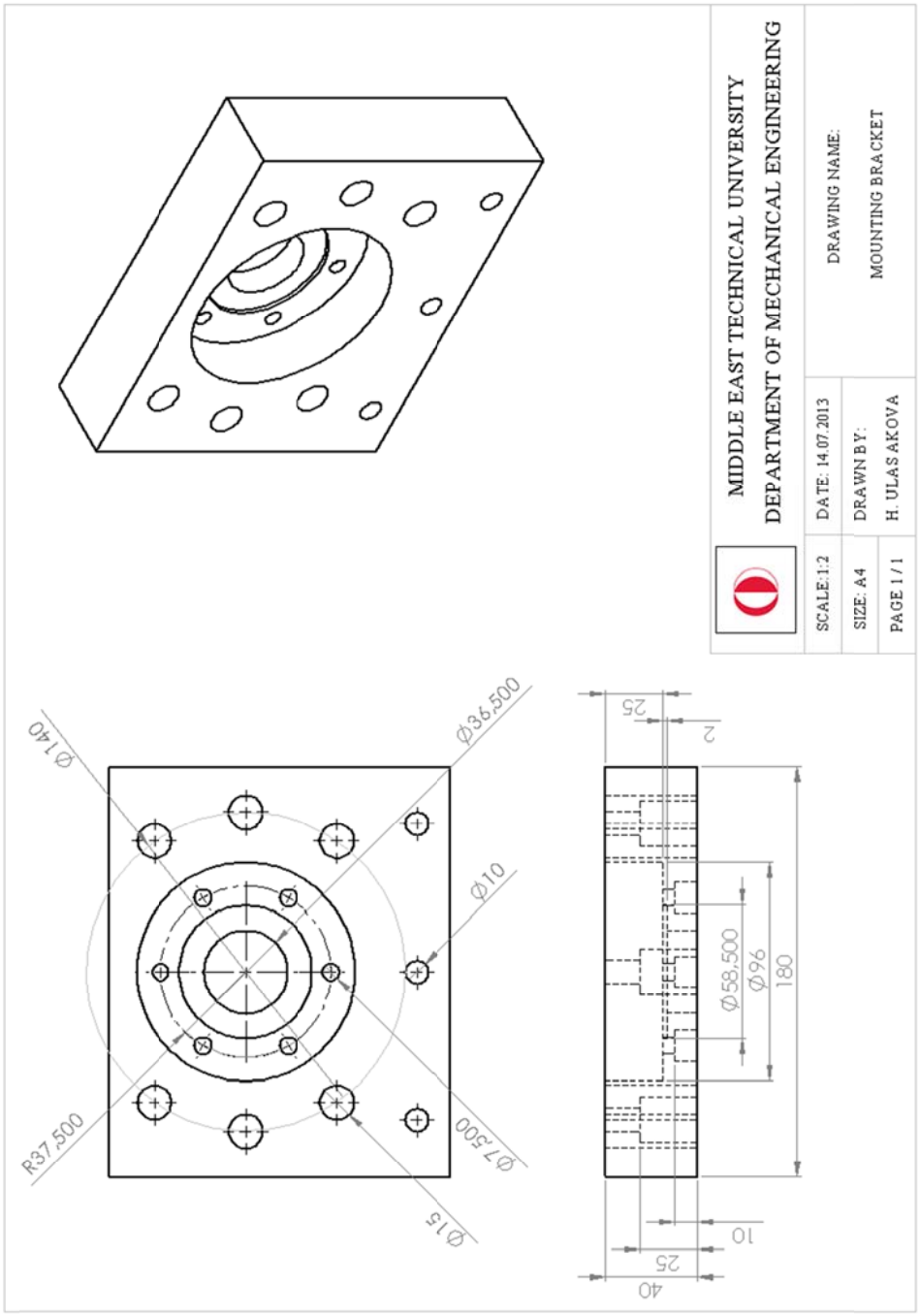

Figure C-2 Mounting bracket

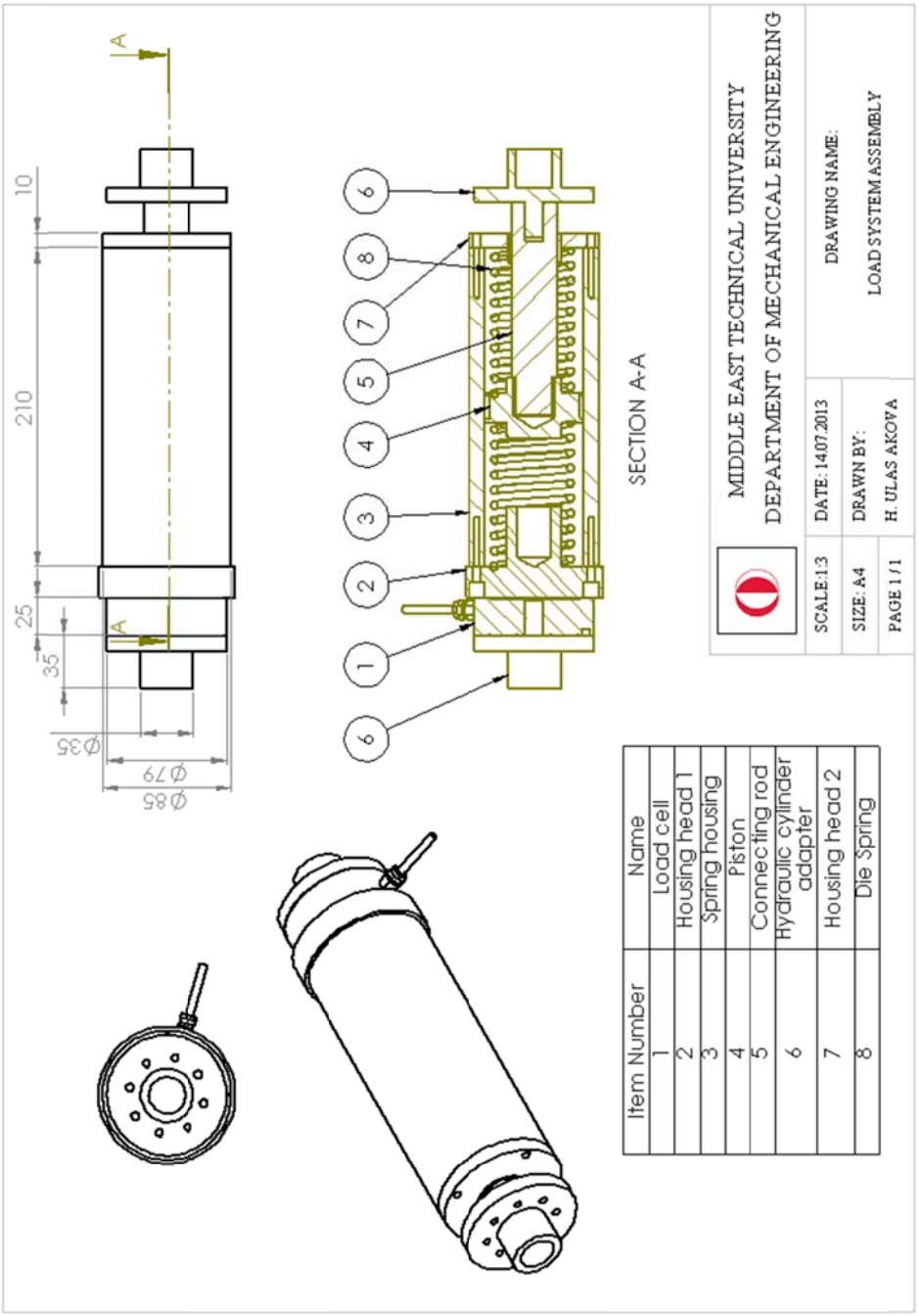

Figure C-3 Load spring system assembly

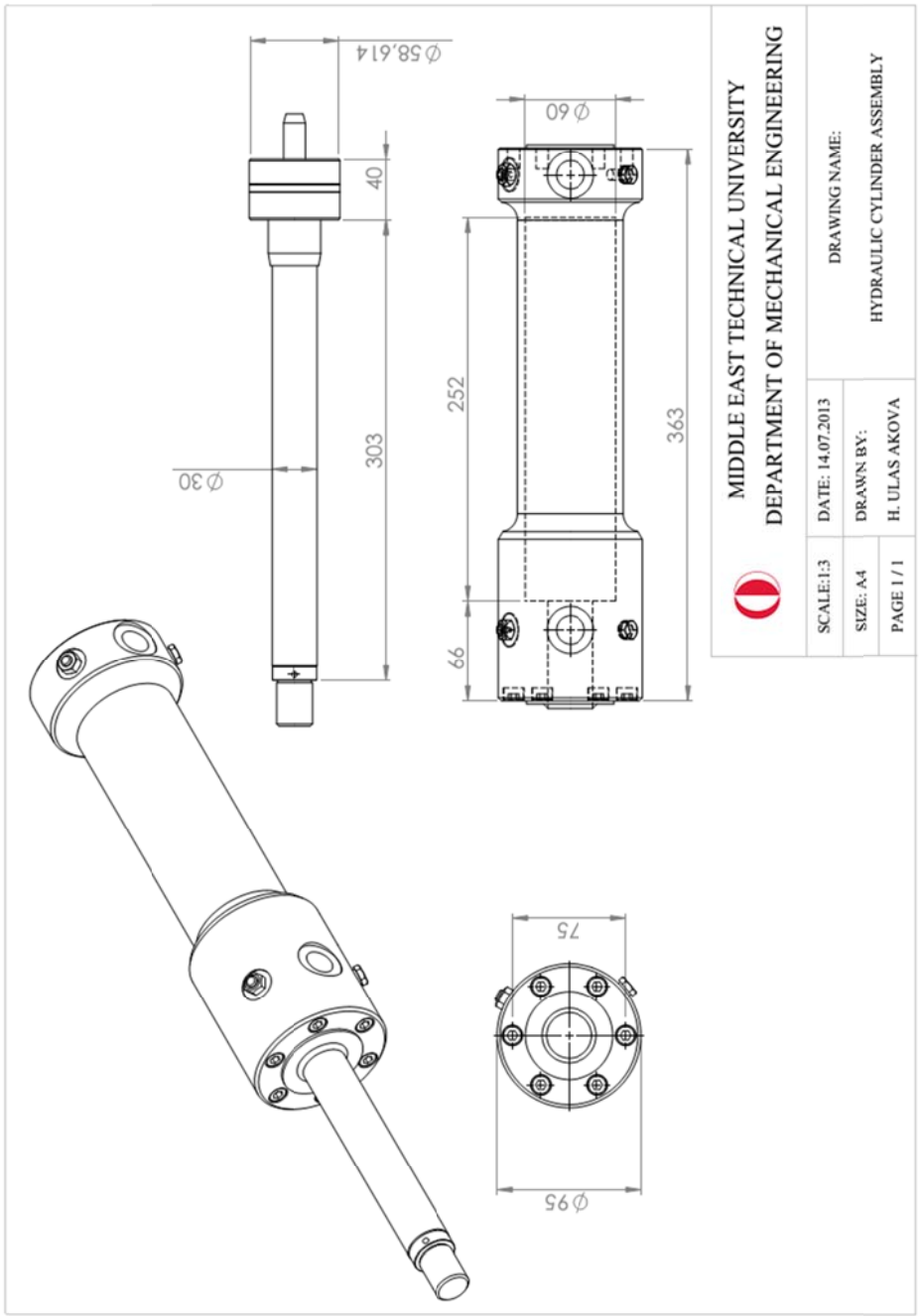

Figure C-4 Hydraulic cylinder assembly

APPENDIX D

SPRING STIFFNESS

The stiffness of the die springs used in this study is highlighted in the catalog of the manufacturer as seen in Figure D-1.

YELLOW DIE SPRING –EXTRA HEAVY DUTY

D_H Outer Diameter	D_d Inner Diameter	L_0 Free Length	Stiffness
mm	mm	mm	N/mm
		32	27.9
		38	23.7
		44	19.2
		51	16.5
		64	13.2
		76	10.9
mm	mm	mm	N/mm
63	38	76	952
		89	819
		102	700
		115	620
		127	565
		152	458
		178	384
		203	337

Figure D-1 Spring stiffness

APPENDIX E

M - FILES

- **Simulation Parameters and Plant Transfer Functions**

```
% Load Simulator - Model Parameters
% 04.05.2014
% ---------------------------------------- %
clear all;
clc;
% ---------------------------------------- %
% Sampling time
Ts = 0.001;      % [Second]
% Supply pressure
p_supply = 12;   % [MPa]
% Fluid propoerties
B = 1.3e9/1e6;   % Bulk Modulus of the Fluid - Nominal
Value [Pa]2[MPa]
% Valve parameters
Kv = (25/60*1e6)/10/sqrt(3.5); % [mm^3/s]/V/[MPa]^0.5
Tv = 1 / 2 / pi / 80;   % [Rad/s]
u_max = 10;  % [V]
% Actuator Parameters
% Hanchen
A_A = pi/4 * (0.060^2) * 1e6; % Piston Area A[m^2]2[mm^2]
A_B = pi/4 * (0.060^2-0.030^2) * 1e6; % Piston Area B
alpha = A_B / A_A;               % Area Ratio [unitless]
x_piston = 0.2*1e3;              % Piston Stroke [m]2[mm]
V_dead_A = A_A*15;               % Dead volume A
[m^3]2[mm^3]
V_dead_B = A_B*15;               % Dead volume B
[m^3]2[mm^3]
% Initial volume in the chambers of the Actuator
% Assuming that the piston is at the midstroke
```

```
% Initial Volume A [mm^3] – at mid-stroke
V_A = V_dead_A + x_piston * 0.5 * A_A;
V_initial_A = V_A;
% Initial Volume B [mm^3]
V_B = V_dead_B + x_piston * 0.5 * A_B;
V_initial_B = V_B;
% Load Model
% M = 3*1e-3;  % Mass [metric ton] – for open-loop tests
M = (3+5)*1e-3;  % Mass [metric ton] with adapter parts
k = 565 * 2;   % Spring rate [N/mm]
b = 6500/1e3;  % Damping coefficient [N/(m/s)]2[N/(mm/s)]

%% ---------------------------------------- %
% Linearized Models
% ---------------------------------------- %
% Effective flow area
A = A_A * (1 + alpha^2 * (V_A /V_B));
% Capacitance
C = V_A / B;
% Valve Dynamics
G_valve = tf(1,[Tv 1]);
% ---------------------------------------- %
% For xv >= 0, Extention of the hydraulic actuator
% Operating point around which the linearization
% will be performed:
p_load_0 = 0;
x_valve_0 = 0;
% Steady State Pressures
p_A_0_ext = (p_load_0 + alpha^3 * p_supply) / (1 +
alpha^3);
p_B_0_ext = (-alpha^2 * (p_load_0 - p_supply)) / (1 +
alpha^3);
% Valve Coefficients [mm^2/s]
KqA_ext = Kv * sqrt(p_supply - p_A_0_ext);
KqB_ext = Kv * sqrt(p_B_0_ext);
KcA_ext = Kv * x_valve_0 / 2 / sqrt(p_supply -
p_A_0_ext);
KcB_ext = -Kv * x_valve_0 / 2 / sqrt(p_B_0_ext);
% Equivalent Parameters
KQ_ext = KqA_ext + alpha * (V_A / V_B) * KqB_ext;
KC_ext = (KcA_ext - alpha^3 * (V_A / V_B) * KcB_ext) / (1
+ alpha^3);
% Transfer Functions for Extention
% G_FU(s) for extension
```

```
G_ext_force = tf(KQ_ext * k * A_A,[C*M (C*b+KC_ext*M)
(KC_ext*b+A*A_A+k*C) (k*KC_ext)]) * G_valve;
% G_FXd(s) for extension
G_ext_force_dist = minreal(tf(k*[C*M (C*b+KC_ext*M)
(KC_ext*b+A*A_A) 0],[C*M (C*b+KC_ext*M)
(KC_ext*b+A*A_A+k*C) (k*KC_ext)]));
% ---------------------------------------- %
% For xv < 0, Retraction of the hydraulic actuator
% Steady State Pressures
p_A_0_ret = (p_load_0 + alpha * p_supply) / (1 +
alpha^3);
p_B_0_ret = (p_supply - alpha^2 * p_load_0) / (1 +
alpha^3);
% Valve Coefficients
KqA_ret = Kv * sqrt(p_A_0_ret);
KqB_ret = Kv * sqrt(p_supply - p_B_0_ret);
KcA_ret = -Kv * x_valve_0 / 2 / sqrt(p_A_0_ret);
KcB_ret = Kv* x_valve_0 / 2 / sqrt(p_supply - p_B_0_ret);
% Equivalent Parameters
KQ_ret = KqA_ret + alpha * (V_A / V_B) * KqB_ret;
KC_ret = (KcA_ret - alpha^3 * (V_A / V_B) * KcB_ret) / (1
+ alpha^3);
% Transfer Functions for Retraction
G_ret_force = tf(KQ_ret * k * A_A,[C*M (C*b+KC_ret*M)
(KC_ret*b+A_A*A+k*C) (k*KC_ret)]) * G_valve;
G_ret_force_dist = tf(k*[C*M (C*b+KC_ret*M)
(KC_ret*b+A*A_A) 0],[C*M (C*b+KC_ret*M)
(KC_ret*b+A*A_A+k*C) (k*KC_ret)]);
```

- **Fourier Analysis of the Experimental Data**

```
function BodePlot(x_in,y_out,t_start,t_end,PloT,Ts)
% Delete the undesired data range
x_in([1:t_start/Ts-1,t_end/Ts+1:end]) = [];
y_out([1:t_start/Ts-1,t_end/Ts+1:end]) = [];
% Time vector [second]
t = t_start:Ts:t_end;
Fs = 1/Ts;
% Number of points
npts = length(t);
% Remove the bias
x = detrend(x_in);
y = detrend(y_out);
```

```
% Auxiliary Plots
if PloT>0
% Plot the signal
figure
plot(t,x,t,y);
xlabel('Time (s)');
ylabel('Amplitude');
legend('Signal x(t)');
end
% Fast Fourier Transform(FFT) of the Data
X=fft(x);
Y=fft(y);
% Determine the numberof unique points
NumUniquePts = ceil((npts+1)/2);
f = (0:NumUniquePts-1)*Fs/npts;
if PloT>0
figure;   subplot(211);
plot(f,abs(X(1:NumUniquePts)));
title('X(f) : Magnitude response');
ylabel('|X(f)|'); subplot(212);
plot(f,abs(Y(1:NumUniquePts)));
title('Y(f) : Magnitude response')
xlabel('Frequency (Hz)'); ylabel('|Y(f)|')
figure; subplot(211);
plot(f,angle(X(1:NumUniquePts)));
title('Phase response');
ylabel('Phase (rad)'); subplot(212);
plot(f,angle(Y(1:NumUniquePts)));
title('Phase response');
xlabel('Frequency (Hz)');
ylabel('Phase (rad)');
end
% Magnitude [dB]
MAG = 20*log10(abs(X)./abs(Y));
% Phase [degree]
PHA = (angle(X)-angle(Y))*180/pi;   % degree
% Format phase
for i = 1 : 1 : (size(PHA) - 1)
    if PHA(i+1)-PHA(i) > 200
        PHA(i+1) = PHA(i+1)-360;
    elseif PHA(i+1)-PHA(i) <-200
        PHA(i+1) = PHA(i+1) + 360;
    end
end
% Bode Plots
```

```
figure('name','Bode Magnitude')
semilogx(f,MAG(1:NumUniquePts));
grid on;
xlabel('Frequency (Hz)');
figure('name','Bode Phase');
semilogx(f,PHA(1:NumUniquePts));
xlabel('Frequency (Hz)');
grid on;
```